JRC Scientific and Technical Reports

Quality assessment of hydro-geomorphological features derived from Digital Terrain Models

Laura Poggio and Pierre Soille

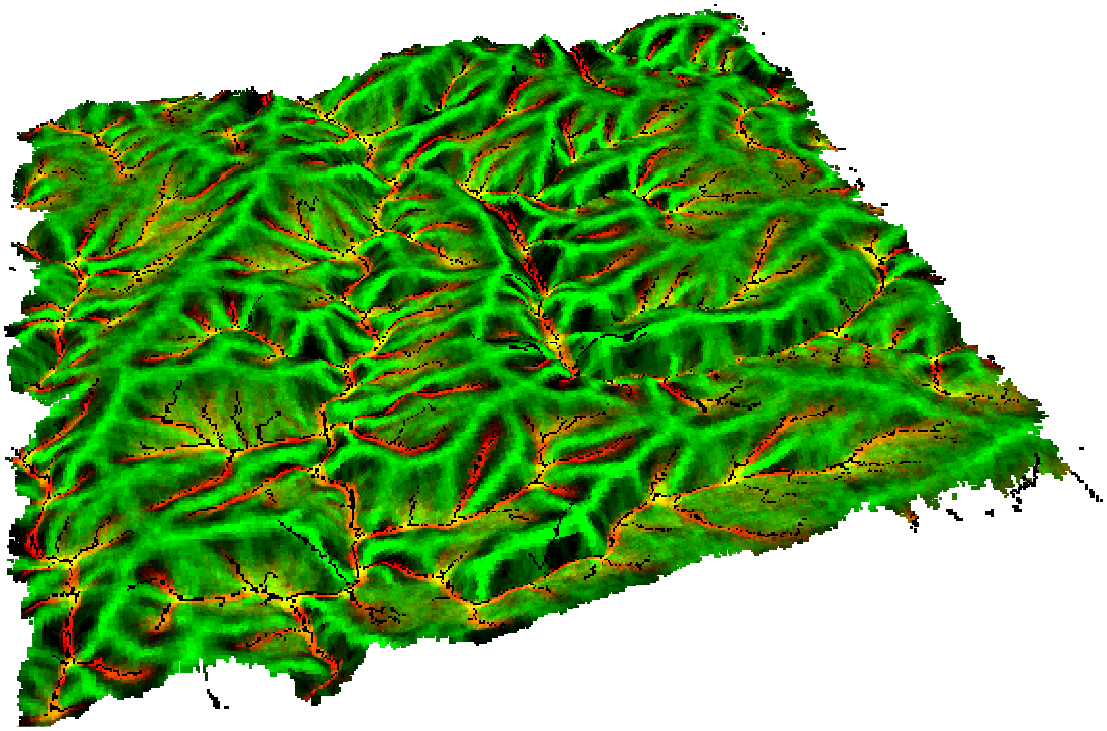

EUR 23489 EN - 2008

JRC
EUROPEAN COMMISSION

ies
Institute for Environment and Sustainability

The mission of the Institute for Environment and Sustainability is to provide scientific-technical support to the European Union's Policies for the protection and sustainable development of the European and global environment.

European Commission
Joint Research Centre
Institute for Environment and Sustainability

Contact information
Address: Pierre Soille – IES – SDI Unit, TP 262 – Ispra (VA) - Italy
E-mail: pierre.soille@jrc.it
Tel.: + 39 – 0332785068
Fax: + 39 - 0332786325

http://ies.jrc.ec.europa.eu/
http://www.jrc.ec.europa.eu/

JRC JRC47243

EUR 23489 EN
ISSN 1018-5593

Luxembourg: Office for Official Publications of the European Communities

Printed in Italy

JRC
EUROPEAN COMMISSION

Institute for Environment and Sustainability

Quality assessment of hydro-geomorphological features derived from Digital Terrain Models

Laura Poggio and Pierre Soille
COSIN Action
IES-Spatial Data Infrastructures Unit

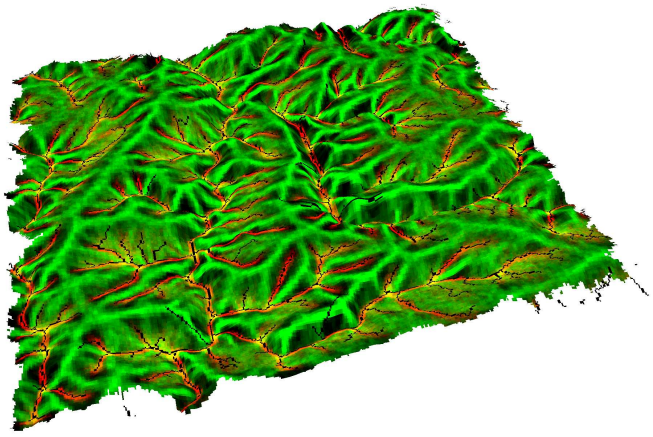

December 19, 2008

Abstract

Digital terrain models (DTM) provide a model for representing the continuous earth elevation surface that can contain errors introduced by the main phases of generation and modelling. Uncertainty of the model is rarely considered by users. Assessment of uncertainty require information on the nature, amount and spatial structure of the errors. DTMs of different original resolution were compared in order to assess the quality of derived hydrological and morphological features. SRTM dataset with resolution of 100m, DEM dataset mosaic from various sources with a resolution of 60m and ASTER derived dataset with a resolution of 30m were used. The error propagation was modelled with a stochastic approach. The probabilistic distribution of extracted hydrological features was drawn considering the spatial structure of errors in the datasets. The features considered were stream network and watershed divides net. The distribution of the Strahler order of the features was studied. An analysis of the overall probability of features extracted from variously prepared datasets was carried in order to get information on where is the most probable stream network or watershed divides net.

Contents

List of Figures

List of Tables

1 Introduction

Digital terrain models are the digital representation of ground surface topography. In the '50s a digital terrain model was defined as *a statistical representation of the continuous surface of a ground by a large number of selected points with known xyz coordinates in an arbitrary coordinate projection* (Miller and Laflamme, 1958). Since then other terms were introduced, such as *Digital elevation model* or *Digital Surface Model*. The terms have often a meaning depending on the context. Some definitions have been established in the years:

Digital terrain model (DTM): it is often used as synonym of bare-earth Digital Elevation Model (Maune, 2001). Sometimes it is used as an umbrella concept covering models of elevations and other geographical elements and natural features, such as rivers and other break lines. It may also include derived data about the terrain, such as slope, aspect, curvature, visibility, etc.;

Digital elevation model (DEM): it is a generic term covering digital topographic (and bathymetric) data in all its various forms as well as the method(s) for interpreting implicitly the elevations between observations. Normally implies elevations of bare earth without vegetation and buildings, but may include other man-made features, such as road/river embankments. Elevations of hydrological features (e.g. lakes and rivers) normally imply a free water surface (Maune, 2001). It is often considered the most fundamental component of DTM;

Digital Surface Model (DSM): it is a model depicting elevations of the top of reflective surfaces, such as buildings and vegetation (Maune, 2001).

1.1 Digital Terrain Models and uncertainty

DEMs represent the continuous earths elevation surface. This form of spatial data provides a model of reality that contains deviations from the truth, or errors. The nature and extent of these errors are often unknown and not readily available to users of spatial data. Uncertainty in the DEM representation of terrain through elevation and derived topographic parameters is rarely accounted for by DEM users. Systematic errors result from the procedures used in the DEM generation process and follow fixed patterns that can cause bias or artefacts in the final DEM product. When the cause is known, systematic bias can be eliminated or reduced. Blunders are vertical errors associated with the data collection process and are generally identified and removed prior to release of the data. Random errors remain in the data after known blunders and systematic errors are removed.

Sources of DEM errors have been described in detail (Burrough and McDonell, 2000; Hengl and Reuter, 2008; Pike, 2002; Wise, 1998). Error sources have been summarised as (a) data errors due to not updated data, incomplete density of observations or spatial sampling; (b) processing errors such as numerical errors in the computer, interpolation errors or classification and generalization problems; and (c) measurement errors such as positional inaccuracy (in the x and y directions), data entry faults, or observer bias. The main phases of digital terrain modelling introduce increasing uncertainty in the values (figure 1.1). Often DEM accuracy is quantified using the Root Mean Square Error (RMSE) statistic. To

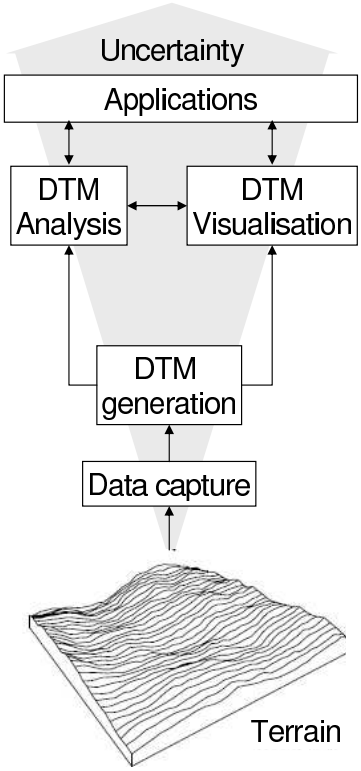

Figure 1.1: Digital terrain modelling and uncertainty (modified from Maune, 2001).

compute the RMSE, differences between the source dataset and co-located values from an independent source of higher accuracy are computed. The RMSE is the square root of the average of these squared differences. The RMSE assumes that DEM errors are random. Because the RMSE is used as a measure of spread, it requires the assumption of normality, which is often violated in the case of the DEM. While a valuable quality control statistic, the RMSE does not provide an accurate assessment of how well each cell in a DEM represents a true elevation. Assessment of DEM uncertainty requires more information on the spatial structure of DEM error beyond that provided by the RMSE.

Topographic attributes frequently used are derived directly from DEMs. DEM errors propagate to derived parameters. The raster grid structure lends itself well to neighbourhood calculations that are frequently used to derive hydrologic and morphological parameters directly from a DEM. Primary surface derivatives such as slope, aspect and curvature provide the basis for characterization of landforms (Wilson and Gallant, 2000). The routing of water over a surface is closely tied to surface form. Flow direction is derived from slope and aspect. From flow direction, the upslope area that contributes to the flow of a cell can be calculated, and from these maps, drainage networks, ridges and watershed boundaries can be identified. Topographic, stream segments order and temperature indices are all secondary attributes computed from DEM data.

The derivatives may be divided into primary topographic attributes, such as slope, aspect, surface curvature, or catchment area, and secondary topographic attributes, such as topographic wetness index, or stream-power index (Wilson and Gallant, 2000). The primary attributes are calculated directly from the elevation data or from one of its derivatives, whereas the secondary attributes are calculated from two or more primary attributes. From the perspective of error propagation analysis, a more useful classification of surface derivatives is one based on their spatial properties rather than their source of calculation. Derivatives based on a fixed neighbourhood may be considered as constrained, while derivatives that are based on far-reaching spatial interactions can be considered as unconstrained. Thereafter, within primary topographic attributes we may find constrained derivatives, such as slope and aspect, and unconstrained derivatives, such as catchment areas.

Flow routing through grid cells of a DEM requires a DEM without disruptions. DEMs often contain depressions that result in areas described as having no drainage, referred to as sinks or pits. These

depressions disrupt the drainage surface, which preclude routing of flow over the surface. Sinks arise when neighbouring cells of higher elevation surround a cell, or when two cells flow into each other resulting in a flow loop, or the inability for flow to exit a cell and be routed through the grid (Burrough and McDonell, 2000). Hydrologic parameters derived from DEMs, such as flow accumulation, flow direction and upslope contributing area, require sinks to be removed. This has become an accepted common practice and many methods are now available (section 1.2 on the next page). Sinks, however, can be real components of the surface. Naturally occurring sinks in elevation data with a grid cell size of $100m^2$ or larger are rare in terrains deriving from fluvial erosion processes. They could occur more frequently in glaciated or karst topographies.

Given spatial data uncertainty, a DEM can be regarded as only one rendering of a distribution of possible realisations. The stochastic simulation approach to error modelling requires a number of maps, or realizations, upon which selected statistics are performed. Uncertainty is computed by evaluating the statistics associated with the range of outputs (Oksanen and Sarjakoski, 2006). In the absence of field collected data other ways have been devised to characterise uncertainty, including using limited elevation values derived from higher resolution DTMs as "ground-truth" data (Kyriakidis et al., 1999), exploring fractal dimensions of DTMs to reveal production artifacts or anomalies (Polidori et al., 1991), or assigning distributions of error for each grid cell based on the reported global error measurements (Fisher, 1993). Representation of these equiprobable distributions of maps is referred to as stochastic modelling (Journel, 1996), or Monte Carlo simulation (Metropolis and Ulam, 1949) due to the random generation of uncertain variables used to simulate uncertainty.

Monte Carlo simulation assumes that the DEM is only one realization of a host of potential realizations. Each cell therefore can be represented by a probability distribution function (PDF) and each cell has a known mean and variance. A value is drawn from the PDF for each cell. This process repeated many times generating a set of realization maps. Each value represents the potential error at a specific point (grid cell). These error maps represent the PDF of the DEMs error distribution, which accounts for the magnitude and spatial dependence of DEM error. Realizations derived from these random fields are used to quantify DEM uncertainty. The Monte Carlo simulation approach as applied to DEMs (section 1.3 on page 5), can be summarized as follows:

a) A random field (error map) is generated based on statistical representation selected for DEM error;
b) The random field is added to the original DEM resulting in a realization;
c) Steps a. and b. are repeated N times based on the number of realizations deemed appropriate to capture the distribution of possible elevations;
d) The distribution of these realizations is evaluated and uncertainty is quantified.

Multiple realizations of the DEM provide a Gaussian distribution that better represents the DEM under uncertain conditions (Hunter and Goodchild, 1997). The underlying assumptions of the Monte Carlo simulation procedure as applied to DEM uncertainty assessment are as follows:

a) DEM error exists and constitutes uncertainty that is propagated with manipulation of the elevation data;
b) The nature and extent of these errors is unknown;
c) DEM error can be represented by a distribution of DEM realizations;
d) The true elevation lies somewhere within this distribution (Lindsay, 2006; Wechsler, 2007).

The uncorrelated representation of error fields as worst case scenarios was refuted by Oksanen and Sarjakoski (2006). Elevation is characterised by spatial dependence, or autocorrelation, therefore elevation errors are spatially autocorrelated. The nature of this autocorrelation is difficult to assess due to the complexity associated with DEM errors and potential anisotropic nature of error. However, methods have been developed to account for spatial autocorrelation in random fields. For example, sequential Gaussian simulation is a geostatistical approach that assumes errors are normally distributed and their distribution can be approximated by using higher accuracy data obtained from ground control points (Goovaerts, 1997; Temme et al., 2008) or from higher resolution datasets (Darnell et al., 2008).

The two following sections detail some sink filling algorithms (section 1.2 on the next page) and the MonteCarlo method (section 1.3 on page 5).

1.2 Sink Filling Algorithms

All hydrologic models ultimately rely on some form of overland flow simulation to define drainage courses and watershed structure (Garbrecht and Martz, 2000). To create a fully connected and fully labelled drainage network and watershed partition, water outflow at every grid cell of the DEM needs to be routed to an outlet on the border of the DEM. Nevertheless, the frequent presence of surface depressions in the DEM prevents simulated water flow from draining into outlets, resulting in disconnected stream-flow patterns and spurious interior sub-watersheds pouring into these depressions. Due to the undesirable results, surface depressions in DEMs are treated as nuisance features in hydrologic modelling. The common practice is to locate and remove surface depressions in the DEM at the very first step of hydrologic analysis. Various algorithms have been proposed to detect and fill surface depressions, such as elevation-smoothing method (Mark 1984), depression-filling algorithms (Jenson and Domingue, 1988; Tarboton et al., 1991), carving method (Soille, 2004b; Soille et al., 2003), or depression watershed method (Chou et al., 2004). Some of them are described hereafter. For a more detailed review it is possible to refer to e.g. Reuter et al. (2008a) or Wang and Liu (2006).

1.2.1 Filling depressions: Traboton et al. (1991)

In the filling depressions method described in Jenson and Domingue (1988, ArcSink in the following text) all single-cell depressions are first filled up by raising each cells elevation to the elevation of its lowest elevation neighbour (pour point). This step reduces the number of depressions that need to be handled in the subsequent steps. Then, flow directions are computed for every cell in the DEM. Special treatment is directed to complex depressions. For the remaining depressions with more than one cell, the interior catchments of depressions are identified and labelled using a flow direction matrix. Instead of filling up depressions one by one, a table of pour points is first built for adjacent interior catchments of depressions. The path of pour points for adjacent depressions is traced until the border of the DEM is reached. Among all pour points on the path, the one with the highest elevation is selected as the threshold. Then, all cells in the interior catchments of the depressions that are lower than the highest pour point are raised to the threshold value.

1.2.2 ANUDEM algorithm

The ANUDEM algorithm is an interpolation method specifically designed for the creation of hydrologically correct DEMs from comparatively small, but well selected elevation and stream coverages (Hutchinson, 1989). The interpolation procedure has been designed to take advantage of the types of input data commonly available, and the known characteristics of elevation surfaces. This method uses an iterative finite difference interpolation technique. It is optimized to have the computational efficiency of local interpolation methods such as inverse distance weighted interpolation, without losing the surface continuity of global interpolation methods such as kriging and splines. It is essentially a discretised thin plate spline technique, where the roughness penalty has been modified to allow the fitted DEM to follow abrupt changes in terrain, such as streams and ridges. The purpose of the drainage enforcement process is to remove all sink points in the output DEM that have not been identified as sinks in the input sink coverage. The program assumes that all unidentified sinks are errors, since sinks are generally rare in natural landscapes (Goodchild and Mark, 1987). The drainage enforcement algorithm attempts to clear spurious sinks by modifying the DEM, by inferring drainage lines via the lowest saddle point in the drainage area surrounding each spurious sink. It does not attempt to clear real sinks. The raster datasets need to be transformed in contour. Then the contour data can be interpolated using an enforcing river network, such as the CCM2 (Vogt et al., 2007). It is implemented in the `TOPOGRID` command of the ESRI softwares.

1.2.3 Filling depressions: Planchon and Darboux (2001)

Although it is designed for analysing the micro-relief of soil surfaces, the filling method described in Planchon and Darboux (2001)is applicable to hydrologic analysis (FillSink in the following text). The algorithm first inundates the surface by assigning a high water surface elevation to all DEM cells and then iteratively drains the excess water from each cell. To find a downslope path for each cell and completely

drain the excess water, the whole DEM is scanned from eight alternating directions. With a seed cell as the root, an upstream tree is progressively searched by following the dependence links, and excess water is removed for all cells on the tree. During the final stage, the water in depressions is drained to the level of the highest pour point on the flow path to an outlet on the border of the DEM, resulting in flat depression surfaces. Water on the cells outside the interior catchments of depressions is completely drained out, and their final elevation values keep the same as before inundation.

1.2.4 Carving

The carving method relies on a flooding simulation. The sinks are not filled, but the terrain is carved to make pits flowing further down (Soille et al., 2003). All spurious minima of the input DTM are identified. If the terrain does not contain any significant natural depression all minima connected to the image border are used as outlets. Carving decreases the elevation of pixels occurring along a path starting from lower elevation pixels.

1.2.5 Optimal hybrid method

An optimal approach combines sink filling and carving (Soille, 2004a) in order to reduce the sum of the differences in elevation between the original DTM and the elaborated one. In the combined approach sinks are filled up to a certain level and then carving proceeds from that level. The level is set according to different criteria. For example: i) minimise the sum of the heights differences between the input and the output depressionless DTM; or ii) minimise the number of modified pixels.

1.3 Probabilistic approach: Monte Carlo simulations

Errors in DEMs will propagate to derived land surface parameters and modelling results in a way that is not easy to predict. Land surface parameters such as slope, aspect, curvature and derived stream network may be more useful measures of the quality of a DEM because they are important derived properties and sensitive to artefacts (Hengl and Reuter, 2008). A high resolution DEM may still have a greater uncertainty than a low resolution one whenever its attributes values are not well defined (Oksanen and Sarjakoski, 2005). It may have a greater potential to describe the landscape, but whether this potential is actually achieved depends on the uncertainty of the attribute value (Oksanen and Sarjakoski, 2005).

The true elevation Z of the considered elevation map (DEM) can be presented as the sum of the measured representation z^* and an unknown error ε:

$$Z(s) = z^* + \varepsilon(s)$$

$Z(s)$ and $\varepsilon(s)$ are random variables and $z^*(s)$ is a deterministic variable. The chosen approach is probabilistic because the true error is not known and it can only be quantify in terms of a probability distribution. In order to characterise ε, the shape of its probability distribution and associated parameters have to be defined. A sensible choice is to assume that ε is normally distributed. This is supported by the so-called Central Limit Theorem. The normal distribution has two parameters, the mean μ_ε and the standard deviation, σ_ε (Webster and Oliver, 2000). The second order stationarity should assume:
1) Constant mean μ_ε;
2) Constant standard deviation σ_ε;
3) Spatial autocorrelation $\rho_\varepsilon(|h|)$ only depending on the distance between points.
It is possible to assume that the systematic error (μ_ε) is constant over the spatial domain and then estimate from sample control point as the average of the observed errors. The standard deviation σ_ε indicates the random error in $z^*(s)$. It can also be estimated from a sample of observed errors at control points, if the assumption of spatially constant standard deviation is taken into account (Temme et al., 2008).

DEM errors are usually spatially autocorrelated, i.e. when the true elevation at some locations is overestimated in the DEM, it is likely that the elevation at a neighbouring location is also overestimated. It is possible to assume that the degree of spatial correlation between $\sigma(s)$ and $\sigma(s+h)$ only depends on the distance of vector h between locations. Then it can be characterised by the correlogram $\rho_\varepsilon(|h|)$.

This will also assume the isotropy, i.e. that the correlation is independent of the direction of vector h between locations (Webster and Oliver, 2000).

When spatial data are used in GIS operations, the errors in the input maps will propagate to the output of the operation. Propagation of attribute errors in spatial modelling can be computed using the Monte Carlo Method. This method is the most often used error propagation method because it is generic and flexible (Burrough and McDonell, 2000).

U is the output of a GIS operation g on m uncertain inputs A_i: $U = g(A_1, ..., A_m)$. The operation g can have different form, but in this case the focus is on the derivation of land surface parameters, where g could be a moving-window operation. The objective of the uncertainty propagation analysis is to determine the uncertainty of the output U given the operation g and the uncertainties in the input attributes A_i (Burrough and McDonell, 2000). The Monte Carlo includes:

1) repeats N times:
   i) Generate a set of realisations a_i from the joint probability distribution of $A_i, I = 1, ..., m$;
   ii) For this set of realisations a_i, compute and store the output $u = g(a_1, ..., a_m)$.
2) compute and store sample statistics for the N outputs u.

The number of realisations N has to be sufficiently large to obtain stable results, but exactly how large N should be depends on how accurate the results of the uncertainty analysis should be. The accuracy of the method is proportional to the square root of the number of runs N. Using a minimal N reduces computing time (Wechsler and Kroll, 2006).

Application of the Monte Carlo method to uncertainty propagation with operation that involve spatial interactions requires that the spatially distributed uncertain inputs are generated in a way that takes into account their spatial correlation. Various methods can be used for stochastic spatial simulations (Goovaerts, 1997). The two more widely used are:

- kriging interpolation of random generated points (Wechsler, 2007). With this method, a point for each locations is generated with normal distribution of mean μ_ε and the standard deviation σ_ε. The points are interpolated using the parameters estimated from variogram analysis of observed errors.

- sequential Gaussian simulation (Goovaerts, 1997; Oksanen and Sarjakoski, 2006). With this method, each cell is visited in a random sequence and at each cell the conditional probability distribution of the variable is computed:

  1) For the first location this is the normal distribution with predefined mean μ_ε and standard deviation, σ_ε. A value from this probability distribution is drawn using an appropriate random number generator and assigned to the location;
  2) At the second location the conditional probability distribution is computed by conditioning the variable at the present location to the value that was sampled at the first location. This is done using simple kriging. The conditional probability distribution at the second location has the kriging estimate as its mean μ_ε and the kriging variance as its σ_ε. From this distribution a value is drawn;
  3) At the third location the conditional probability distribution is calculated again, using the two previous locations in simple kriging.

  The process is repeated until values for allocations have been drawn from their conditional probability distributions (figure 1.2).

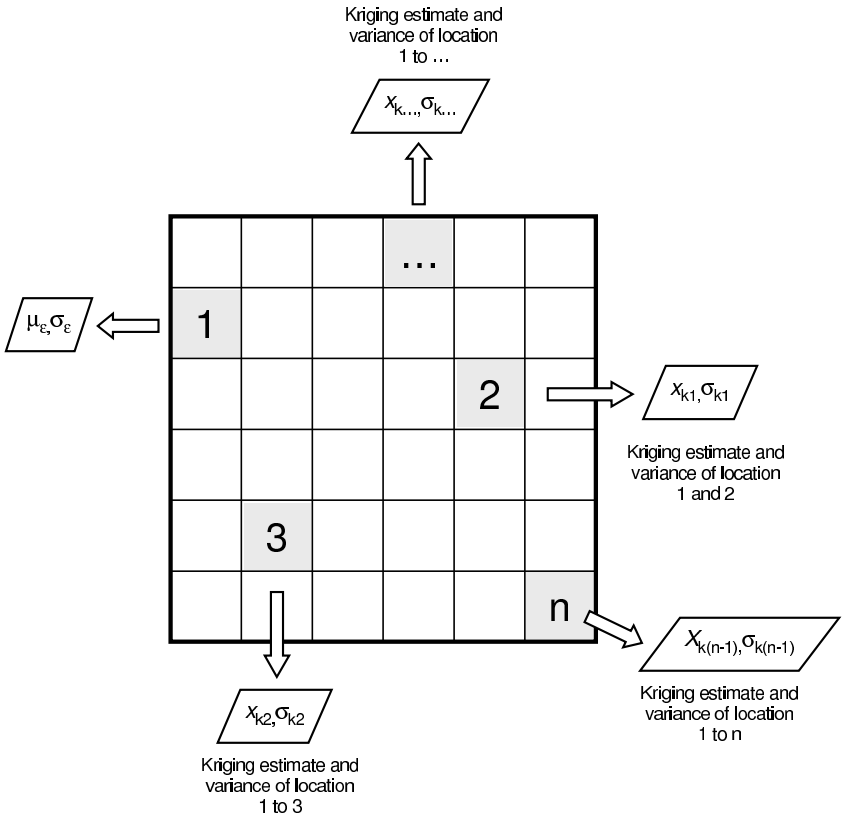

Figure 1.2: Sequential Gaussian simulation (modified from Webster and Oliver, 2000).

2 DTM preprocessing

Three DTMs datasets of different origin and cell resolution were compared, in order to evaluate the influence of original resolution on the derivation of morphological parameters and hydrological features. The influence of different sink filling methods on the original data was evaluated and several morphological and hydrological parameters were derived and statistical analysed. The term DTM is used to refer in general to the datasets considered.

2.1 Input data

The area used for the test is situated in the Rhine basin near the borders of France, Germany and Luxembourg. It present a variety of land uses and morphological characteristics. A subset of approximately 120 km^2 (360 x 364 30m cells) was selected for more detailed investigations (figure 2.1).

2.1.1 Datasets used

The three considered DTMs datasets used had different original cell resolution, origins and error structure:

1. ASTER derived dataset (Data source: JRC/CIAT; Reuter et al., 2008b, c) with original resolution of 30m (figure 2.2a; AST in the following text). The AST Digital Elevation Model product is generated using bands 3N (nadir-viewing) and 3B (backward-viewing) of an AST Level-1A image acquired by the Visible Near Infrared (VNIR) sensor. It has an input Image Resolution of 15 meters and an output Image Resolution of 30 meters.

2. DEM dataset mosaic (EuroDEM, 2008; EuroGeographics, 2008; Hovenbitzer, 2008) from various sources with original resolution of 60m (figure 2.2b; DEM in the following text). It is a digital representation of the ground surface topography of Europe and it describes the distribution of terrain or 'bare Earth' heights, not including 'first surface' elevations such as vegetation and man made structures.

3. SRTM dataset (Jarvis et al., 2006) with original resolution of 100m (figure 2.2c; SRTM in the following text). The SRTM digital elevation data were originally produced by NASA. It has a resolution of three arc seconds. The dataset used was further processed from the original NASA DEMs to fill in no-data voids. The processing included: (i) the support for auxiliary information, (ii) the use of a void region specific processing over a tile based processing (Reuter et al., 2007), and (iii) use of SWDB V2 water body database.

The datasets, if necessary, were resampled to a common resolution of 30m in the European LAEA projection (Annoni et al., 2003) using cubic convolution (Keys, 1981). The datasets were pre-processed in order to reach a certain level of homogenisation. The procedures common to all datasets were:
- mosaiking of scenes available;

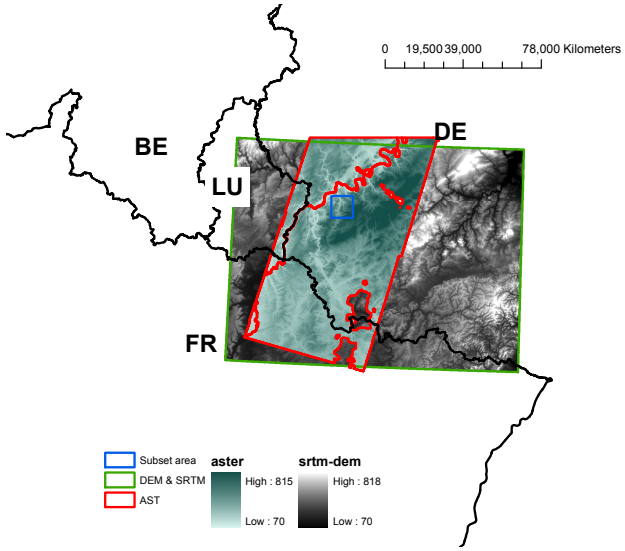

Figure 2.1: Test area selected and datasets available.

- projection to the ETRS89-LAEA projection (Annoni et al., 2003);
- coregistration of the datasets.

Two tiles of SRTM and DEM datasets and the four scenes of AST one were mosaicked using the built-in `mosaic` tool of the ESRI GIS software. The background values were set as no-data and the default values for no-data was selected. In the overlapping region the mean of the values was used. In order to fill the large voids in the AST dataset the ANUDEM algorithm was used (Reuter et al., 2007) as implemented in the ESRI `topogrid` tool. The interpolated data were used only to fill the voids, while the original data were kept where existing (Vrščaj et al., 2007). All datasets were converted to ETRS89-LAEA using the ESRI `project` command for raster. The resampling technique used was the `cubic convolution` (Keys, 1981) that uses the 16 nearest input cell centres and their values to determine the output cell value with a smooth curve fitted through the points to find the value at the output cell centre. The datasets were coregistered twice:
1) before the projection and consequent transformation. The ENVI `coregistration` tool was used;
2) after the projection, using the ESRI `georeferencing` tool.
In both cases the RMS errors were below 0.2.

2.1.2 Ancillary data

Some ancillary data were used:
- Corine land cover 2000 (CLC2000) 100 m - version 9/2007. It provides information on land uses in the considered area. (`http://image2000.jrc.it/`)
- CCM2, version 2, window 2003 (Vogt et al., 2007). It includes a hierarchical set of river segments and catchments based on the Strahler order, a lake layer and structured hydrological feature codes based on the Pfafstetter system. It provided information on river basin border and stream network. (`http://agrienv.jrc.it/activities/catchments/`)
- SRTM 100 (Jarvis et al., 2006). It is the original SRTM dataset with a resolution of about 100 m in LAEA projection. (`http://srtm.jrc.it/`)
- panchromatic images from IMAGE2000 (Nunes de Lima, 2005) with a resolution of 12.5 metres. (`http://image2000.jrc.it/`)

Table 2.1: Land use groups.

Land use code	Corine Code	Land use
11	111, 112	Urban fabric
12	121, 122, 123, 124	Industrial, Commercial, transport
13	131, 132, 133	Mine, dump and construction sites
14	141, 142	Artificial, non-agricultural vegetated areas
21	211, 212, 213	Arable land
22	221, 222, 223	Permanent crops
23	231	Pastures
24	241, 242	Heterogeneous agricultural areas
25	243, 244	Agro-forestries
31	311	Broad-leaved forest
32	312	Coniferous forest
33	313	Mixed forest
34	321, 322, 323, 324	Scrub and/or herbaceous vegetation
35	331, 332, 333, 334	Open spaces with little or no vegetation
41	411, 412, 421, 422, 423	Inland wetlands
51	511, 512, 521, 522, 523	Inland waters

Table 2.2: Slope classes and landforms classification.

Slope classes		Landforms	
1	0-2 %	-8	Pit
2	2-5 %	-6	Channel
3	5-8 %	-1	Concave Hill-Slope
4	8-15 %	0	Plan Hill-Slope
5	15-30 %	1	Saddle
6	30-45 %	2	Convex Hill-Slope
7	45-60 %	7	Ridge
8	60 %	9	Peak

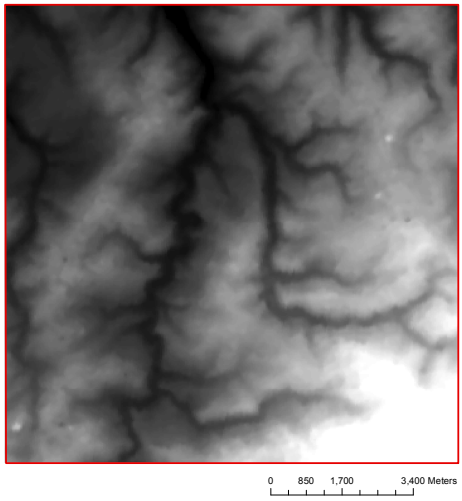

(a) AST (Reuter et al., 2008b)

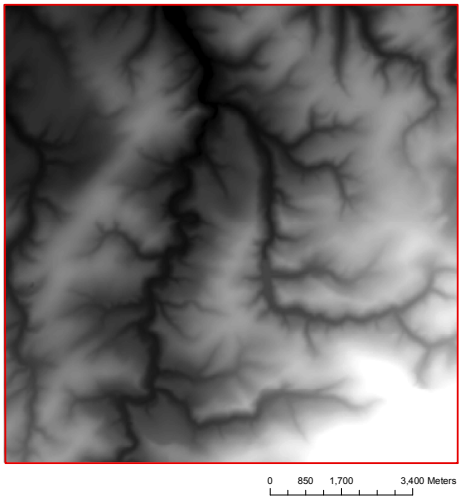

(b) DEM EuroDEM (EuroDEM, 2008; Hovenbitzer, 2008) © EuroGeographics and *Bundesamt fër Kartographie und Geodäsie*.

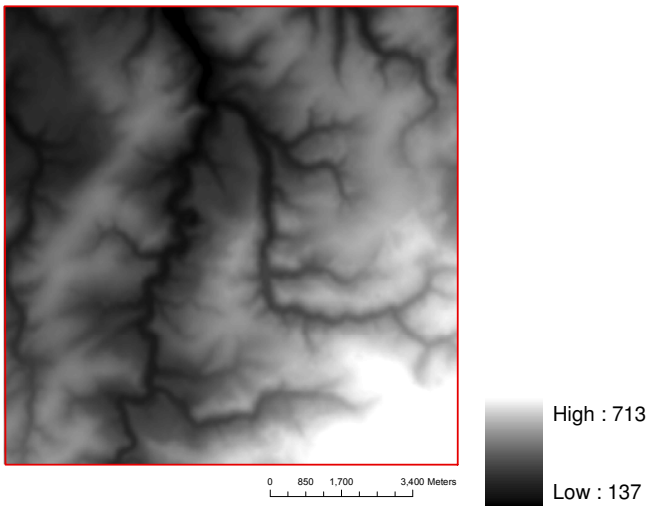

(c) SRTM (Jarvis et al., 2006)

Figure 2.2: Dataset used in the subset area, highlighted by a blue frame in figure 2.1 on page 9.

Table 2.3: Sink density.

	Sink density(km^2)	Max Depth
AST	2.87	173
Aster-No-Voids	1.23	173
DEM	1.44	40
SRTM	2.46	40
SRTM100	0.61	82

2.2 Sink removal and filling algorithms

In order to obtain a functional flowing dataset sinks and peaks have to be removed. Different algorithms exist in order to create a depressionless dataset. In this case the following methods were considered:

- ArcSink (Jenson and Domingue, 1988). The method is implemented in the `fill` tool of ESRI software. the sink depth was calculated using the `sink` tool (Tarboton et al., 1991).
- FillSink (Planchon and Darboux, 2001). The method is implemented in the SAGA (`http://www.saga-gis.uni-goettingen.de/html/index.php`) software.
- Carving (Soille, 2007).
  - morphological filling (F1 in following text). It fills the sink using the graph-connectivity (Soille and Ansoult, 1990).
  - carving (F2 in following text). It performs the carving on the dataset (Soille, 2004a).
  - optimal (F3 in following text). It performs the optimal removal of all internal pits of the datset using the methodology described in Soille (2004b).
- ANUDEM (Hutchinson, 1989). The method is implemented in the `topogrid` tool of ESRI.

A modere detailed description of methods can be found in section 1.2 on page 4. The number of sinks in the raw datasets and remaining after the filling process was calculated using the `sink` tool of ESRI. All methods tested for sink filling, except ANUDEM, removed all sinks. The ANUDEM interpolator greatly reduce the number. Table 2.3 shows that the AST and SRTM datasets have the highest density of sinks. The DEM has a considerable minor number of sink, as the AST with filled voids.

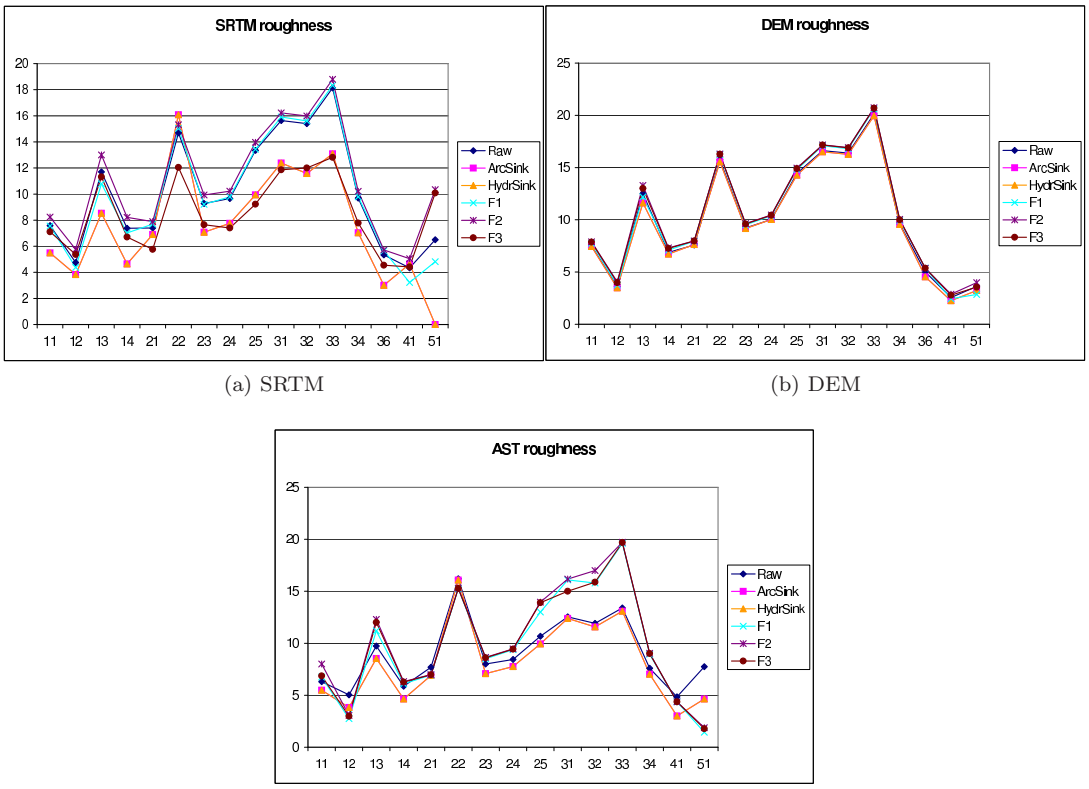

(a) SRTM (b) DEM

(c) AST

Figure 2.3: Roughness Index for considered datasets and the land use groups detailed in table 2.1.

2.3 Landforms derivation

The three DTMs datasets were compared in the derivation of terrain landforms and morphological parameters, such as slope, curvature, aspect, topographic wetness index and other morphological parameters.

2.3.1 Methods used

In order to compare the behaviour of the datasets, different parameters were derived. The methods and algorithms used are:
- Slope: D8 algorithm (Fairfield and Leymarie, 1991)
- Curvature (Moore et al., 1991). It represent the rate of change of slope for each cell.
- Aspect: identifies the direction of maximum rate of change in z value from each cell
- Topographic Wetness Index (TWI; Sorensen et al., 2006). It is calculated as:

$$\mathrm{TWI} = \ln \frac{CDA}{\tan \Delta}$$

The slope, curvature and aspect were calculated using the `slope`, `curvature` and `aspect` ESRI commands respectively.

The parameters calculated were analysed in more homogeneous regions. The zones were defined according to i) land uses group derived from CLC2000 (table 2.1 on page 10), ii) slope classes and iii) landforms (table 2.2 on page 10). The landforms were derived using the algorithm described by (Peucker and Douglas, 1975). The statistics were performed using the `zonalstatistics` tool of ESRI.

2.3.2 Roughness Index

The topographic roughness index (TRI; Blaszczynski, 1997; Reuter et al., 2006; Riley et al., 1999) is a measurement to express the amount of elevation difference between adjacent cells of a digital elevation

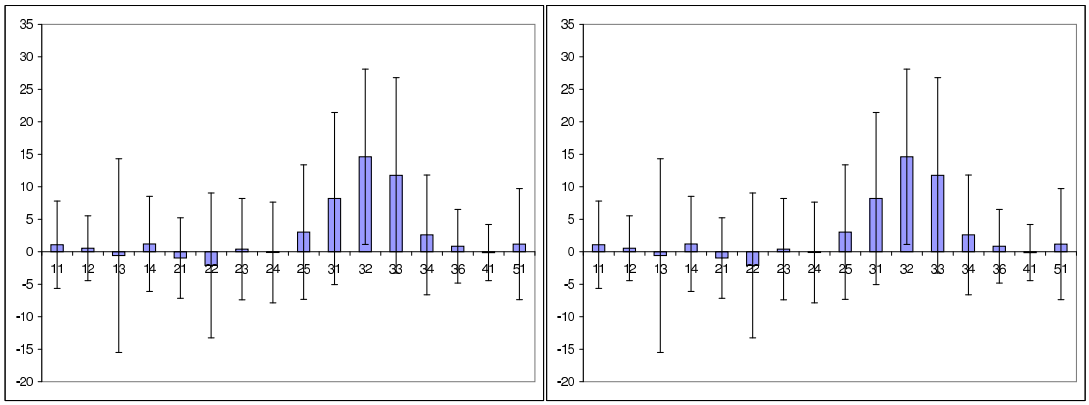

(a) SRTM and DEM (b) SRTM and AST

Figure 2.4: Variability of differences in heights for the land use groups detailed in table 2.1.

grid. The process essentially calculates the difference in elevation values from a centre cell and the eight cells immediately surrounding it. Then it squares each of the eight elevation difference values to make them all positive and averages the squares. The topographic roughness index is then derived by taking the square root of this average, and corresponds to average elevation change between any point on a grid and its surrounding area.

The index was calculated for the raw data and for the datasets filled with the different considered methods. The filling algorithms did not change significantly the roughness of the original datasets. However some differences among algorithms and datasets can be highlighted (figure 2.3). The filling algorithms (ArcSink and HydrSink) behave exactly the same, with a minor reduction of roughness in case of SRTM and AST datasets. No significant changes can be seen in the DEM datasets for all algorithms used. The carving algorithms behave slightly different for SRTM and AST dataset. In the SRTM dataset F1 and F2 maintain the roughness as in the raw data. F3 behave similarly to the other filling algorithms. In the AST dataset, the carving algorithms behave similarly to the other filling algorithms in most of the land uses groups, but they increase the dataset roughness in the forest land use groups.

2.3.3 Morphological parameters

The considered landforms parameters were derived for raw data and filled datasets. The results (figure 2.4) show a high standard deviation, indication of a high variability that makes difficult to statistically separate the different results in populations.

Figure 2.5 represents the differences of heights, slopes, aspect and curvature for the datasets according to homogeneous land use groups. The main differences in heights (figure 2.5a) appears in urban and forested land uses, with SRTM > DEM > AST. The differences calculated for slope (figure 2.5a), aspect (figure 2.5b) and curvature (figure 2.5c) did not show a clear pattern. However it is possible to see that the higher differences are found in urban land uses and in forested and water areas where differences are less reliable as the water surface is flat.

The differences of heights for slope classes (figure 2.6a) do not present significant differences for DEM and AST data, the two datasets with higher resolution. The SRTM presents important differences, increasing in steeper regions. The differences calculated for landforms do not present any significant difference (figure 2.6a).

The differences in heights for the filling methods tested are presented in figure 2.7. In case of the differences between SRTM and DEM (figure 2.7a) the raw data, the results from ArcSink and FillSink methods are overlapping, while there are some differences for the other methods used in forested land use and in water bodies. In case of comparison of SRTM / AST (figure 2.7b) and DEM / AST (figure 2.7c) all the filling algorithms behave in the same way with overlapping curves. The main differences with raw data occur in case of forested land uses and water bodies.

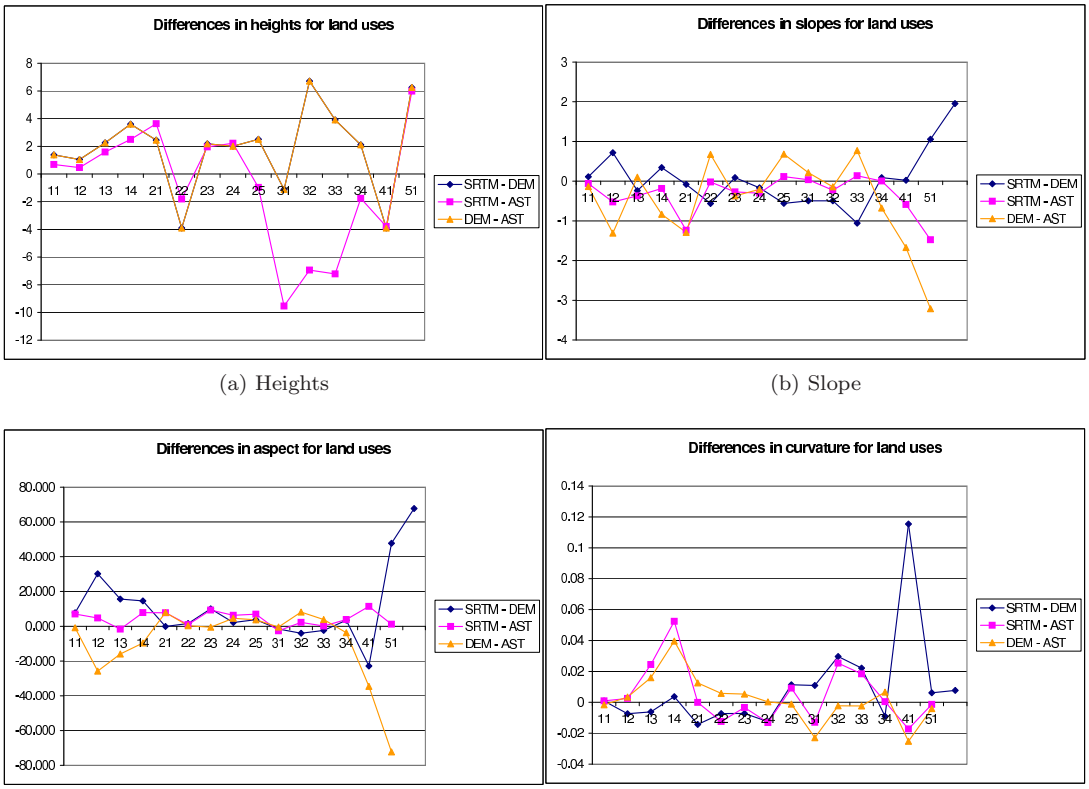

(a) Heights (b) Slope

(c) Aspect (d) Curvature

Figure 2.5: Differences of heights and morphological features in land use groups.

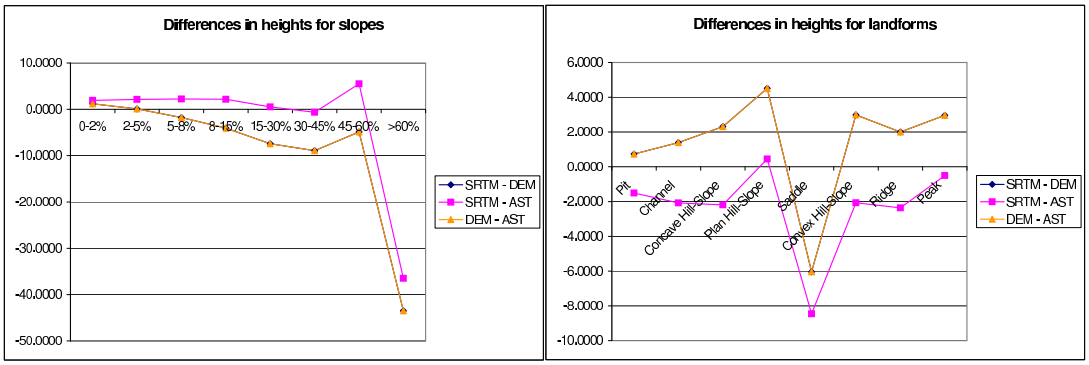

(a) Slopes (b) Landforms

Figure 2.6: Differences of heights in slope and landforms classes.

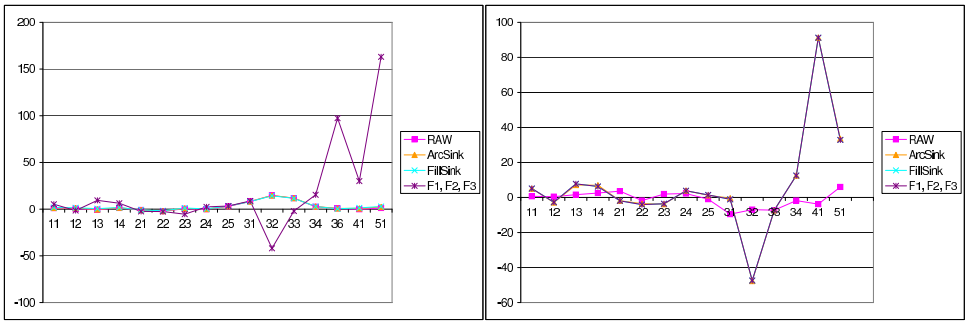

(a) SRTM & DEM

(b) SRTM & AST

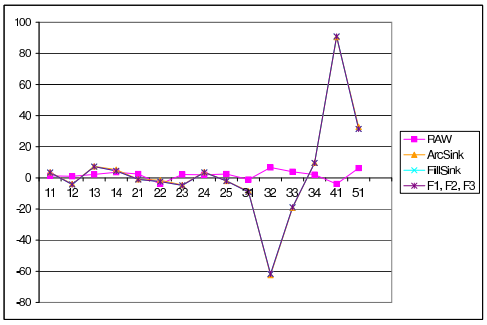

(c) DEM & AST

Figure 2.7: Differences in heights for filling methods.

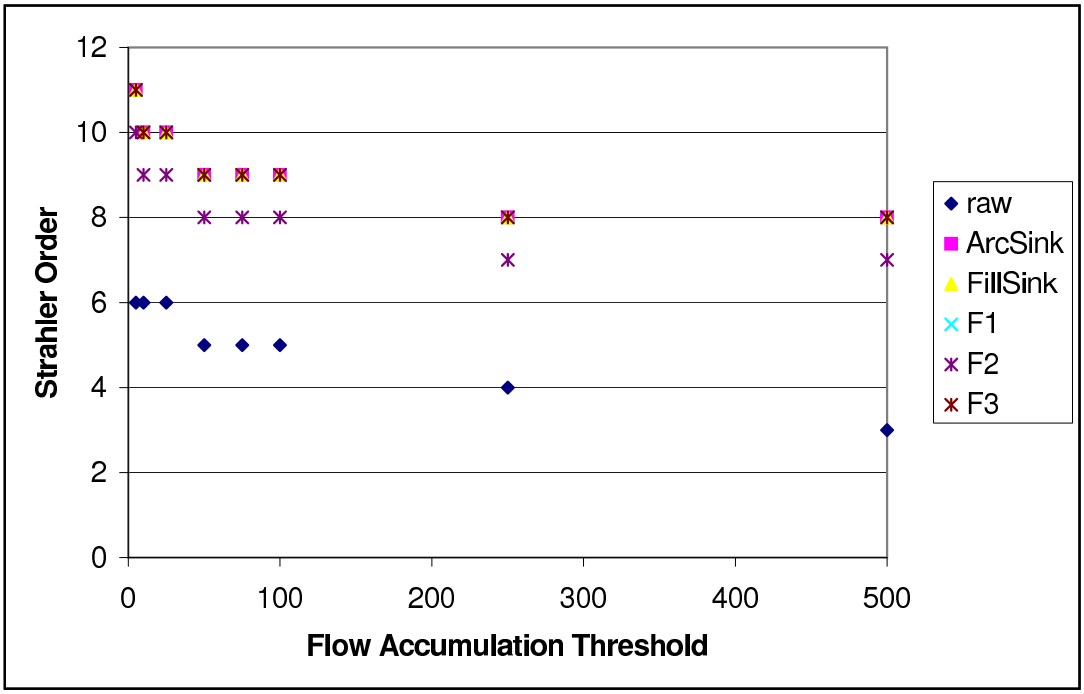

Figure 2.8: Difference in filling algorithms for SRTM. The other datasets have similar trends.

2.4 Extraction of river network features

The derivation of hydrological parameters and features such has stream segments, watershed divides and related information was compared for the three different DTMs considered.

2.4.1 Methods used

In order to compare the behaviour of the datasets, different parameters were derived:
- Flow direction
- Flow accumulation
- Stream network
- River order

The flow direction and the flow accumulation were calculated using the `flowdirection` , `flowaccumulation` ESRI commands based on the D8 methodology (Fairfield and Leymarie, 1991). The stream network was defined as all cells with a flow accumulation value higher then a predefined threshold. The river order was defined using the `streamorder` command in ESRI, choosing the method of stream ordering proposed by Strahler in 1952 in which stream order only increases when streams of the same order intersect. Therefore the intersection of a first order and second order link will remain a second order link rather than create a third order link.

2.4.2 Strahler order and contributing drainage area

The river networks were extracted from the raw data and from the datasets filled with the different tested methods, excluding ANUDEM. The river networks were extracted using different flow accumulation thresholds and then the Strahler order was computed. The considered filling methods behave all in a similar way (figure 2.8). It is possible to see some small differences for the F2 (carving) method. The differences could be explained by the different approach of the method used (1.2.4 on page 5). The three datasets showed similar patterns for the methods considered (figure 2.9). The DEM always reached the highest order in the comparison, while the SRTM reached a significantly lower order. The AST dataset with the highest original resolution was expected to reach the highest order, but it always reached one order less than the DEM.

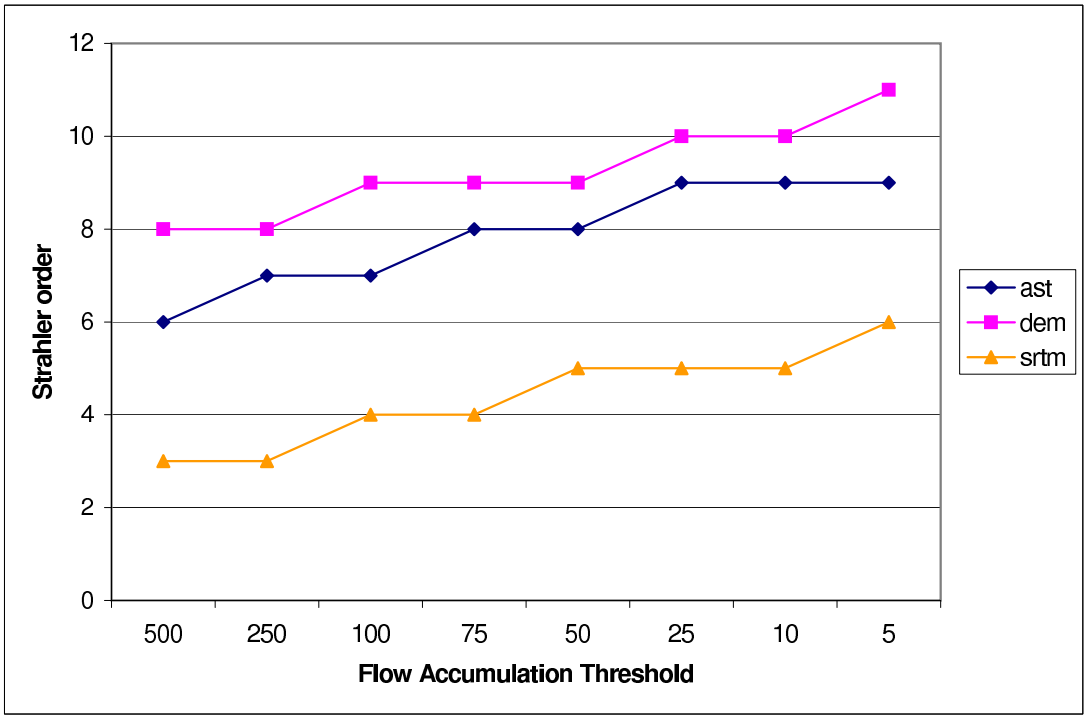

Figure 2.9: DEMs Strahler order.

The contributing drainage area (CDA) was computed and expressed as the number of pixel for each Strahler order. Figure 2.10 shows that AST dataset has always a much higher CDA for lower Strahler order, with a steeper curve. This seems to be due to flat areas where, in case of AST, more parallel streams are derived (figure 2.11). In figure 2.13 are presented the flow direction and the flow accumulation for considered datasets in a flat region. The flow direction map of AST (figure 2.12a) is very homogeneous in the considered area, but more details are visible in the upslope regions. The AST dataset seems to have a more detailed micromorphology (figure 2.2 on page 11) that could initialise a higher number of stream for the same flow accumulation threshold. This could be confirmed from the flow directions maps were is AST has a clear different trend (figure 2.13a). The behaviour of AST in flat regions could explain why it does not reach Strahler orders as high as the DEM.

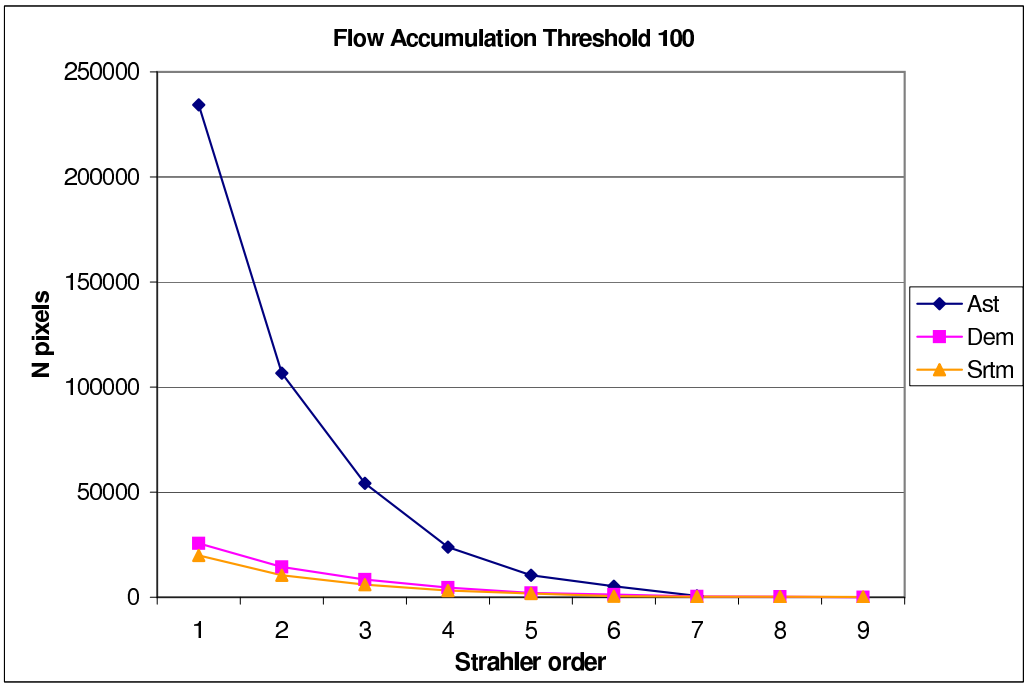

(a) CDA = 100

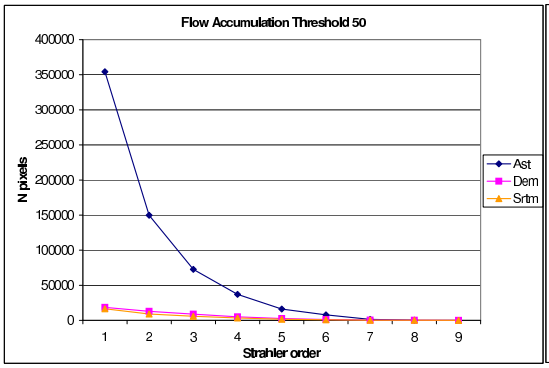

(b) CDA = 50

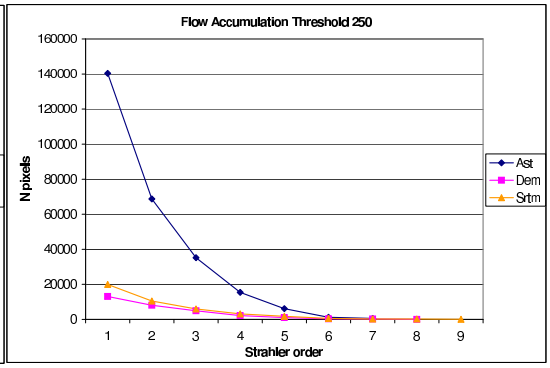

(c) CDA = 50

Figure 2.10: CDA for different flow accumulation thresholds.

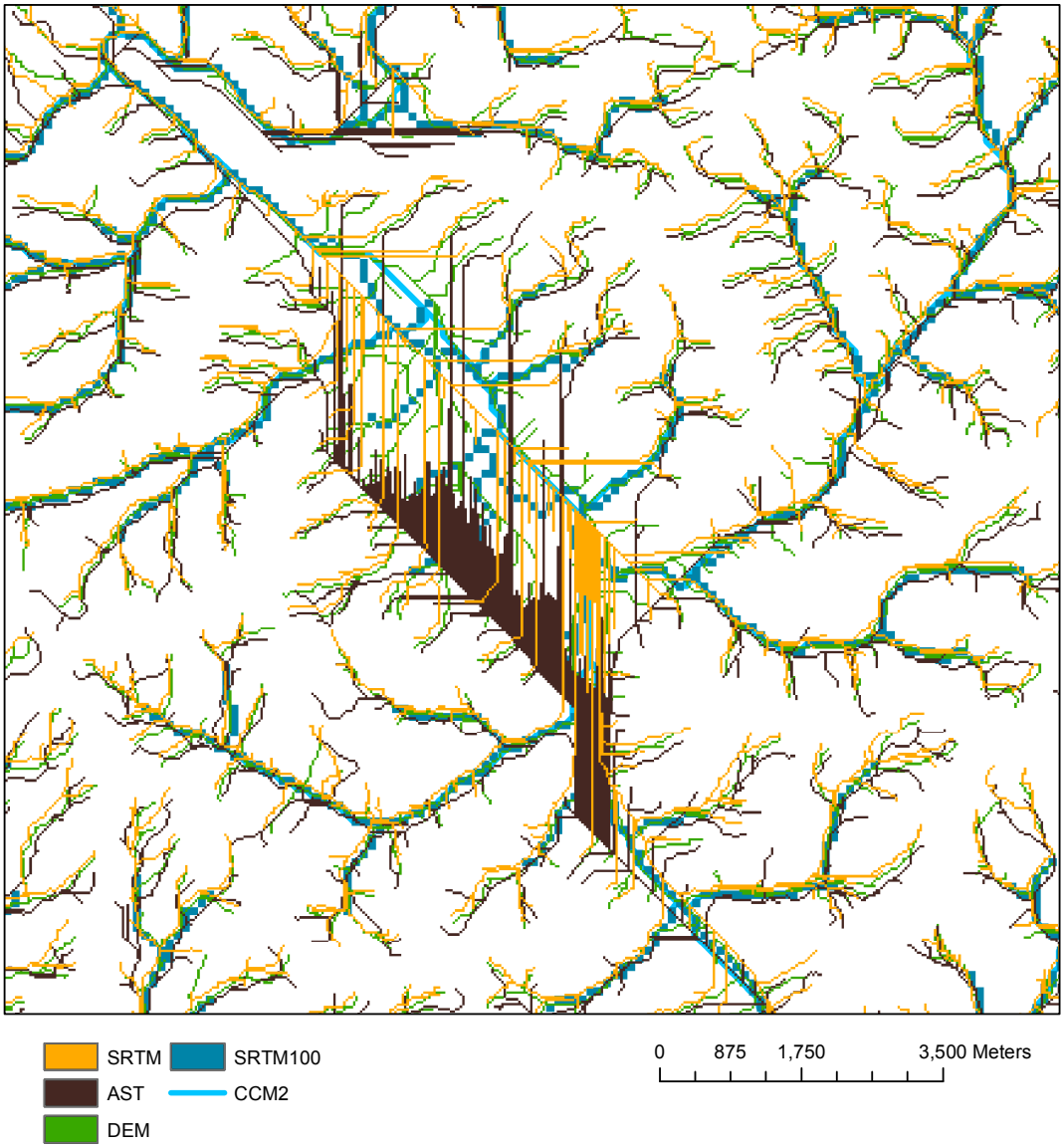

Figure 2.11: Extracted river networks in flat regions.

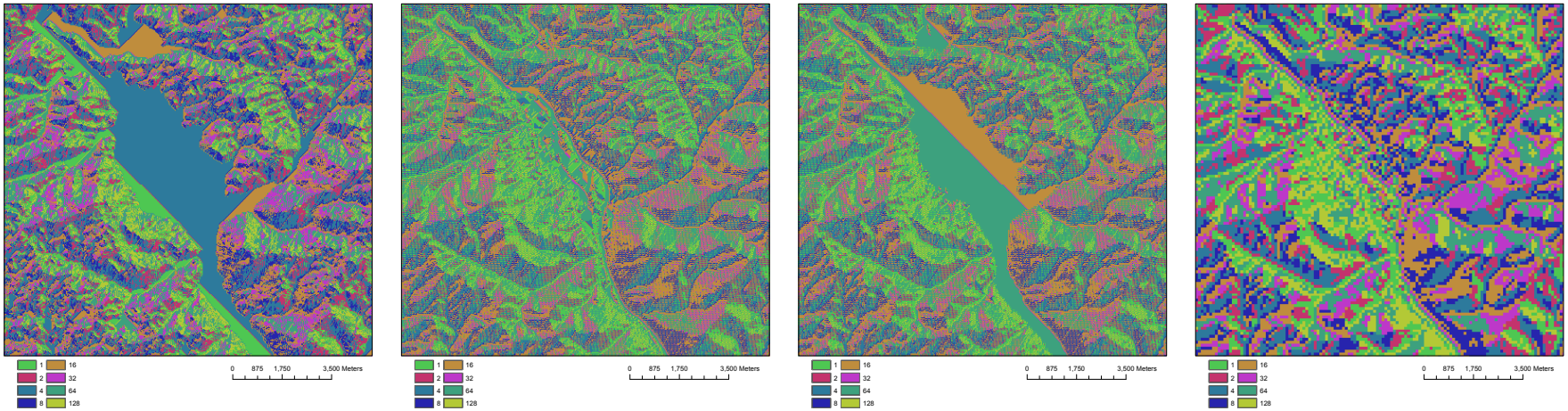

(a) AST (b) DEM (c) SRTM (d) SRTM100

Figure 2.12: Flow directions for the considered datasets in a flat region.

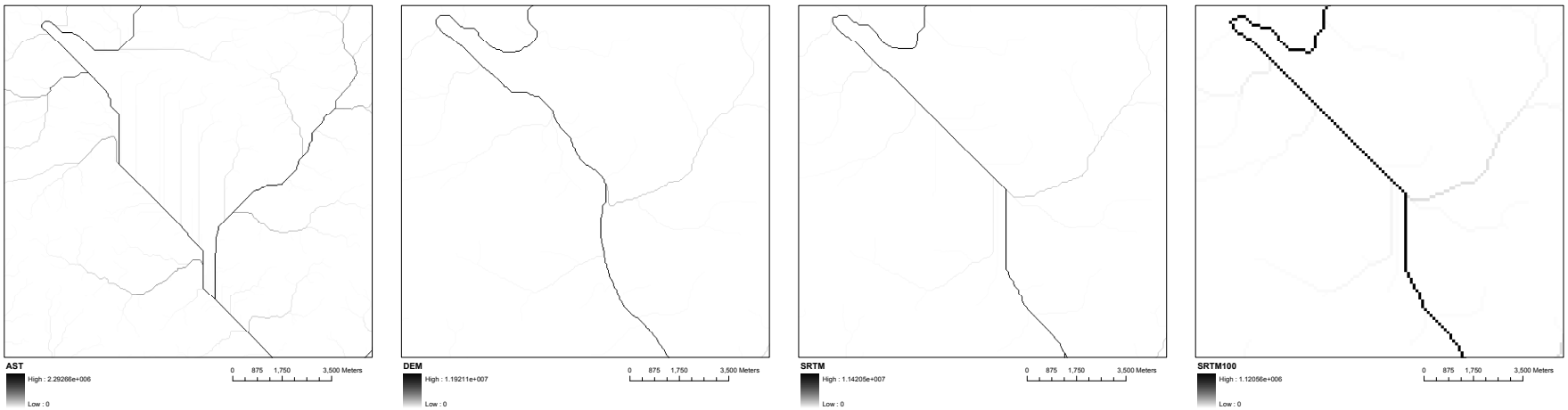

(a) AST (b) DEM (c) SRTM (d) SRTM100

Figure 2.13: Flow accumulation maps for the considered datasets in a flat region.

3

Simulations and hydrological features extraction

The DEM errors can be understood as the difference between two topographical surfaces. The basis for using the Monte Carlo method in error propagation analysis is that the original data is perturbed repeatedly by the realisation of the modelled error, and the GIS analysis is calculated from the perturbed data set. Finally, statistical summaries are drawn from the stack of analysis results based on the perturbed data sets. Several features were extracted from the error modelled surfaces. The features were analysed statistically and spatially.

3.1 Error propagation method

The error propagation was analysed on a subset of the test area, of about 120km^2 (figure 2.2 on page 11), using Monte Carlo approach with consideration of spatial variability of the errors. The method used is sketched in figure 3.1.

The procedure can be broken down in three main steps:

1. **Errors calculations**. The errors of the datasets were calculated as the difference between the data and a reference dataset considered as the ground true value.

2. **Modelling of errors**. The errors models obtained were statistically and spatially analysed. The spatial analysis consisted in assessing the spatial variability of the error in order to derive a kriging model. The model was then applied to the random generated noise, in order to preserve the spatial structure of the errors.

3. **Simulations**. The simulated errors were then added to the original dataset:

$$\text{Simulated DTM} = \text{DTM} + \text{kriged error}$$

Several parameters were derived from each dataset at each iteration:
- slope as example of first order derivative
- topographic wetness index (TWI) as example of second order derivative
- stream network and order
- watershed borders

The model was run 100 times as compromise between computation costs and explained variance (section 3.1.2 on page 25) and several summarising parameters were collected and analysed. The average, standard deviation and coefficient of variation were calculated for slope and TWI. The variability of the stream networks was characterised by:

i) Number of time a cell was considered to be part of the network;
ii) Percent of cells that were part of the network a given number of times;
iii) Average and standard deviation for number of segments and length for each order.

The derivation of watershed was summarised with:

i) Number of watersheds

Table 3.1: Error models analysis: parameters.

	AST	DEM	SRTM
μ_ε	6.64	-6.96	-0.03
σ_ε	30.90	17.77	25.75
Lag (m)	510	510	510
Range (m)	260	6380	310
Nugget	17.30	25.73	15.6
Partial Sill	107	25.74	102.1

ii) Number of time a cell was considered to be part of a watershed border
iii) Percent of cells that were part of a watershed border a given number of times

3.1.1 Error model analysis

The statistical distribution of the errors was described through the mean (μ_ε) and the standard deviation (σ_ε) of the differences between the considered dataset and the reference one. The reference was calculated as the average of the 3 available datasets. The use of the mean of existing datasets could introduce some errors and noise disturbance, but it was the most consistent method according to the available data. The use of the average of the other two datasets as reference was considered and tested but the results were not satisfying. The calculated values of mean and standard deviation were used to generate a point dataset of random values with mean and standard deviation equal to the previously calculated values, μ_ε and σ_ε. The ESRI `create random raster` was used.

In order to simplify the analyses, the assumption that the modelling of the DTM error was possible with a second-order stationary Gaussian random field was made. That included the fact that the DTM error was assumed to be independent of external factors and additionally free of any systematic errors (Oksanen and Sarjakoski, 2006). The exponential and Gaussian spatial autocorrelation models (Cressie, 1993) were selected to represent the correlation structure of the DTM error. The exponential model has been found to be realistic in earlier works (e.g. Holmes et al., 2000). The spatial variability and structure were modelled through the variogram analysis of the data. For each dataset a model was derived and defined in terms of (i) lag distance; (ii) range; (iii) nugget; (iv) partial sill.

The derived parameters were then used with the ordinary kriging interpolation method on the previously generated random noise in order to impose the dataset spatial structure on the generated noise. The ESRI `kriging` tool was used, inserting the variogram parameters calculated. The results show (table 3.1) that a certain spatial correlation is present in all the considered datasets. The parameters resulting from the analysis of AST and SRTM datasets show a short range and a nugget that is significantly smaller then the sill (figure 3.2). The DEM shows a much higher range and a nugget that is about 50% of the sill with a less clear exponential model (Cambardella et al., 1994).

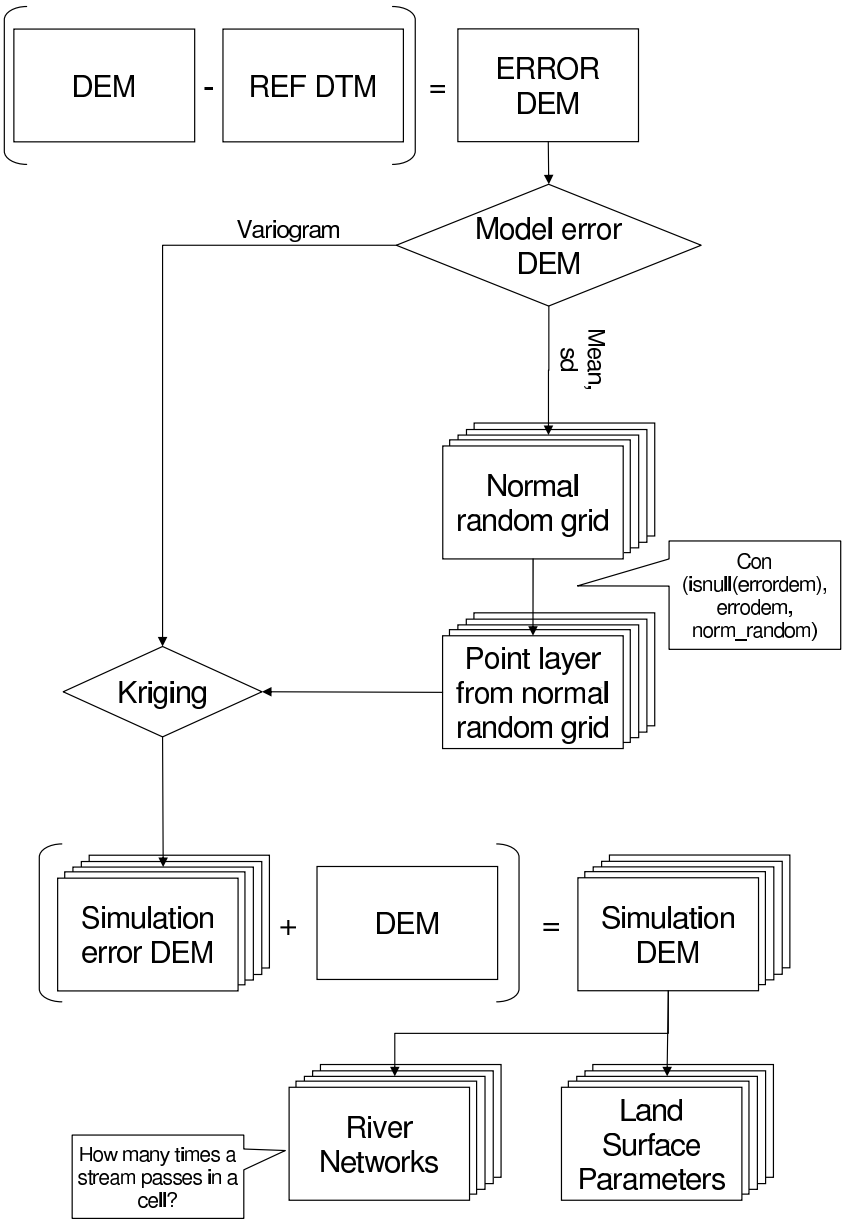

Figure 3.1: Flow chart of the error propagation method.

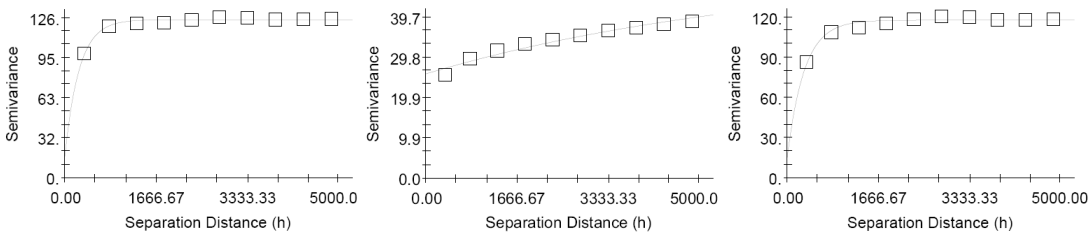

(a) AST (b) DEM (c) SRTM

Figure 3.2: Error models analysis: variograms.

Table 3.2: Explained variance and confidence levels.

N'=500	AST	DEM	SRTM
Explained variance % at N'=100	92.62	94.95	92.72
N' for 95% explained variance	238	104	226

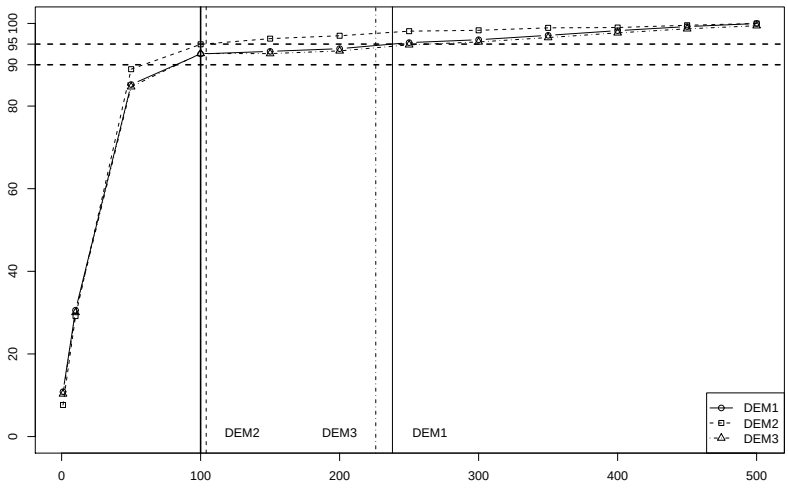

Figure 3.3: Standard deviation for N' = 500 iterations and explained varaince for considered DTMs.

3.1.2 Number of iterations and confidence level

The number of iteration (N = 100) was chosen arbitrarily as a compromise between computation costs and explained variance. In order to calculate the variance explained by the model, and thus the confidence level of the results, a high number (N' = 500) of random DTMs was calculated for each dataset:

$$\text{random DTM} = \text{DTM} + \text{random noise}(\mu_\varepsilon, \sigma_\varepsilon)$$

where $\mu_\varepsilon, \sigma_\varepsilon$ are the mean and the standard deviation of the errors calculated as in the previous section. The standard deviation of all 500 random DTMs was calculated and considered as the total variation. Then the standard deviations of $N' - 1$, $N' - 2$, $N' - ...$ were calculated. This method is often applied in order to determine the m minimum number of iterations, reached when the standard deviation of $N' - m$ is below a given threshold (Wechsler and Kroll, 2006). In this experiment the value of $N' - 100$ was taken as the explained variance of the model.

Figure 3.3 shows the result for the considered datasets. The values of explained variance for 100 iterations (solid line in the figure) are always above 90%. The detailed values are indicated in table 3.2 with the number of iterations that would have been necessary to reach the 95% confidence level, other value often used (dotted lines in the figure). In this latter case, the DEM datasets needs less then the 50% of the iterations needed by AST or SRTM datasets.

Table 3.3: CDA and FA values for considered DTMs.

	AST	DEM	SRTM	SRTM100
CDA (m^2)	7000	10500	7500	7300
FA (m^2)	177	203	153	155

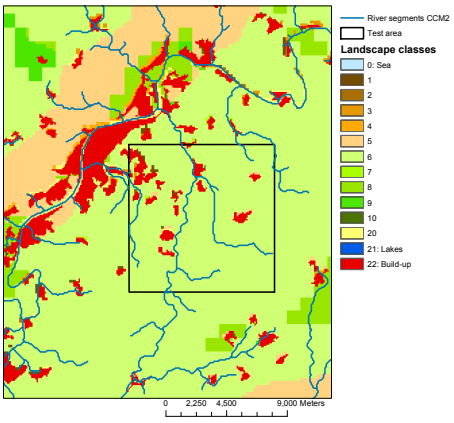

Figure 3.4: Landscape classes for the test area (Vogt et al., 2007).

3.1.3 CDA threshold calculation

In order to analyse the critical Contributing Drainage Area (CDA) threshold a diagram of local slope versus CDA was prepared. Many studies used the log-log linear relationship between local slope and CDA as computed from DTM in order to infer an adequate threshold (e.g. Hancock, 2005; Tarboton et al., 1991). The slope was derived from raw non sink-filled data. The CDA was derived from sink filled data with optimal hybrid carving method. Both the local slope and the CDA were computed using the D∞ methods (Tarboton, 1997) which allows for flow dispersion. The plot was generated using all the cells values in the test area and analysed with dedicated software (Colombo et al., 2007; Vogt et al., 2007, 2003). The cell values were aggregated by binning 800 samples and the average and standard deviation of each bin was calculated. The relationship between slope and CDA is shown in figure 3.6 for the three considered datasets. In the graphs it is possible three main sections with different scaling responses (Vogt et al., 2007):
1) increasing slope
2) constantly decreasing slope
3) straight part with theoretical slope of -0.5
Section two and section three are separated by a *breakpoint* were the slope is slightly increasing. The breakpoint is often used to define the critical CDA threshold. In this case the breakpoint was selected visually and it is around 10,000m^2 for all datasets (table 3.3).

The critical threshold so defined was calculated using the D∞ method, while the flow accumulation (FA) threshold used in the model simulations was obtained with the D8 method implemented in the ESRI `flow accumulation` tool (Jenson and Domingue, 1988). In order to compare the values a regression was performed between the CDA (D∞) and the FA (D8) values. All the cell values of the input area were considered and then aggregated in bins, as in the analysis of the slope versus CDA. Figure 3.6 displays the regression relationships and the derived equations.

The detailed values of CDA and the values of FA derived through the regression are presented in table 3.3. According to the landscape stratification of Vogt et al. (2007), the selected area belong almost completely to class six (figure 3.4), with an average aptitude to develop drainage channels. The CDA value calculated for this class at continental scale is 4.80 km^2 (Vogt et al., 2007), thus much larger than the values obtained at local scale in the tested area.

The CDA values calculated locally vary according to the considered dataset. The SRTM value for the resampled dataset is rather similar to the one obtained locally for the original SRTM.

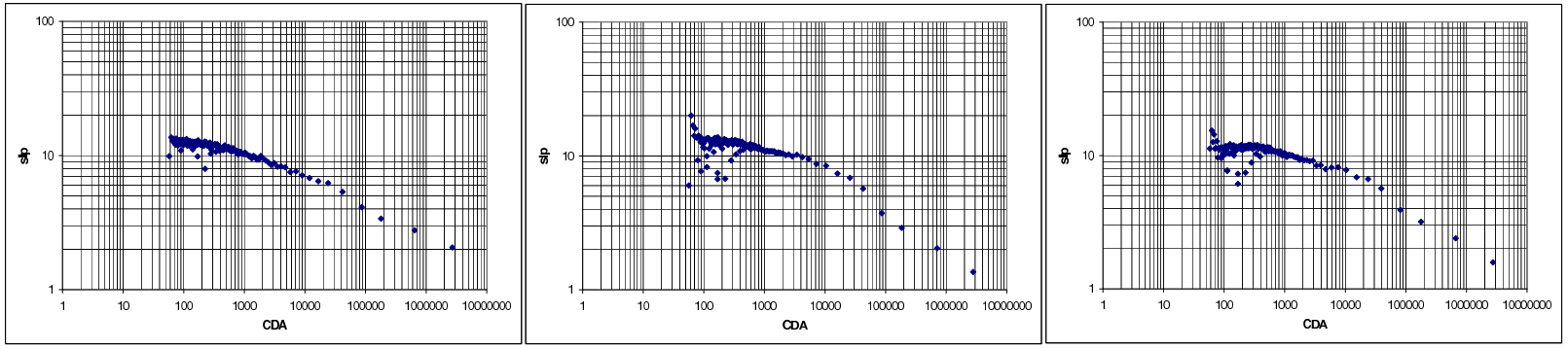

(a) AST (b) DEM (c) SRTM

Figure 3.5: Log-log plot of local slope (degree) vs CDA (m^2).

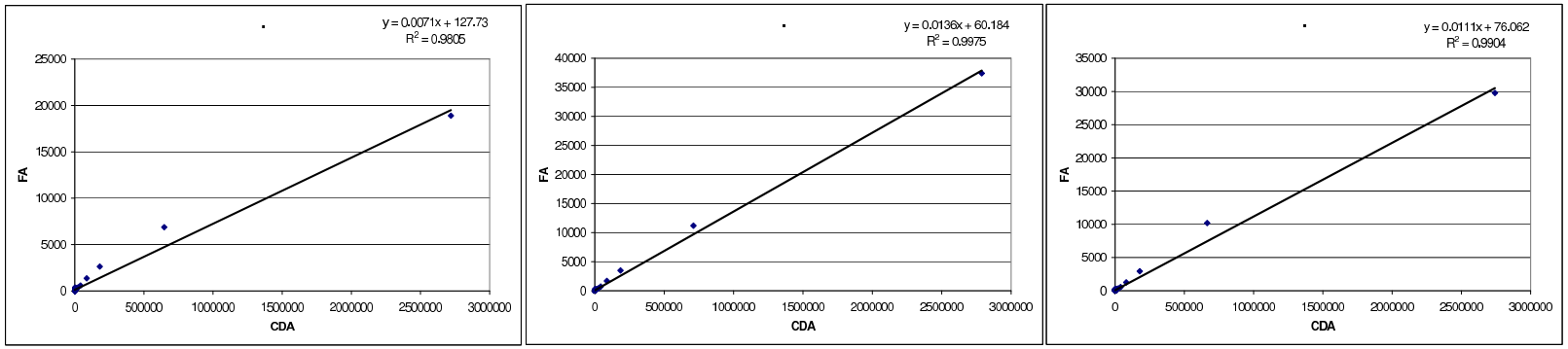

(a) AST (b) DEM (c) SRTM

Figure 3.6: Regression relationships for CDA and FA.

3.2 Probabilities

The simulated DTMs were used to extract river networks and watershed divides. The error propagation analysis allowed to get information about the confidence level of derived features and probabilities of extracted parameters.

3.2.1 Methods proposed

In order to create a depresionless dataset the simulated DTMs were treated with the filling algorithm implemented in ESRI `fill` tool (Jenson and Domingue, 1988; Tarboton et al., 1991). Flow directions and flow accumulations were calculated using the D8 method (Fairfield and Leymarie, 1991) as implemented in `flowdirection` and `flowaccumulation` tools respectively.

The river network was defined as all cells with a flow accumulation value higher then 100 pixels. The threshold was set arbitrarily, as compromise between the characteristics of the three datasets used. The ridge cells were identified as the cell where the flow accumulation is equal to zero. The hydrographic order of each river segment was calculated using the `stream order` tool of ESRI, with the Strahler option (Strahler, 1952). Statistical tools, such as `cell statistics`, `summary statistics`, were used in order to calculate the length of the segments and the frequency of the stream orders. The different iterations were combined to produce a cumulative probability surface. At each iteration the networks were added to each other in order to calculate in how many iterations a cell was part of the stream network. Each cell identify how many times a stream network passed trough the cell. The more times a stream network passed trough the cell, the higher the probability it would occur. The same was done with the ridge cells.

The watershed were derived following the method indicated in `www.ce.utexas.edu/prof/maidment/gishyd97/class/wshed/wshed.htm`. As first step the stream links, i.e. the sections of a stream channel connecting two successive junctions, a junction and the outlet, or a junction and the drainage divide, were derived using the `stream link` tool. The links were then used to calculate the maximum value of flow accumulation along the network (`zonalmax`). Then the cells which value was equal to the flow accumulation were selected as the cells above which the contributing areas, or catchments, are determined. These cells were used as input for the watershed calculations as pour point locations, together with flow direction values in the `watershed` tool. The tool outputs the total area flowing to a given outlet or pour point. An outlet is the point at which water flows out of an area and it is the lowest point along the boundary of the watershed. A watershed is defined by contiguous cells with the same ID. The borders of the watershed were identified as the cells where the range of values, calculated in a 3x3 window, was greater than 1. The border obtained was 2 pixels wide, 1 pixel for each neighbouring watersheds. It allowed to keep the ID of each watershed linked with its border. The different iterations were combined to produce a cumulative probability surface. At each iteration the borders of the watersheds were added to each other in order to calculate in how many iterations a cell was part of the border of a watershed. Further statistics were calculated in order to summarise number and area of the watershed in the various simulations.

In order to get a better visualisation, the cumulative probability maps or river networks and watersheds borders were graphically unified in a composite band image using the `composite bands`:

- red = cumulative probability data for river networks
- green = cumulative probability data for watershed borders
- blue = void image

Therefore yellow pixels indicate high values for both input data, and black pixels represent low values for both data.

The `basin` tool was used to compute the drainage basin of the datasets considered. The tool delineates drainage basins by identifying ridge lines. It analyses the flow direction to find all sets of connected cells that belong to the same drainage basin. The drainage basins are created by locating the pour points at the edges of the image, where water would pour out of the grid, then identifying the contributing area above each pour point. The different iterations were combined to produce a cumulative probability surface. At each iteration the borders of the basins were added to each other in order to calculate in how many iterations a cell was part of the border of a basin.

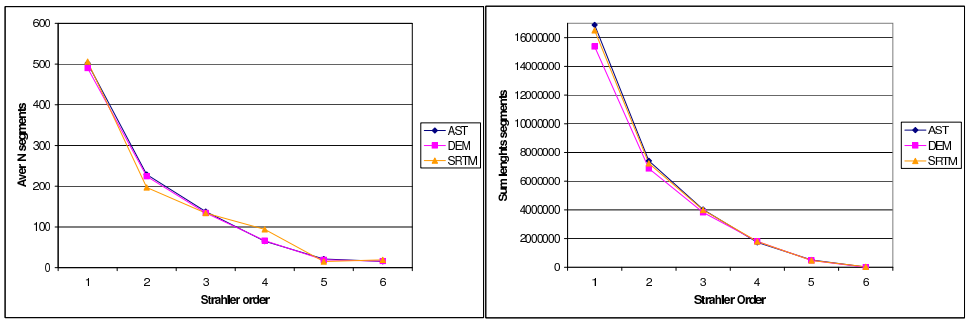

(a) Average number (b) Length

Figure 3.7: Statistics about Strahler order segments.

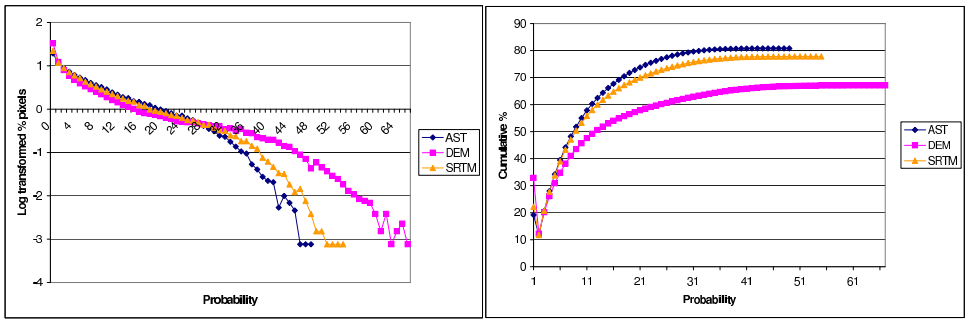

(a) (b)

Figure 3.8: Probability distribution of stream network.

3.2.2 Stream Networks

The number of segments for each Strahler order was calculated in each iteration. The average over the 100 repetitions is represented in figure 3.7a. AST and DEM datasets follow a similar pattern, with very small differences. SRTM dataset, which has the lowest original resolution, shows a steeper reduction for order two, with a slightly higher value for order four. SRTM and AST show a slightly steeper curve when plotting the sum of the lengths of the segments for each order (figure 3.7b). However, in both cases, it is difficult to identify significant differences among the datasets.

The pixel distribution was derived from the raster indicating the cumulative probability of stream network. The distribution of the probability indicates which % of pixels belong to a certain values of probability. It is shown in 3.8a with a log10 transformation of the data in order to enlarge the scale for better differentiating among datasets. The cumulative probability curve is shown in figure 3.8b. The DEM dataset appears to be the one reaching the highest maximum probability value (72%) and also has the highest number of cells with value 0, never part of a network. AST reaches the lowest maximum probability value (49, 55 for SRTM), but with an higher number of cells in the most probable side. The distribution of SRTM is intermediate within the other two, but appears to be closer to the AST one.

3.2.3 Watershed

The number of the watersheds was calculated for each iteration and then summarised and averaged for all the 100 iterations. The number vary from the minimum of 696 watersheds of the DEM dataset to the maximum of 811 of the AST dataset (figure 3.9). The pixel distribution was derived from the raster indicating the cumulative probability of the watershed borders. The probability distribution is shown in figure 3.8a with a log10 transformation of the data in order to enlarge the scale for better differentiating among datasets. The cumulative probability is reported in figure 3.10b from which it is possible to recognise the typical shape of normal distributed values. AST and SRTM have very similar

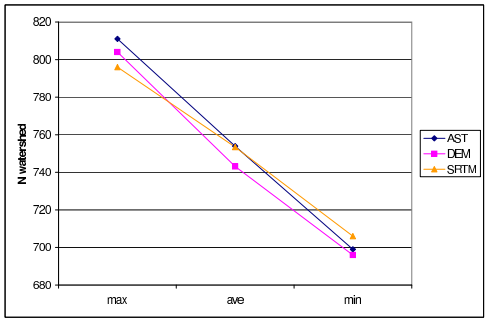

Figure 3.9: Number of watershed.

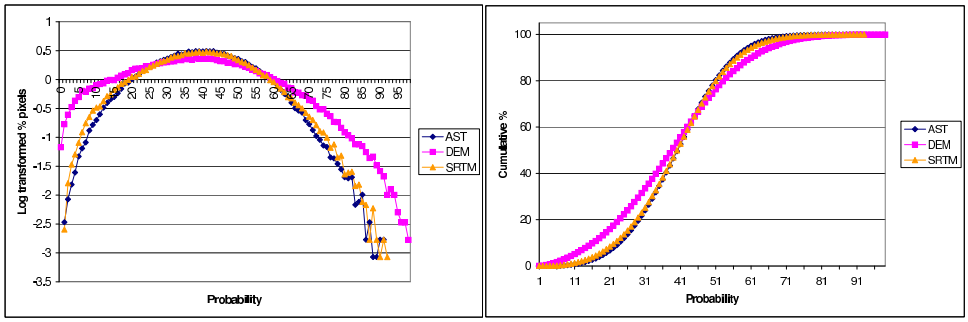

(a) (b)

Figure 3.10: Probability distribution of watershed borders.

distributions, while DEM has a slight different curve, reaching higher probability values (close to 100), but with very few pixels.

3.2.4 Spatial distribution

The maps in figure 3.11 for AST, figure 3.12 for DEM and figure 3.13 for SRTM represent the spatial dimension of the previous illustrated distributions. The river network is clearly delineated for all three datasets. The distribution of the watershed borders is more smooth and it is difficult to clearly identify all the watersheds. This is further indicated by the distribution of the ridge cells that is very scattered. In this case it is possible to identify part of the river network where there is the lower probabilities to find a ridge cell. A more clear representation of the spatial distribution of the watersheds is given in the combined RGB maps, where the yellow areas indicate the junctions pixels, where streams and watersheds join. The maps in figure 3.14 represent the spatial dimension of the cumulative probability of derived basins plotted over the respective cumulative probability map for stream networks.

The cumulative probability map for stream derived from DEM dataset appears more defined. The main network is narrower and the uncertainty in the lower order segments is less marked. In the DEM cumulative probability map for watershed borders the main divides are more evident, as well as some catchments in the central area. In the distribution of the ridge cells the river network is better delineated

Table 3.4: Statistics about the probability distribution maps of considered datasets.

	% cell 0 value			Mean probability value		
	AST	DEM	SRTM	AST	DEM	SRTM
Stream network	0.19	0.33	0.22	24.52	33.59	27.52
Watershed divides net	0.00	0.01	0.00	46.07	49.51	46.50
Basin divides	0.63	0.69	0.64	48.02	49.57	44.50

and most branches can be identified. The borders of the basins are quite well delineated and narrower compared to the other datasets. The maps of AST and SRTM are quite similar. The stream network has a wider area on the main segments and the identification of segments of lower order has high uncertainty, as they are represented mostly as clouds of points. The map of cumulative probability for watershed borders is very smooth and only the main divide can be identified. The ridge cell distribution is very scattered, especially in case of AST dataset. The borders identified in the map of cumulative probability for basins are more pronounced, but wider then in case of DEM dataset and with some cloudy regions aside from the main basin.

In order to try to quantify the differences perceived in the spatial distribution, the percent of cells with value zero was computed (table 3.4). These cells are never part of the stream networks or of the watershed divides nets. An higher percent of cell with zero value could be considered as an indication of less spread spatial distribution. DEM dataset has a considerable higher value for the stream network and it is the only dataset that has some cells with zero value in the watershed divides map. As other indicator the mean of the probability value was computed for the cells part of a network at least once (table 3.4). DEM dataset has higher values also for this indicator, but the differences are less important. The values for the watershed divides net are rather similar for all three considered datasets.

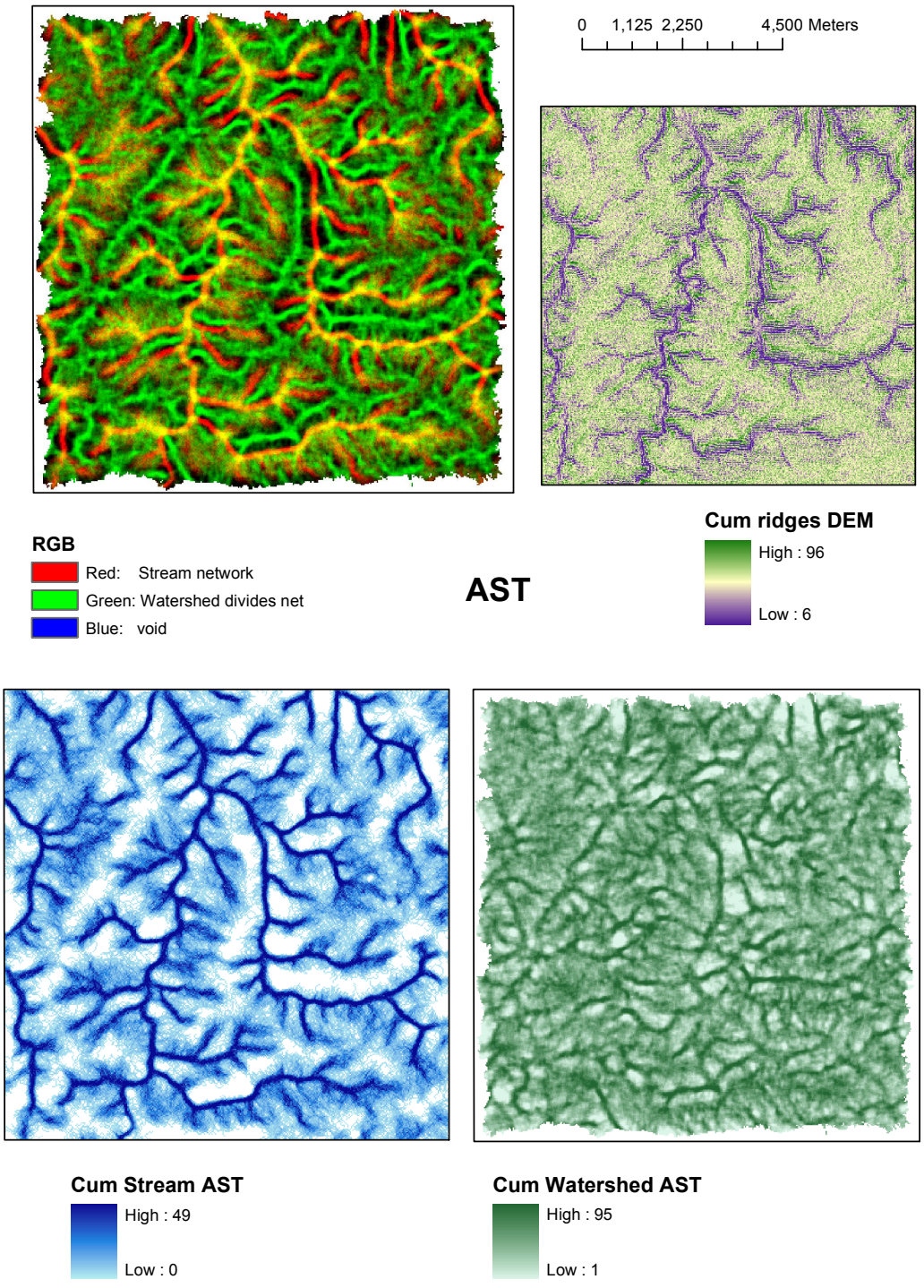

Figure 3.11: Cumulative probability distribution for AST dataset.

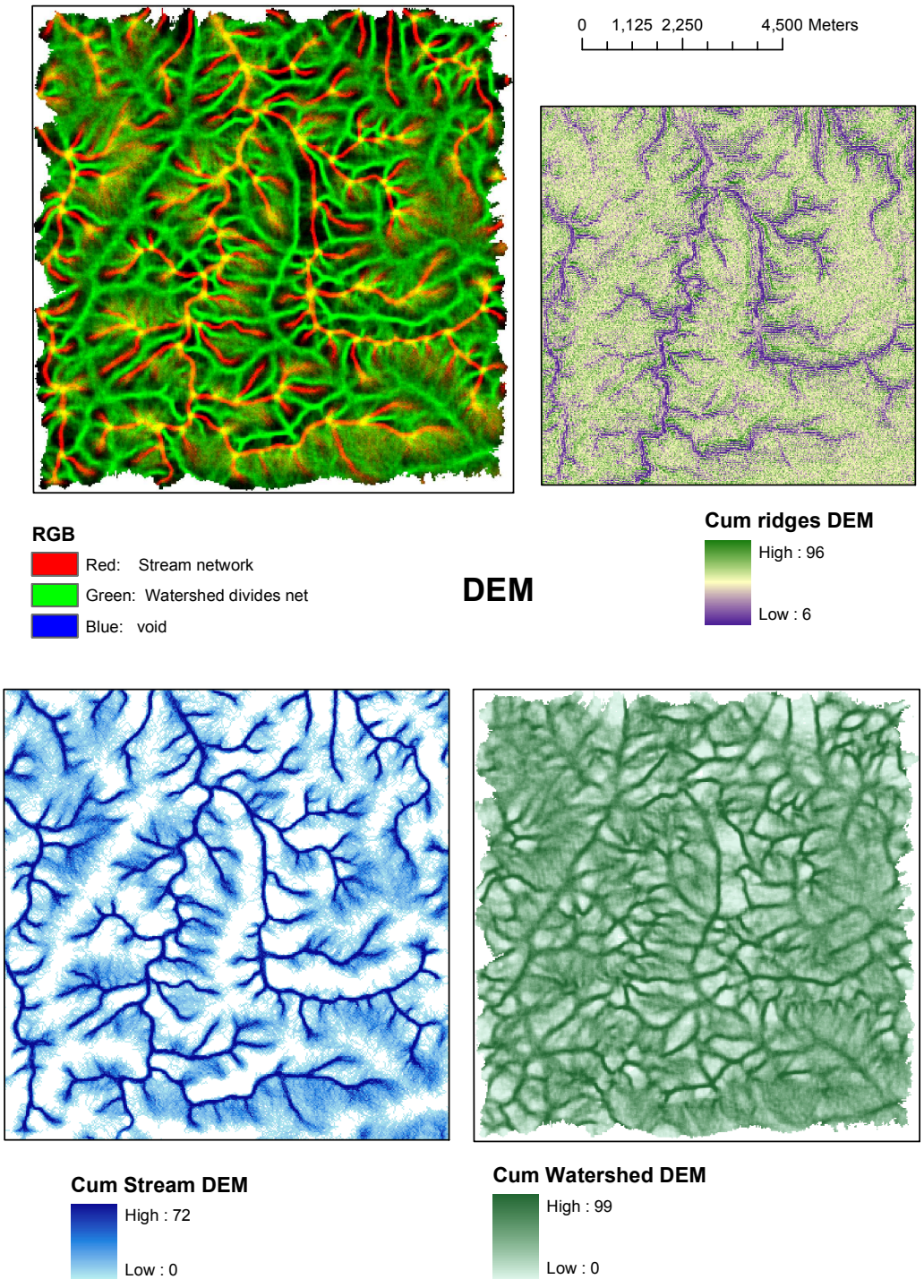

Figure 3.12: Cumulative probability distribution for DEM dataset.

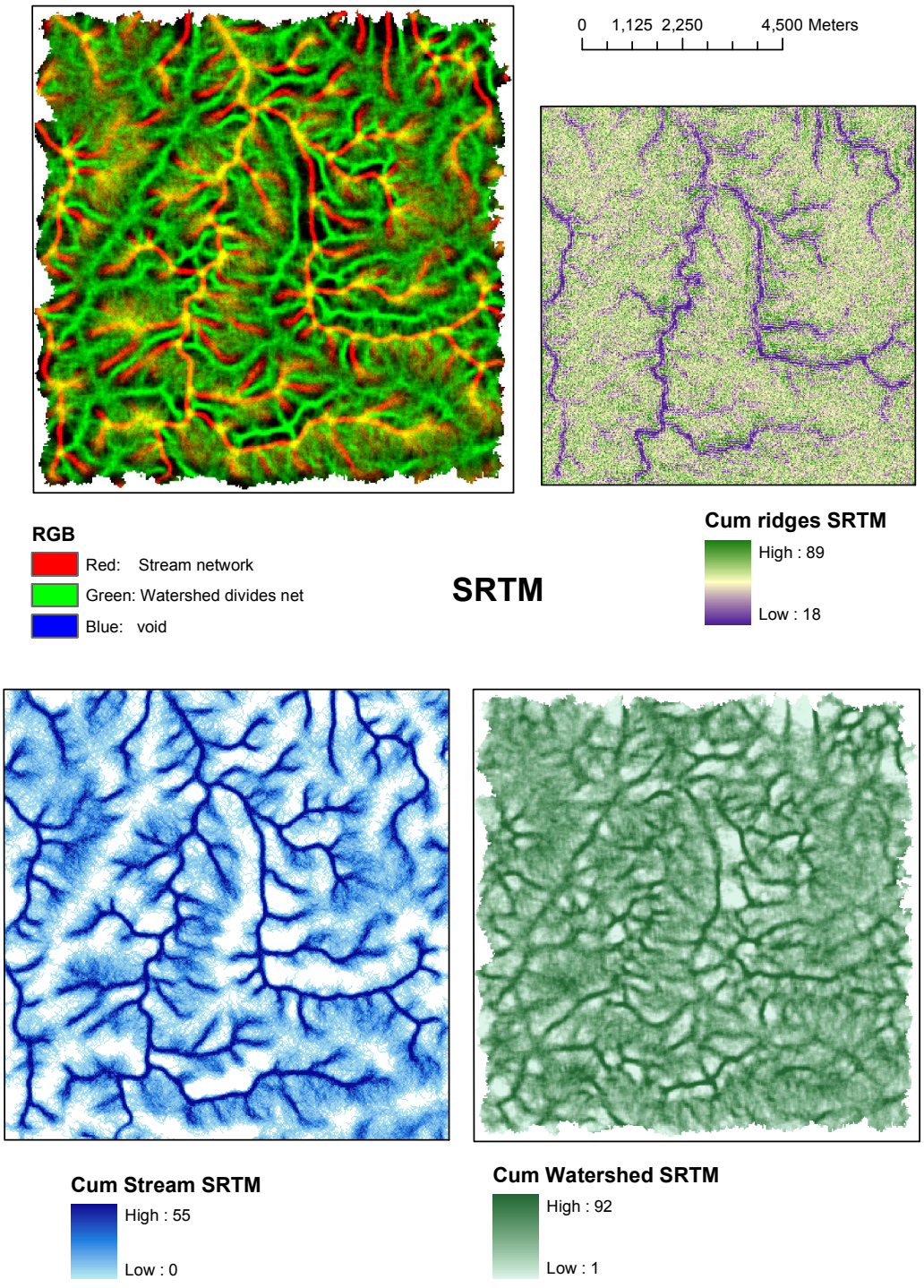

Figure 3.13: Cumulative probability distribution for SRTM dataset.

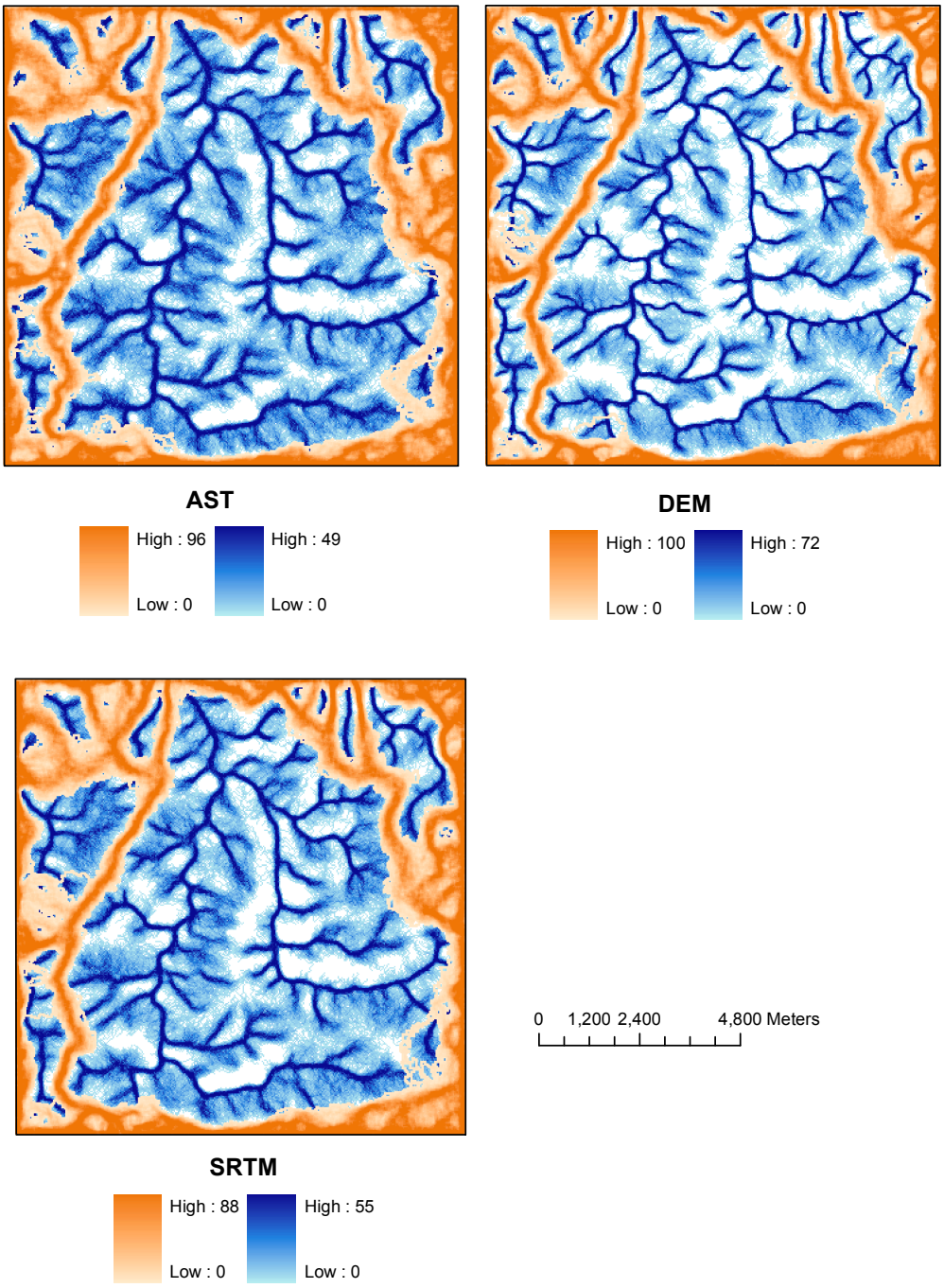

Figure 3.14: Cumulative probability distribution for derived basin, superimposed on the stream cumulative probability maps.

3.3 Strahler order

The variability of the Strahler order in a given cell was investigated, in order to better characterise the distribution of the Strahler order values for the different segments of the river networks among the 100 iterations. Several parameters were calculated and summarised for all the iterations. The Strahler order of the watersheds was calculated in order to analyse the behaviour of cumulative divides positioning in different uncertainty conditions.

3.3.1 Methods proposed

For all the calculations related to Strahler orders, the `NO DATA` values were set as 0 in order to avoid interferences in following computations. Several options of the `cell statistic` tool of ESRI were used:
- **variety** defined as how many different values has a cell;
- **maximum/minimum** values. In order to calculate the minimum value for all iterations a further transformation of the data was needed. Each cell was at least once not part of a network and then identified with value 0. Thus the minimum among the 100 iterations was always for all cells zero. To avoid this the zero values were set as 10, since this Strahler order value is never reached;
- **range**.

The cumulative distribution probability for each order was computed. At each iteration the segments of the river network belonging to the same order were added to each other in order to calculate in how many iterations a cell was assigned the considered Strahler order. The process was repeated for all the existing orders, six in this case. The the maximum value of the six cumulative probability distributions/maps was calculated (`cum-max` in the following text). Finally the maximum most probable value of Strahler order was derived using a `conditional` map algebra statement: if the value of the `cum-max` grid for a given pixel is equal to the value for cumulative probability of order one then value 1 is assigned to that pixel, if the value of the `cum-max` grid for a given pixel is equal to the value for cumulative probability of order two then value 2 is assigned to that pixel and so on. The resulting map was defined as the *maximum most probable Strahler order*.

A similar approach was used also for the derivation of watersheds and the calculation of watersheds orders. The watershed were derived from stream network presenting only segments with increasing orders:
1) segments with Strahler order higher then 1 (orders 2 to 6);
2) segments with Strahler order higher then 2 (orders 3 to 6);
3) segments with Strahler order higher then 3 (orders 4 to 6);
4) segments with Strahler order higher then 4 (orders 5 and 6 , when existing).

The borders of the watersheds were then derived, applying the method described in section 3.2.1 on page 28. The cumulative distribution probability for the borders of the watersheds in the case listed above was computed and labelled as following:
1) **prob0** → all orders are considered;
2) **prob1** → orders 2 to 6 are considered;
3) **prob2** → orders 3 to 6 are considered;
4) **prob3** → orders 4 to 6 are considered;
5) **prob4** → orders 5 and 6 are considered.

3.3.2 Stream Networks

Figure 3.15a represents the summary for all iteration of the variety of the Strahler order values for each cell. Variety one represent the pixels that have the same value for all the iterations. From the spatial distribution (figure 3.18 for AST, figure 3.19 for DEM and figure 3.20 for SRTM) it is possible to see that these pixels have Strahler order value zero, thus are never part of the stream network. The highest number of pixels has variety two, i.e. when part of a river network, a cell have always the same Strahler order. From the spatial distribution it is possible to see that they have mostly a low Strahler order value, generally one. The curve decreases then rapidly and only about one fifth of the pixels has variety four. Very few pixels have variety higher then five. AST and SRTM have similar behaviour, while DEM has a higher number of pixels with variety one and lower amounts of pixels with variety three and four. The distribution of the range (figure 3.15b) shows a high amount of pixels for values zero, where the

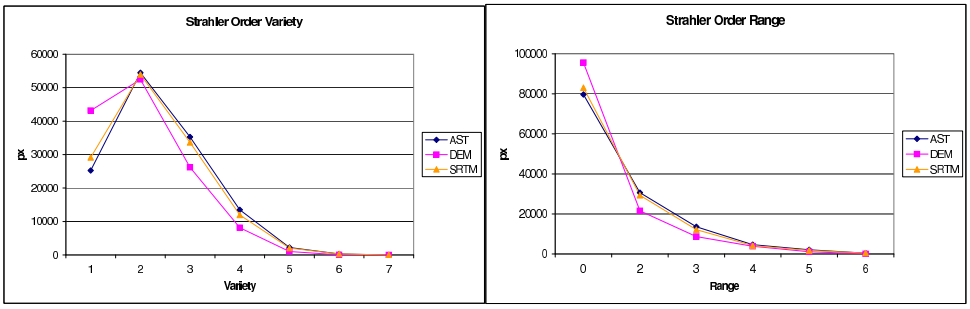

(a) Variety (b) Range

Figure 3.15: Strahler order variety and range.

maximum and minimum were coincident. The curves decrease then rapidly, indicating that there were few pixels with large differences of Strahler orders among the iterations.

The pixel distributions were derived form the cumulative probability rasters of each Strahler order, indicating the % of a certain probability. In figure 3.16 the different orders are plotted together for each dataset. In case of AST the highest probability are reached for Strahler order three and very few values are existing for Strahler order six. The DEM dataset is reaching higher probabilities values for all Strahler order. The highest probability is reached for Strahler order two. Strahler order six is represented with very few pixels, corresponding to one iteration. The SRTM reaches the highest probability for Strahler order four, with the highest amount of pixels representing Strahler order six. Figure 3.17 compare directly the three datasets for the different orders. The DEM reaches the highest values of probabilities for all the Strahler orders expect the order six, generally with a more flat curve. AST and SRTM have curves with very similar trends and AST, generally, reaches lower values.

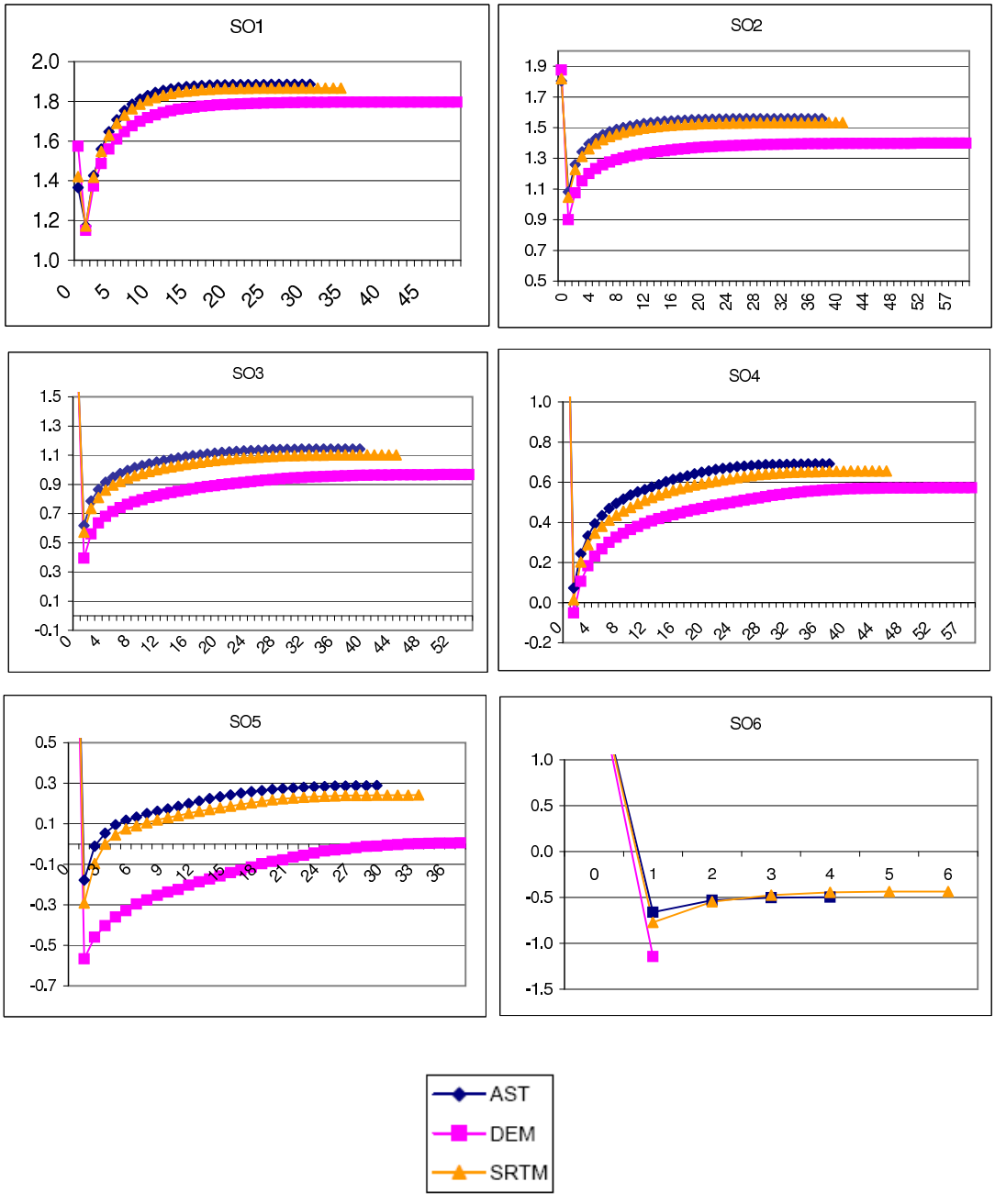

Figure 3.16: Cumulative probability distributions for Strahler orders.

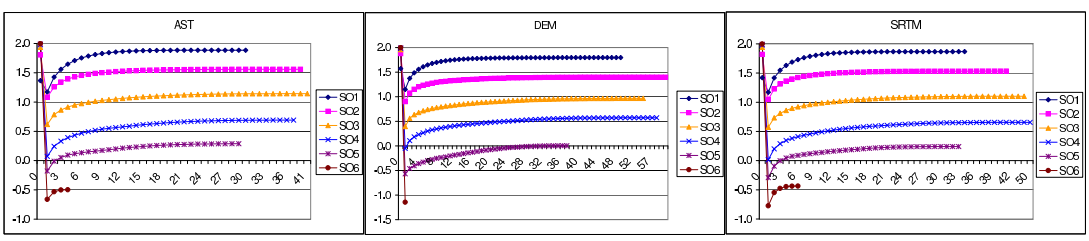

(a) AST (b) DEM (c) SRTM

Figure 3.17: Cumulative probability distributions for Strahler orders and datasets.

Table 3.5: Statistics about the probability distribution maps of considered datasets for the various Strahler orders (SO).

	% cell 0 value			Mean probability value		
	AST	DEM	SRTM	AST	DEM	SRTM
SO1	0.232	0.374	0.264	15.53	25.14	17.53
SO2	0.638	0.750	0.659	19.74	30.08	21.32
SO3	0.861	0.907	0.873	20.05	27.56	22.50
SO4	0.951	0.963	0.955	19.03	29.14	23.24
SO5	0.981	0.990	0.983	15.00	20.15	17.03
SO6	0.997	0.999	0.996	1.80	1.00	3.50

Spatial distribution

The map showing the maximum values of Strahler order for all iterations (figure 3.18 for AST, figure 3.19 for DEM and figure 3.20 for SRTM) is generally very cloudy for Strahler orders one and two, becoming more defined for orders higher than three. Order four is evident in the two main branches of the stream network while order five and six are mainly visible in the last part of the network toward the main outlet. The main branches are characterised by an inner core of higher order surrounded by a narrower line of lower order. The range map show a similar pattern. The maps presenting the minimum values of Strahler order are characterised by large areas of value one and the stream network can be localised with difficulties, being not full connected. Generally, the DEM distribution is more defined and narrower, with less variability in the main branches.

The variety distribution shows a higher variability in the main branches and in some cloudy areas around segments of order one. The distribution of DEM dataset is more clear with less area with high variability. It seems that DEM has generally at least a variety order less then AST and SRTM. Figure 3.21 for AST, figure 3.22 for DEM and figure 3.23 for SRTM represent the cumulative probability map for each considered Strahler order and the map with the maximum most probable Strahler order for each pixel. AST and SRTM have very similar patterns, with AST a little bit more cloudy for order one, with wider network for orders four and five. SRTM has a more defined network for order six, reached in six iterations instead of four for AST. DEM has different distributions, visually less scattered for order one. In the map representing Strahler order two, the segments are already mostly defined with very limited cloudy areas. Higher orders are more clearly defined, with narrower uncertainty bands. Strahler order six is represented with a line, as it was reached in only one iteration.

The maps of the maximum most probable Strahler order are very similar for AST and SRTM. AST is slight more scattered in lower Strahler orders. The DEM dataset present larger areas of zero value, that were never part of a network and a more defined network with sharper transitions among orders. Cloudy areas for orders higher then two are rather rare and also Strahler order two is well defined.

The percent of cells with value 0 and the mean of probability values for cells that were part of the network broken down by Strahler order are shown in table 3.5. The numerical values underline what was visible in the maps. In each order DEM reached higher values. In general the values for Strahler order one are rather low, indicating high variability and uncertainty in the positioning of the segments.

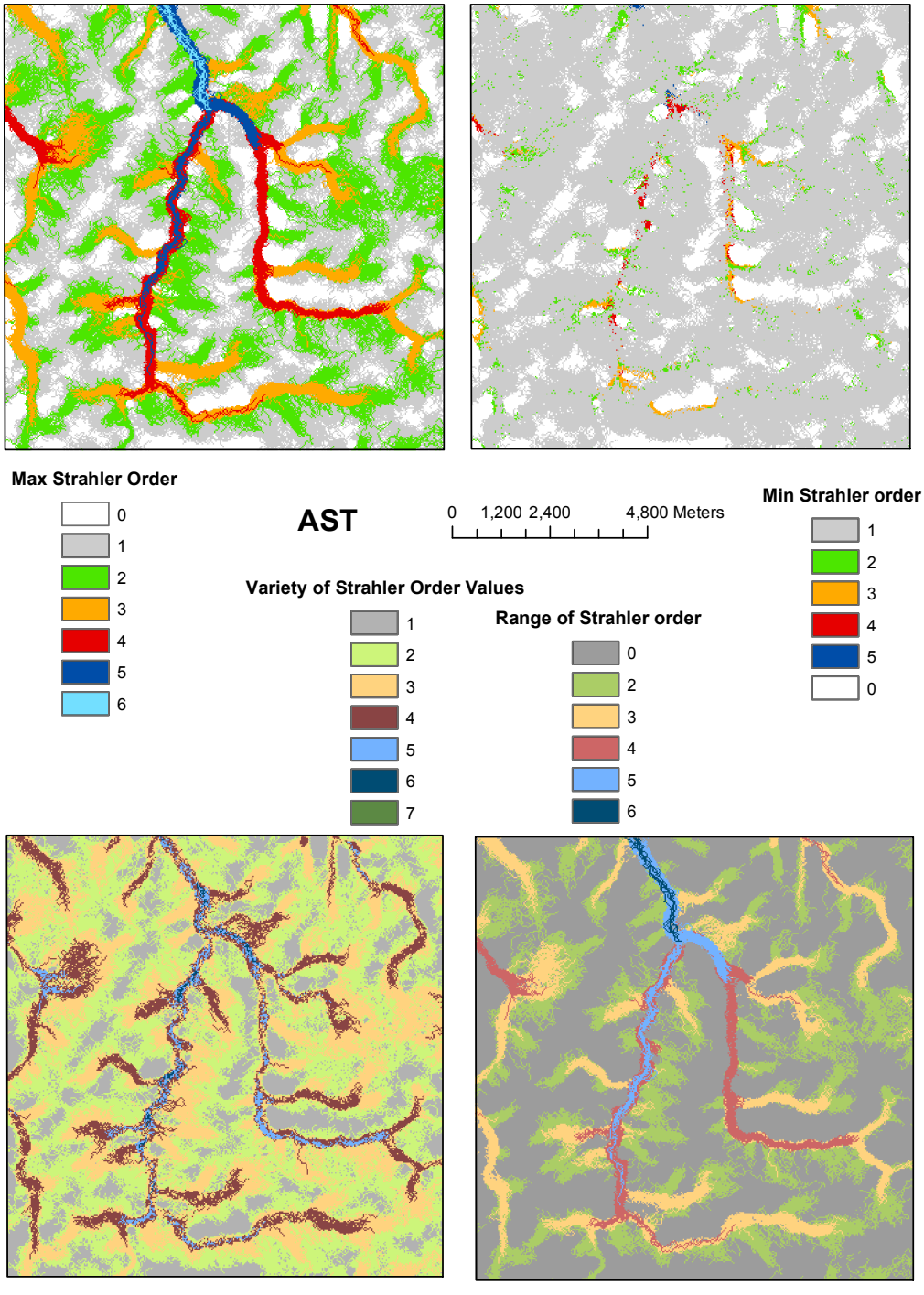

Figure 3.18: AST: Distribution of some Strahler orders summary statistics.

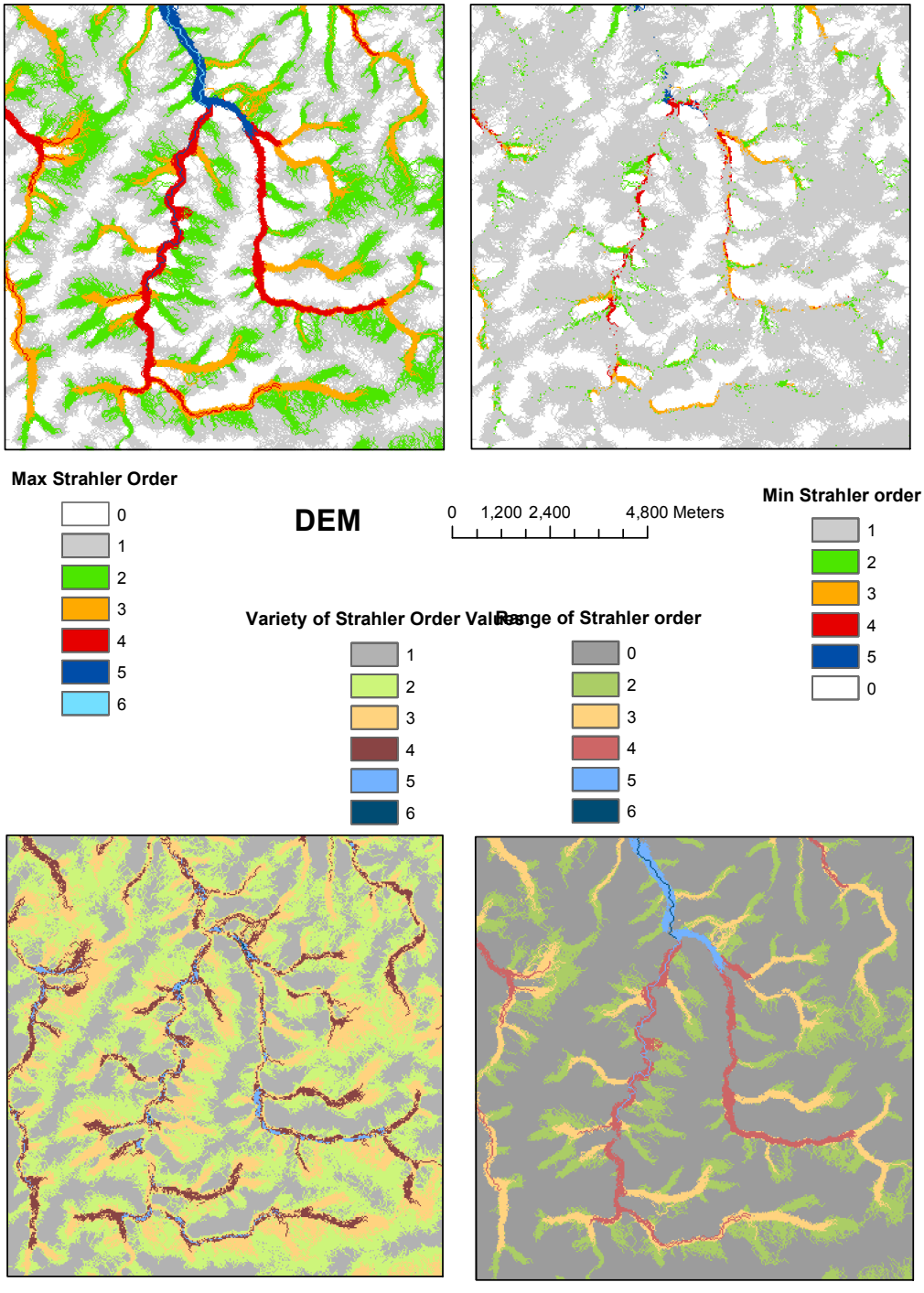

Figure 3.19: DEM: Distribution of some Strahler orders summary statistics.

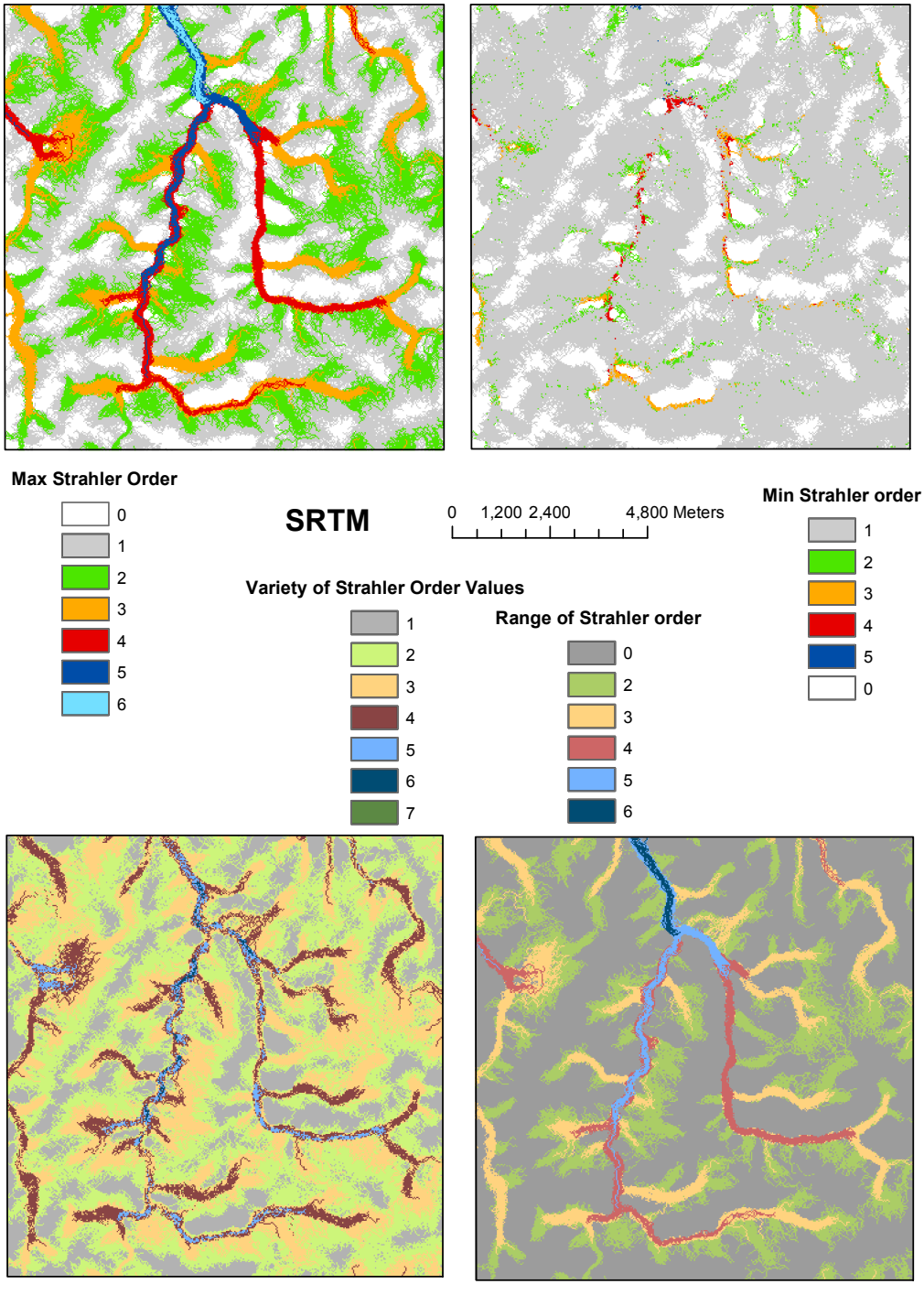

Figure 3.20: SRTM: Distribution of some Strahler orders summary statistics.

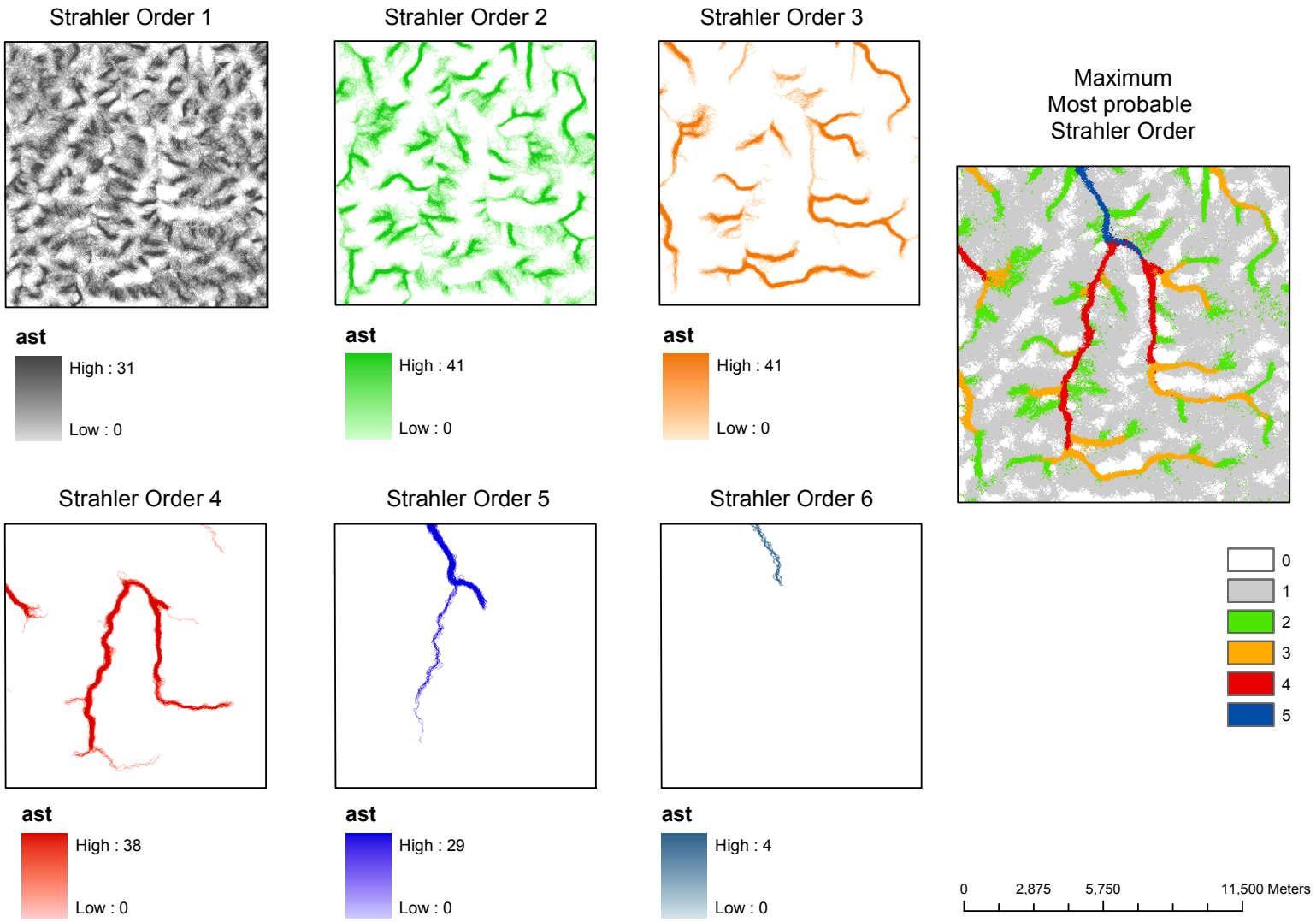

Figure 3.21: AST: Cumulative distribution probability for the Strahler orders and maximum most probable value.

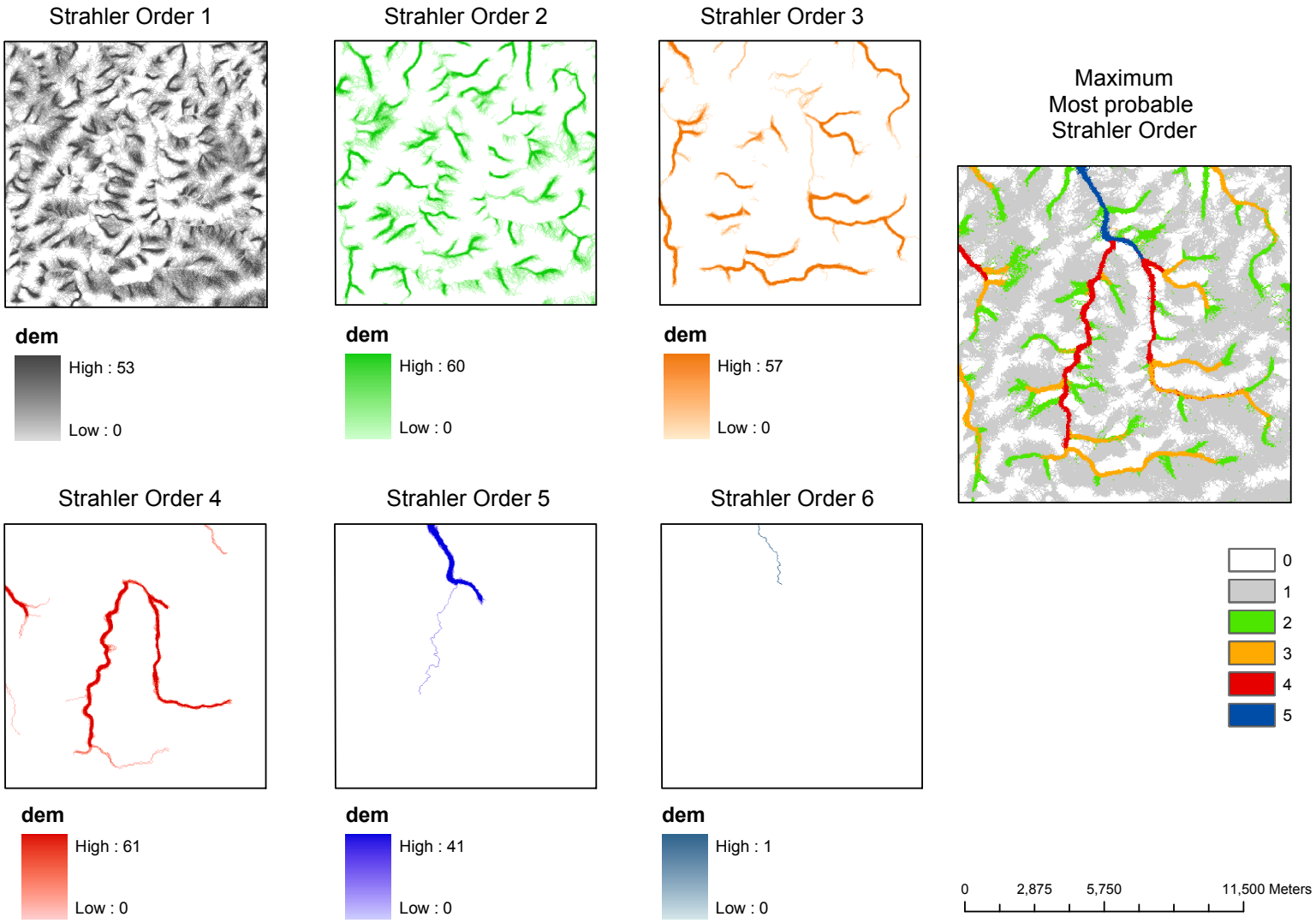

Figure 3.22: DEM: Cumulative distribution probability for the Strahler orders and maximum most probable value.

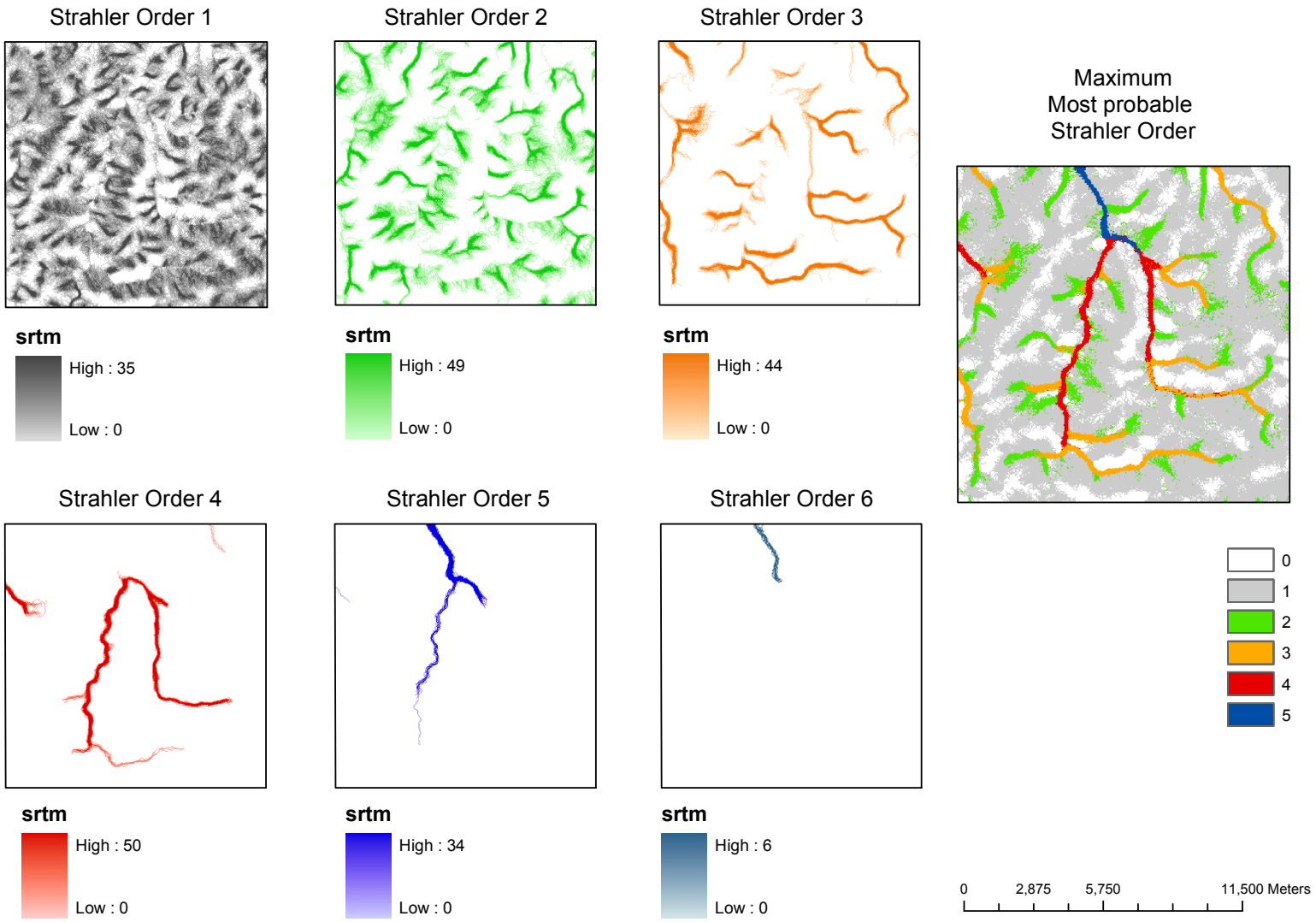

Figure 3.23: SRTM: Cumulative distribution probability for the Strahler orders and maximum most probable value.

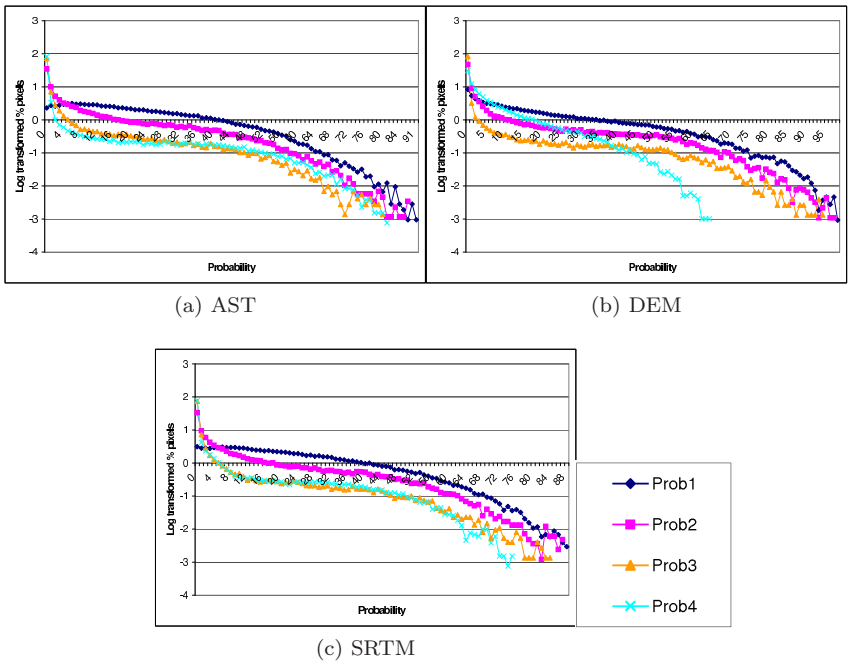

(a) AST (b) DEM

(c) SRTM

Figure 3.24: Probability distribution of watershed divides for different Strahler orders.

3.3.3 Watershed

Figure 3.24 represents the probability distribution of the cumulative probability map for watershed divides derived from stream network with increasing Strahler order. The curve `prob1` is derived from a network where segments of order one were not considered, curve `prob2` from a network where segments of orders one and two were not considered and so on. The curve of `prob0` for watersheds divides when all the orders are considered is described in figure 3.10 on page 30.

The four curves have similar trends and show comparable behaviours among the considered datasets. The shapes are rather different from the curve where all Strahler orders were considered. Curve `prob1` has a flatter shape, in a kind of transition from curve of `prob0` (figure 3.10). From curve `prob2` and on the shape is clearly different and more similar to what was found for the stream network derivation (figure 3.8). The cumulative distribution of the four curves (figure 3.25) does not follow the normal distribution shape as in case of figure 3.10, when all orders were considered.

The considered datasets show a similar behaviour, with AST and SRTM almost overlapping in most of the curves. DEM presents a clearly different trend in case of the curve `prob4`, when only orders 5 and 6 are used for computations of watersheds divides. This is also highlighted from the distribution of the cumulative probabilities (figure 3.25).

Spatial distribution

Figure 3.26 for AST, figure 3.27 for DEM and figure 3.28 for SRTM datasets represent the cumulative probability maps calculated for watershed divides from stream segments of increasing Strahler order:
- **prob0** grey map;
- **prob1** green map;
- **prob2** orange map;
- **prob3** red map;
- **prob4** blue map.

In the `prob0` map, where all Strahler orders were considered, the divides are overlapping and only some sections with higher probabilities are more easily identifiable. When increasing the Strahler order considered and thus decreasing the number of river segments used in the computations, the divides became more clear identifiable. The size of watershed increase for increasing number of Strahler orders.

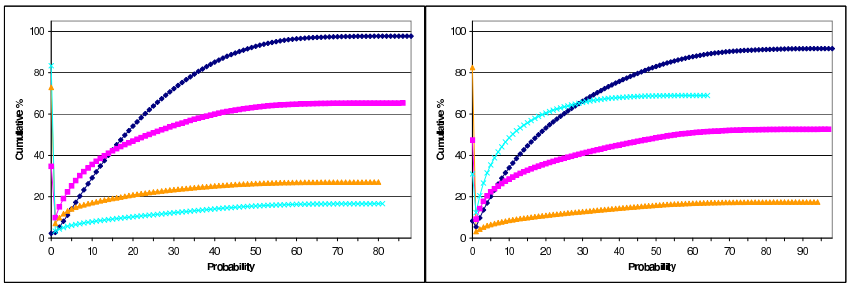

(a) AST (b) DEM

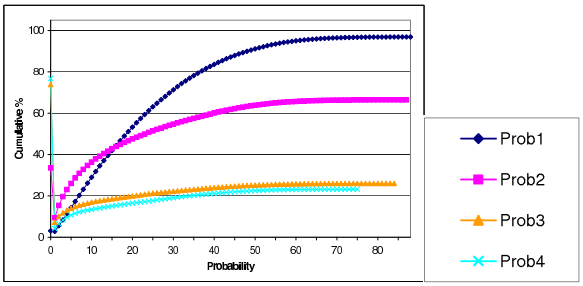

(c) SRTM

Figure 3.25: Cumulative probability distribution of watershed divides for different Strahler orders.

The map of `prob2` (orders 3 to 6) is sketching a more defined divides net. `Prob3` and `prob4` maps show few watershed and when considering only orders 5 and 6 the map is rather similar to the one for basin derivation (figure 3.14 on page 35). This can be linked with the distribution of stream network for different Strahler orders (figure 3.21 on page 43), where it was also highlighted that segments of orders one or two are very scattered in space among the different iterations, and there is not a clear indication on the most probable position in the space.

The differences among the three considered datasets show more defined maps for DEM and rather similar distributions for AST and SRTM.

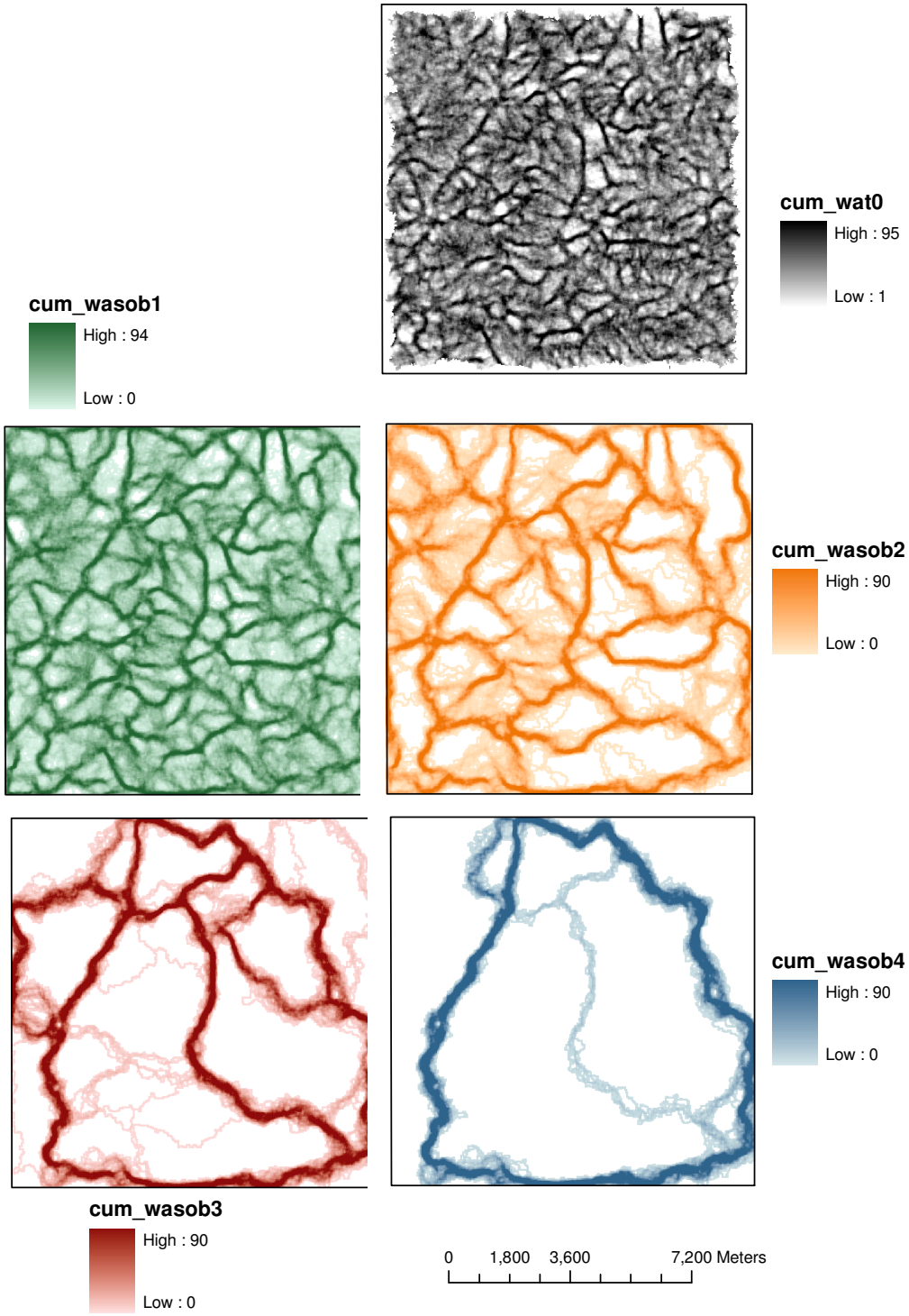

Figure 3.26: AST: Cumulative probability maps of watershed divides for different Strahler orders.

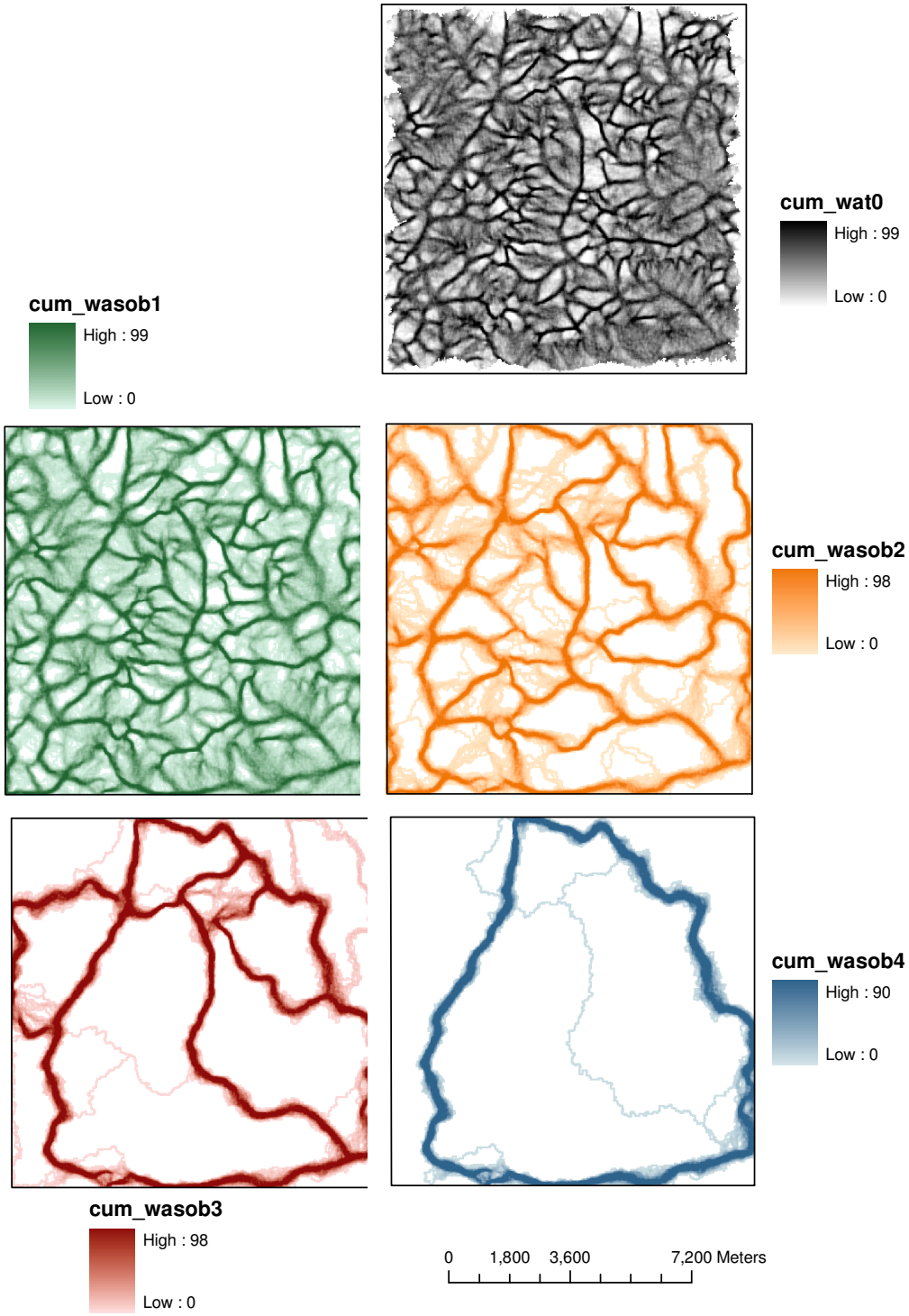

Figure 3.27: DEM: Cumulative probability maps of watershed divides for different Strahler orders.

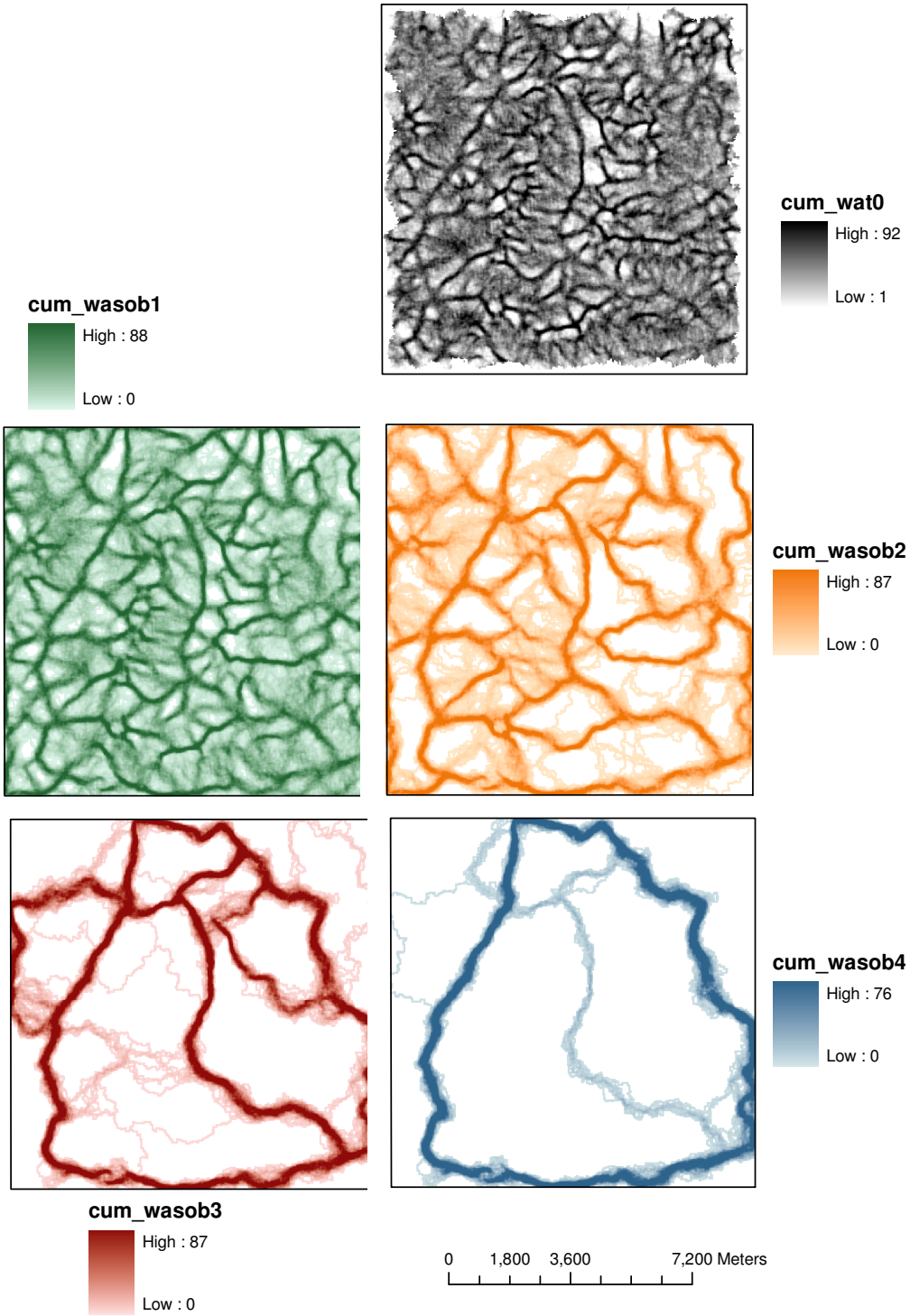

Figure 3.28: SRTM: Cumulative probability maps of watershed divides for different Strahler orders.

3.4 Most probable

The analysis of the cumulative probability maps and distributions provide information about the confidence level of a cell, i.e. on which is the probability that a certain cell is part of a stream network or of a divide among watersheds. However it does not directly indicates which is the *most probable* river network or divide net. *Most probable* is defined as the network that maximise the probability. The most probable network should therefore pass trough cells with high probability values.

3.4.1 Method proposed

In order to identify the most probable stream network or watershed divides net several features were extracted from different datasets and the *overall probability* calculated. The overall probability was defined as the sum of the values derived from the cumulative probability map for all the cells of the considered river network or divides net. In order to get the most probable feature the overall probability has to be maximum. The datasets used were:

i) the original elevation dataset without any error modelling (`dtm` in the following text);
ii) average and median of the three datasets considered;
iii) the inverse of the cumulative probability map for stream networks;
iv) the stream network and divides net that had the highest overall probability among all which were extracted in the 100 iterations (`IterMax` in the following text);
v) the cumulative probability map for watershed divides.

The average and the median datasets were calculated as, respectively, the average and the median of all the 100 simulated DTMs obtained with the various iterations. The inverse of the cumulative probability map was calculated as $100 - cellvalue$ on a cell by cell basis. All datasets were threaded with pit filling algorithms in order to generate flowing surfaces. The methods used were the one implemented in the ESRI `fill` tool (ArcSink; Jenson and Domingue, 1988), a morphological pit filling algorithm (F1; Soille and Gratin, 1994), the carving (F2; Soille et al., 2003) and the optimal hybrid carving (F3; Soille, 2004b). The stream networks and divides nets were then extracted. The overall probability was calculated attributing to each cell the value of the cumulative probability map of the corresponding cell and summing up all the values.

In case of watersheds the cumulative probability maps were different according to which Strahler orders were considered in the computations:

prob0 → all orders;
prob1 → orders 2 to 6;
prob2 → orders 3 to 6;
prob3 → orders 4 to 6;
prob4 → orders 5 and 6.

3.4.2 Stream Networks

Figure 3.29 is representing the results of the overall probability for the considered datasets, figure 3.29a reports the absolute values, while the values normalised by the number of pixels are in figure 3.29c. Figure 3.29b represents the number of pixels for the derived stream network for the considered datasets. The itermax dataset has the highest number of pixels, while the inverse cumulative probability map for stream networks with sink filled with F2 or F3 method (carving or optimal hybrid carving) have the lowest. In order to avoid the influence of the number of pixels on the overall probability, the normalised values were considered.

It is possible to see a significant difference between the overall probability of features extracted from the DTMs-derived data, i.e. dtm, mean, median and itermax datasets, and feature extracted from the inverse probability maps. The network that maximised the overall probability among the different iterations has the lowest overall probability in this comparison. The network extracted from average and median datasets show slightly higher values. The results are shown only for the ArcSink filling method, as other filling methods did not change significantly the results. The network extracted form the inverse of the cumulative probability map for stream networks has the highest overall probability values, already when filled with the ArcSink method. The results are coincident to the values obtained using the F1 method. The use of the optimal hybrid carving algorithm (F3) increases further the values. The three

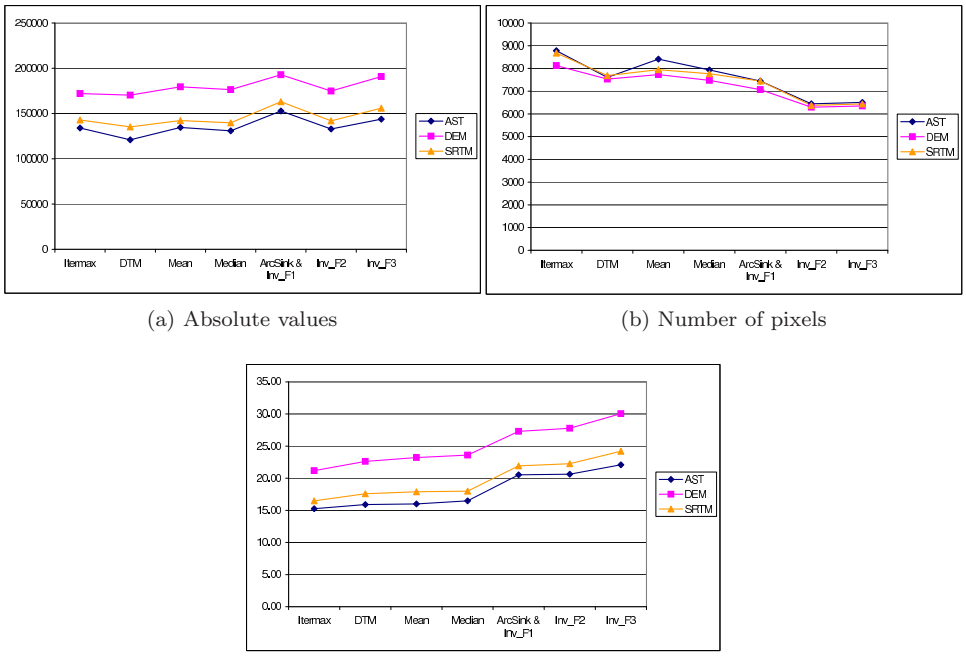

(a) Absolute values

(b) Number of pixels

(c) Normalised values

Figure 3.29: Overall probability of considered datasets for stream networks.

datasets have similar parallel trends. AST has the lowest overall probability for all the tested options. SRTM is quite close to AST, while DEM reaches the highest values.

In figure 3.30 the distribution probabilities along the network are presented for the tested options. In all three datasets it is possible to recognise some common indications. The networks extracted from average/median datasets and itermax have the peak of the curve in the left part of the diagram where the lower values for probabilities are. Most of the pixels are then in the low values area. The network extracted from the inverse probability map show a peak in the central part of the diagram, with more pixels in the central values of probabilities. The network extracted from the inverse probability map and filled with optimal hybrid carving shows a rather flatter curve, with a larger plateau including some of the higher probability values.

In figure 3.31 the networks extracted from the inverse probability map and filled with optimal hybrid carving are compared for all the three datasets. SRTM has a flatter curve, AST shows a higher peak, but less pixels in the area of higher values. DEM has a more homogeneous distributed curve, with the peak in the right region of the graph.

The cumulative probability curves are displayed in figure 3.32 and reveal similar general trends. Generally, extracted river networks with higher number of pixels (figure 3.29b) have higher cumulative probability distribution. The maximum probability for the iterations has always highest distribution, but very close to the curves of average and median derived datasets. The features extracted from the inverse probability map and simply filled have a distribution with a more pronounced S shape. Finally the features derived from the inverse probability map and filled with carving or optimal hybrid carving show a more flattened shape, reaching the plateau in a later stage.

Spatial distribution

In figure 3.34 for AST, figure 3.34 for DEM and figure 3.35 for SRTM, the stream network extracted from the different options tested are plotted on the cumulative probability distribution map. The features extracted from the original DTM datasets show numerous artefacts in the junctions, where multiple parallel lines are derived. The itermax network presents some artefacts and does not always follow the most probable path. The network derived from the average and median datasets are very similar and thus only the median network is presented. The features follow approximately the most probable values

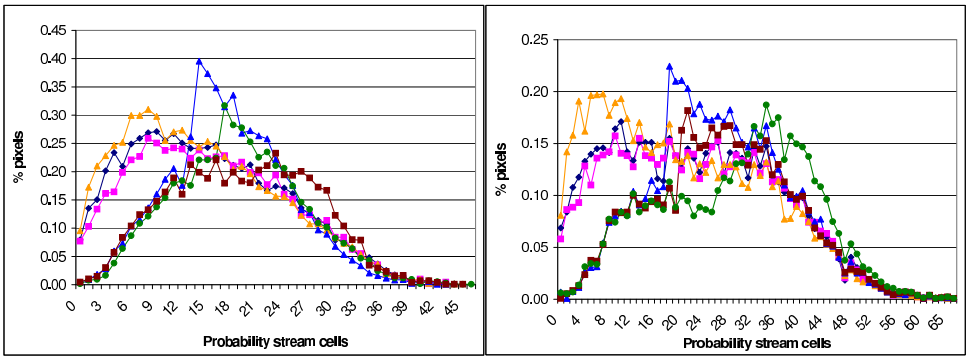

(a) AST

(b) DEM

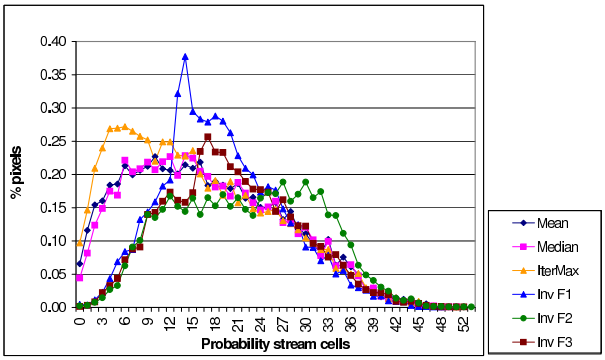

(c) SRTM

Figure 3.30: Distribution probabilities along the stream networks.

of the cumulative probability distribution map, falling often slightly aside, especially for the lower order segments.

The network extracted from the inverse of the cumulative probability maps show a different behaviour according to the filling algorithms used. In case of simple pit filling, the network presents often streams flowing parallels in the flatter regions. This is overcome using the carving or the optimal hybrid carving methods. In case of carving the networks present straight segments, while in case of optimal hybrid carving the networks seem to follow better the particularities of the terrain. In case of DEM datasets few segments are laying in areas with very low probability.

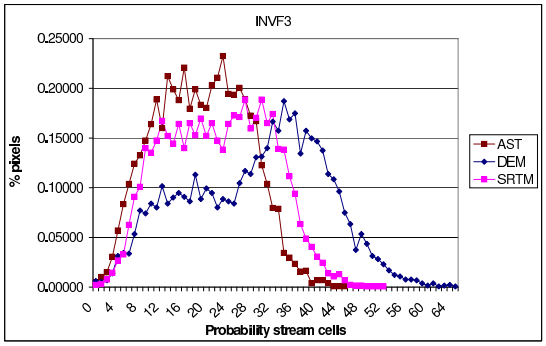

Figure 3.31: Distribution probabilities along the stream network of the considered datasets for the most probable case filled with optimal hybrid carving.

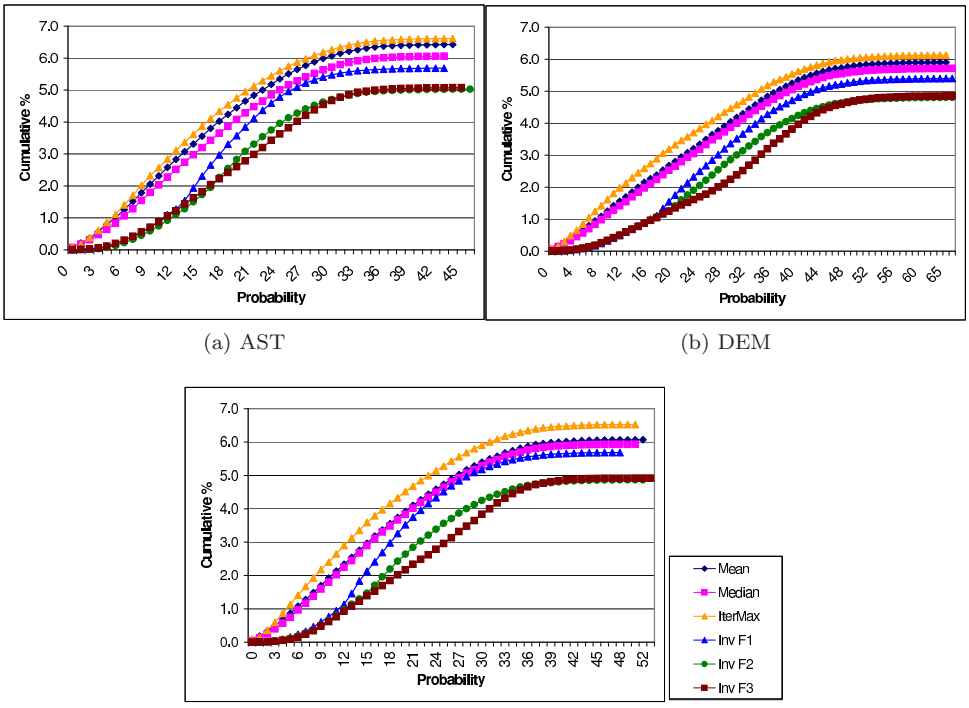

(a) AST

(b) DEM

(c) SRTM

Figure 3.32: Cumulative probability distributions of most probable river networks.

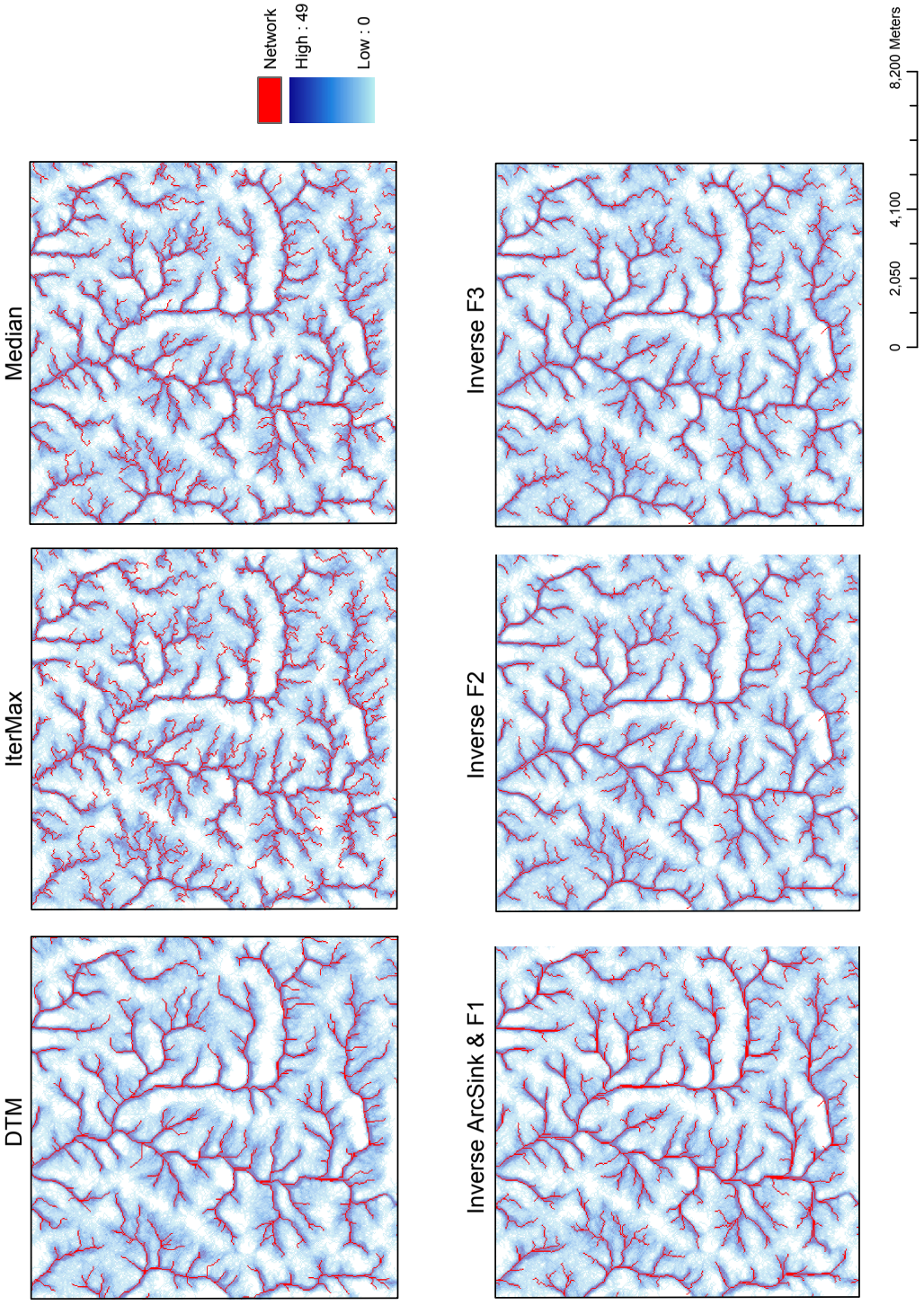

Figure 3.33: AST: Most probables stream networks.

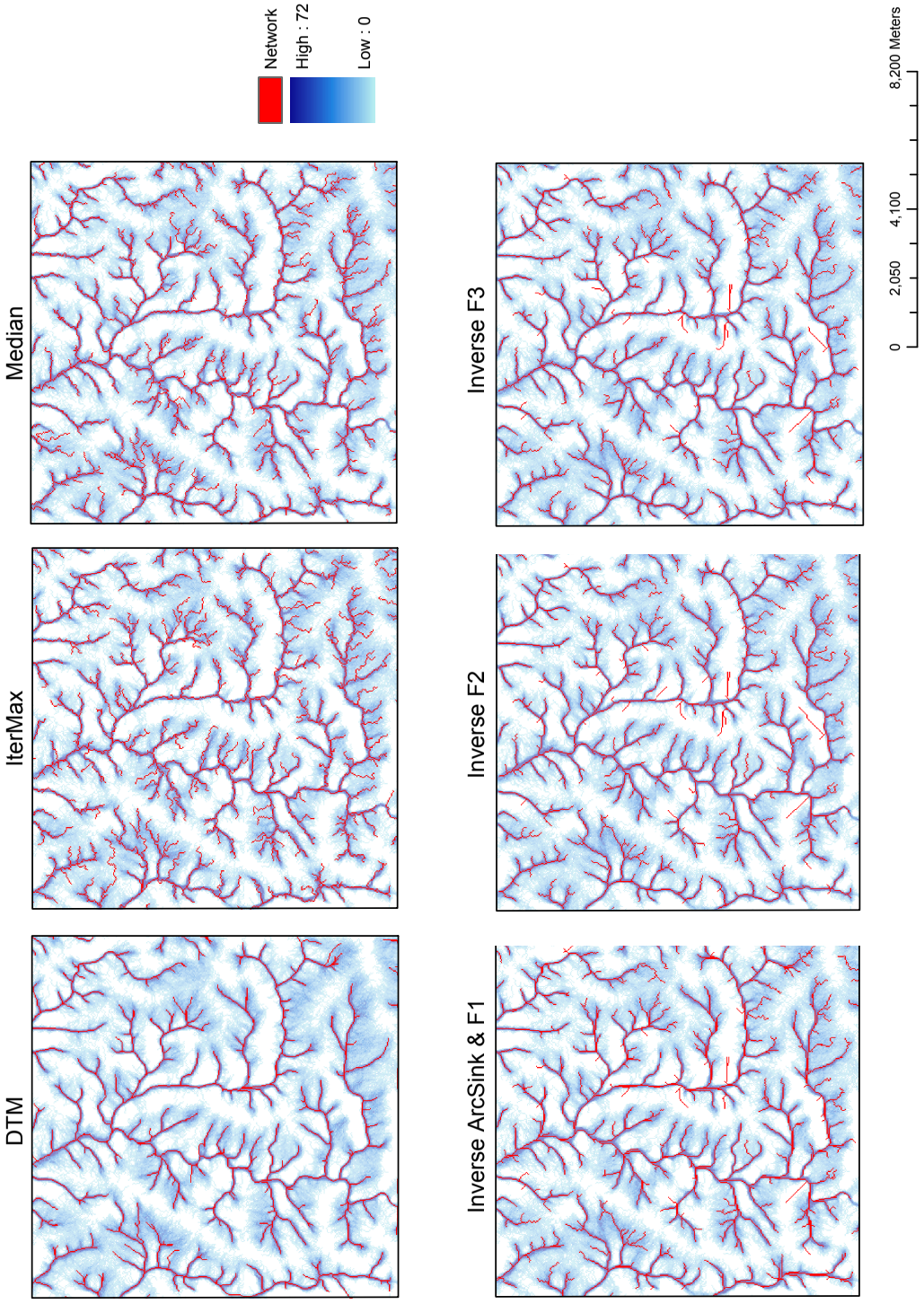

Figure 3.34: DEM: Most probables stream networks.

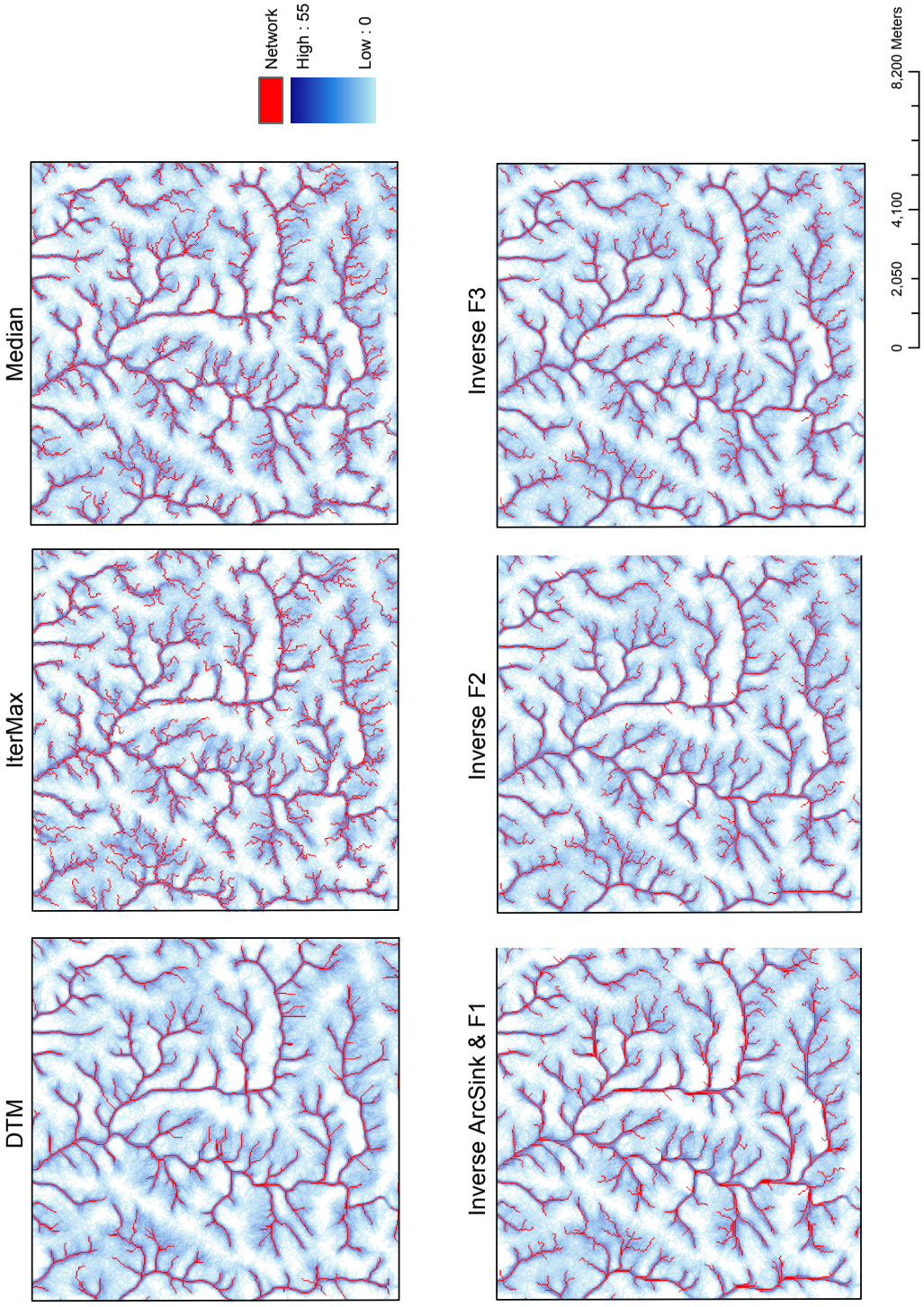

Figure 3.35: SRTM: Most probables stream networks.

Table 3.6: Overall probability values.

	AST	DEM	SRTM
CCM2	18.88	27.26	22.37
InvF3	22.10	30.06	24.21
Median	16.49	23.60	17.98
DTM	15.90	22.63	17.59
IterMax	15.26	21.18	16.47

Figure 3.36 on the next page show the most probable network compared with the network derived in the CCM2 (Catchment Characterisation and Modelling; Vogt et al., 2007). The CCM2 network has less numerous river segments because of the threshold calculated at continental scale. The two networks overlap in most cases. The obtained overall probability are higher for the derived most probable network (table 3.6), but the values for CCM2 are within a similar range, significantly higher then the values obtained for the network that obtained the highest overall probability and similar to the values obtained for the network derived from the mean dataset (table 3.6 and (3.29c). A few pixels translations can be found in the case of AST dataset and partly in case of SRTM resampled to a resolution of 30 m.

The network that reached the highest overall probability (InvF3) and the network reaching the lowest overall probability values (itermax) were plotted over a panchromatic image of the area in order to visually check the correspondence with the terrain (figure 3.37 on page 60; the area in the rectangle is enlarged for a more detailed visualisation). The features extracted from the inverse of the cumulative probability map for stream networks filled with optimal hybrid carving show a good spatial matching with terrain attributes. The segments are lying in valleys following the morphological contours of the region. The situation if rather different for the itermax features. Numerous low order segments are drawn in the upper regions of the watersheds. It is not possible to clearly indicate if these features are really existing on the terrain or if they are artefacts due to applied methods and available data. Furthermore these segments belong to the more scattered part of the cumulative probability map, where the probability values are lower.

(a) dem (b) DEM (c) SRTM

Figure 3.36: Most probable stream network and CCM2 (Vogt et al., 2007) network

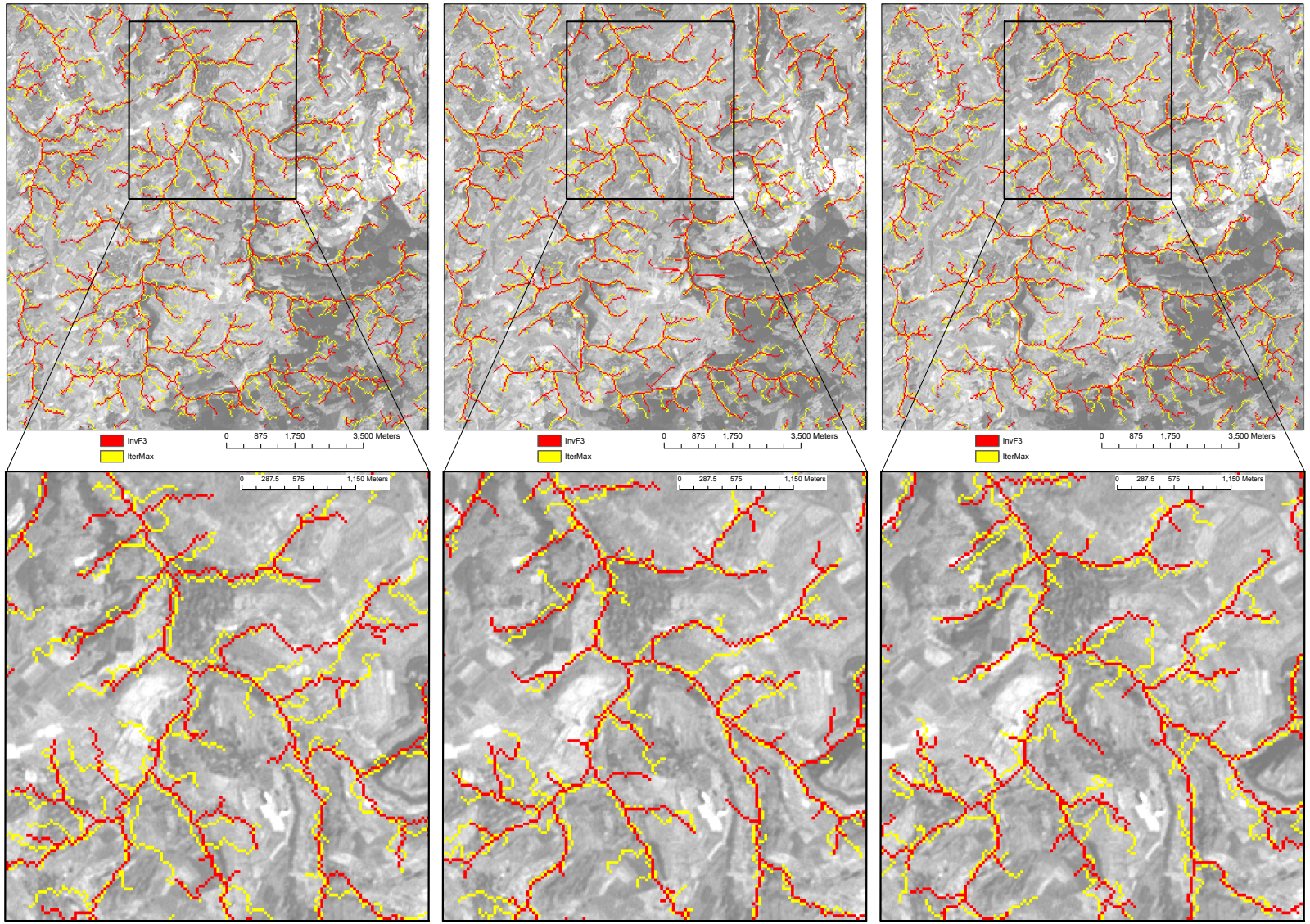

(a) dem (b) DEM (c) SRTM

Figure 3.37: Most probable stream network on panchromatic image

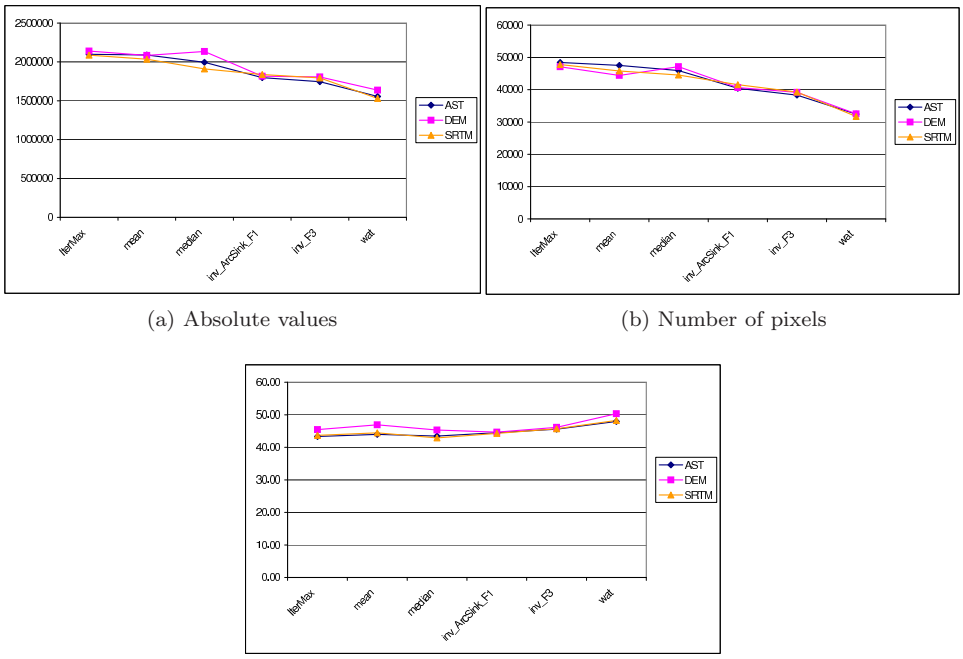

(a) Absolute values

(b) Number of pixels

(c) Normalised values

Figure 3.38: Overall probability of considered datasets for watershed divides.

3.4.3 Watershed

Figure 3.38 show the results for the computation of overall probabilities for the watershed divide nets. Figure 3.38a reports the absolute values, while figure 3.38c presents the values normalised by the number of pixels. Figure 3.38b represents the number of pixel of the derived watershed divides net for the considered datasets. The trend are not so well defined as in case of the stream network (figure 3.29b on page 52). The nets derived form the itermax, mean and median datasets show similar values with slight differences according to the DTMs considered. The nets derived from the inverse cumulative probability map for stream networks have lower values, while the nets derived from the cumulative probability map for watershed divides has the lowest number of pixels.

In case of watershed divides, on normalised values, it is not possible to indicate which is the most probable net. The divide nets derived from the average, the median and the inverse of the cumulative probability map for stream network have similar values. Using optimal hybrid carving method for sink filling does not improve significantly the results. The net derived from the cumulative probability map for watershed divides show higher overall probability. However, when plotting the net (figure 3.44 on page 68), the spatial distribution is not very consistent, as some divides do not follow the most probable path and often straight lines are appearing, cutting the watersheds. This behaviour could be explained by the fact that the cumulative probability map for watershed has a fairly different morphology then the DTM used or the cumulative probability map for stream network.

In order to reduce the uncertainty due to lower order segments the overall probability was calculated using the cumulative probability maps for watershed divides derived from increasing number of Strahler order (figure 3.39). While decreasing the number of watershed the differences among derived divide nets become more evident. Generally the nets derived from the average dataset or the inverse of the cumulative probability map for stream network have the higher values. With increasing Strahler order values the overall probability of the divides derived from the cumulative probability map for watershed decrease. It was not possible to extract river segments of order higher then four from this kind of dataset. The overall probability is increasing when increasing the Strahler order considered. With less number of watersheds, it become easier to identify the net passing through the most probable cells.

In figure 3.40 the distribution probabilities along the watershed nets are presented when all the Strahler orders were considered. The extracted nets present a similar trend, overlapping in most of

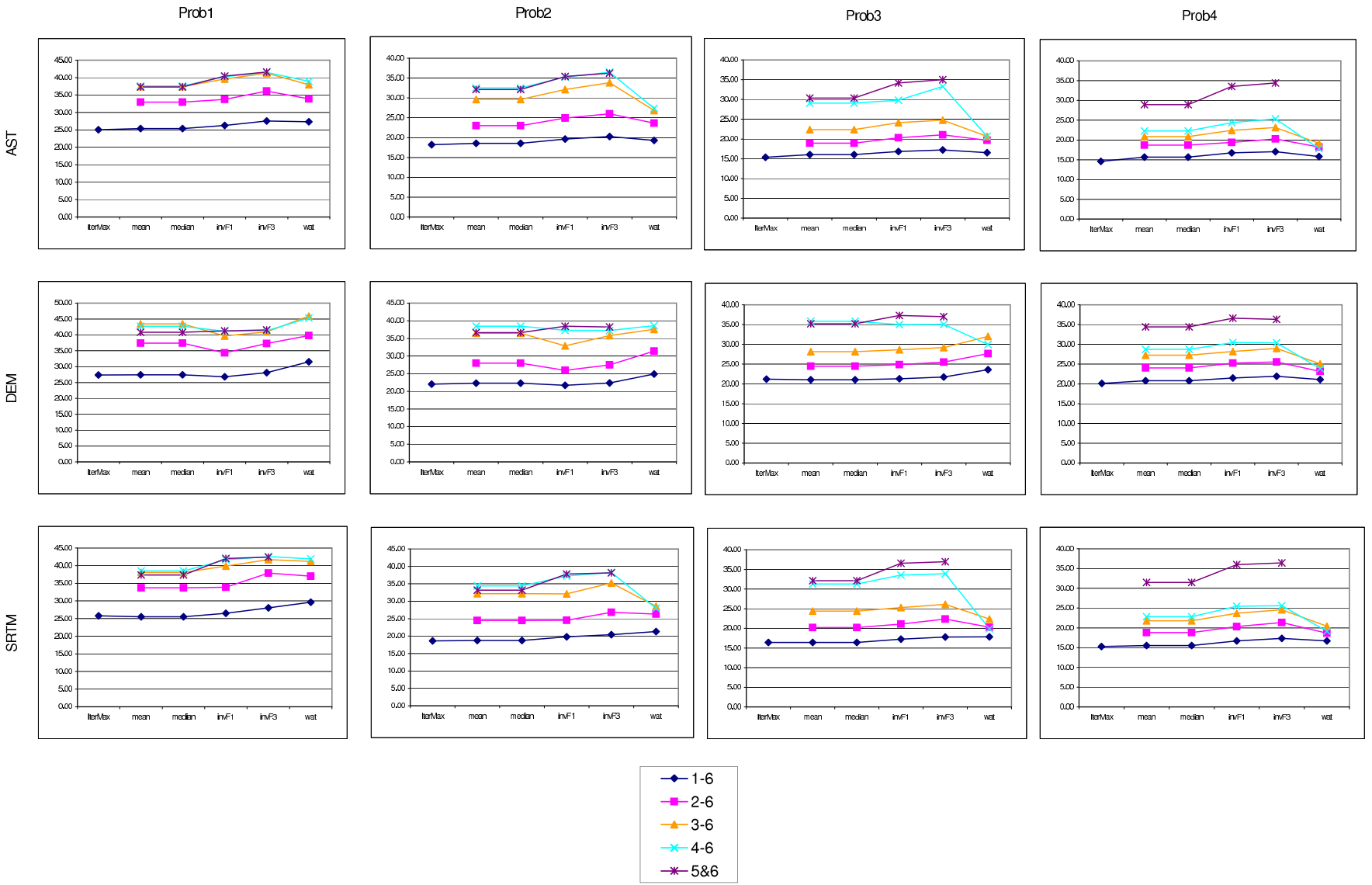

Figure 3.39: Overall probability of watershed divides for considered datasets and different Strahler orders considered.

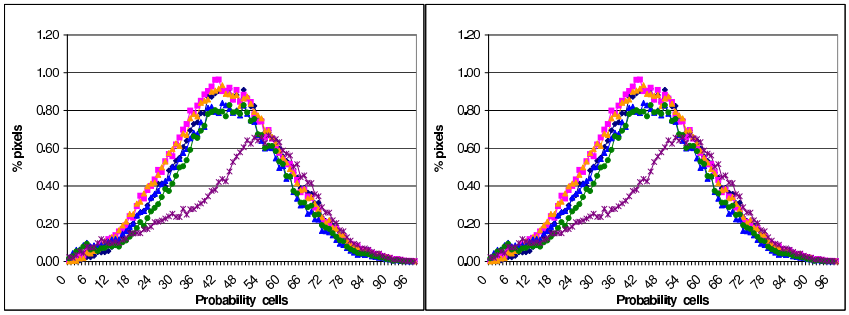

(a) AST (b) DEM

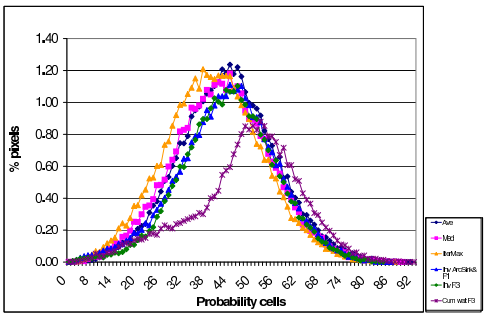

(c) SRTM

Figure 3.40: Distribution probabilities along the networks (all Strahler orders considered).

the points. The curve for the watershed net extracted from the cumulative probability map is rather different, shifted towards the right. The behaviour of the three DTMs is similar. DEM has curves with larger and flatter shape. SRTM and AST have narrower curves, with higher peaks. Especially AST that is presenting the higher peaks among the considered DTMs. Figure 3.42 for AST, figure 3.42 for DEM and figure 3.43 for SRTM present the distribution probabilities along the watershed divides nets when not all the Strahler orders were considered. In particular:

a) all Strahler orders with overall probability calculated using the cumulative probability map `prob1`, obtained using divides of Strahler order 2 to 6;
b) Strahler orders 2 to 6 with overall probability calculated using the cumulative probability map `prob1`, obtained using divides of Strahler order 2 to 6;
c) Strahler orders 3 to 6 with overall probability calculated using the cumulative probability map `prob2`, obtained using divides of Strahler order 3 to 6;
d) Strahler orders 4 to 6 with overall probability calculated using the cumulative probability map `prob3`, obtained using divides of Strahler order 4 to 6;
e) Strahler orders 5 and 6 with overall probability calculated using the cumulative probability map `prob4`, obtained using divides of Strahler order 5 and 6.

The curves show different trends according to the cumulative probability used and to the DTM considered. The first case (a) shows a peak in the left side of the graph with smoother curve on the left. The second case (b) presents a centred peak, more similar to what obtained when considering all the Strahler orders. In case of `prob2` the behaviour of the net derived from the cumulative probability for watershed is different with a high number of pixels of value 0. The other nets present a similar trend. `prob3` emphasises the pattern of the net derived from the cumulative probability map for watershed, with the other curves almost always overlapping. The main differences among DTMs can be seen in case of `prob1` is used, with DEM showing a considerable different shape. Generally DEM presents curves that are flatter, while the peaks of AST curves are the highest among the considered DTMs.

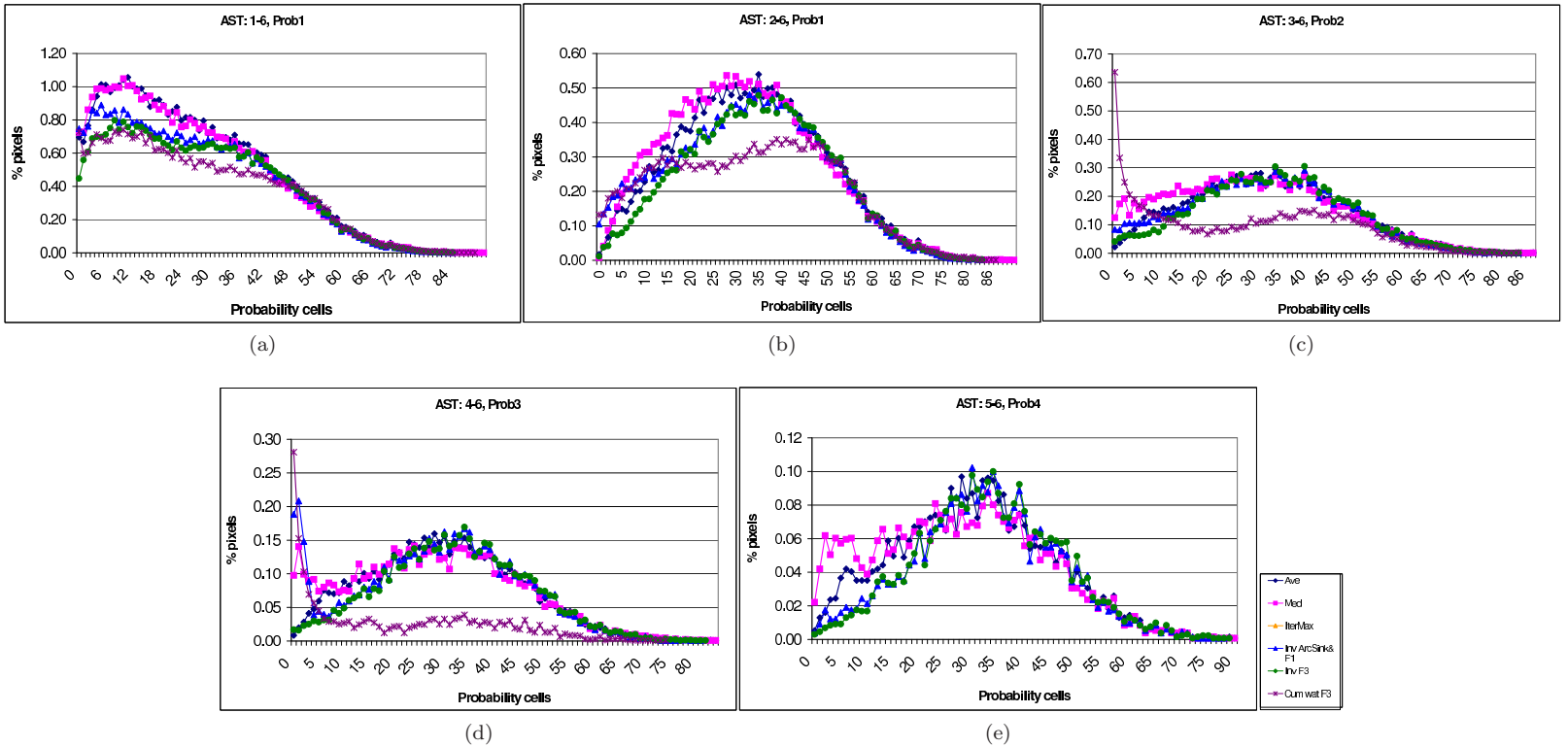

Figure 3.41: AST:Distribution probabilities along the networks.

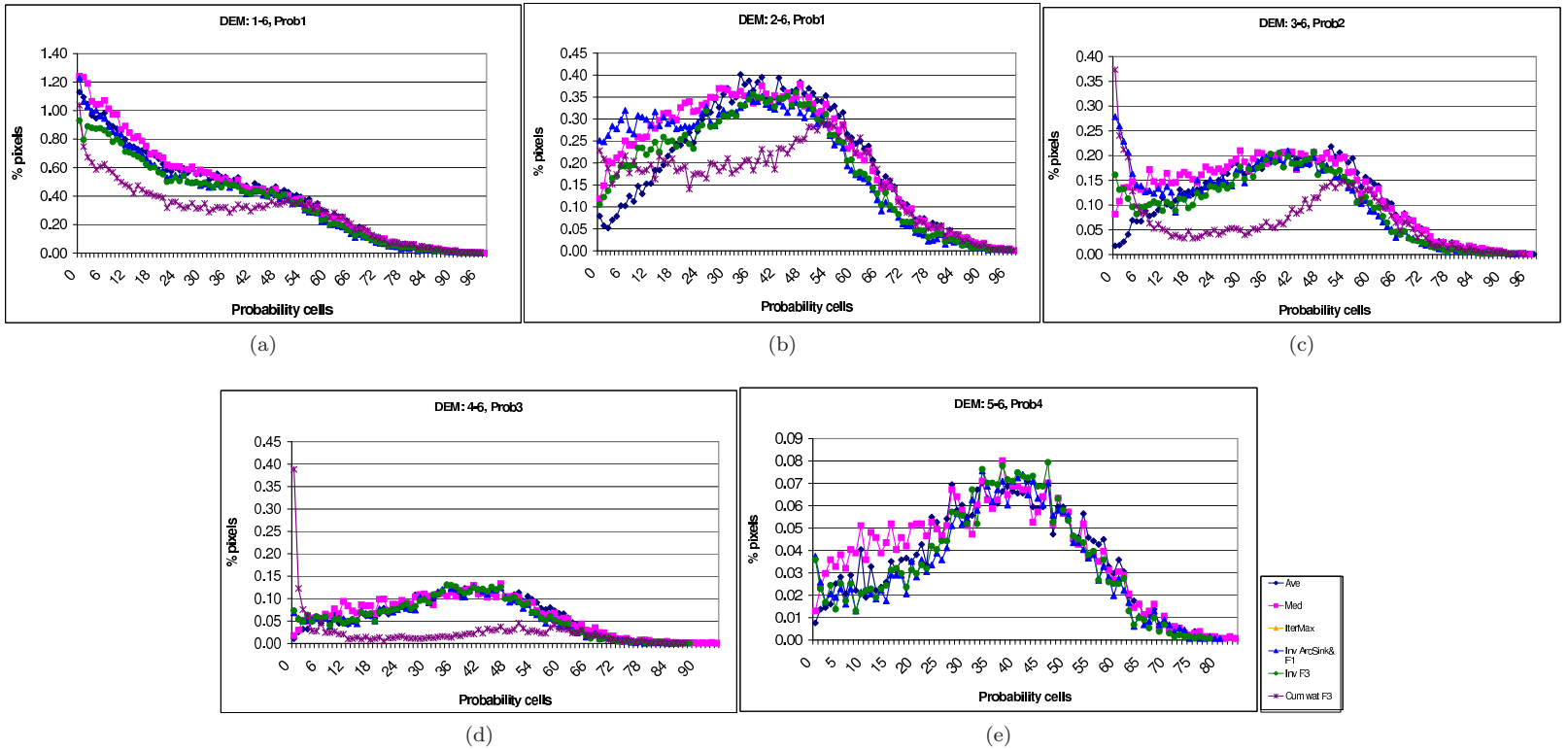

Figure 3.42: DEM:Distribution probabilities along the networks.

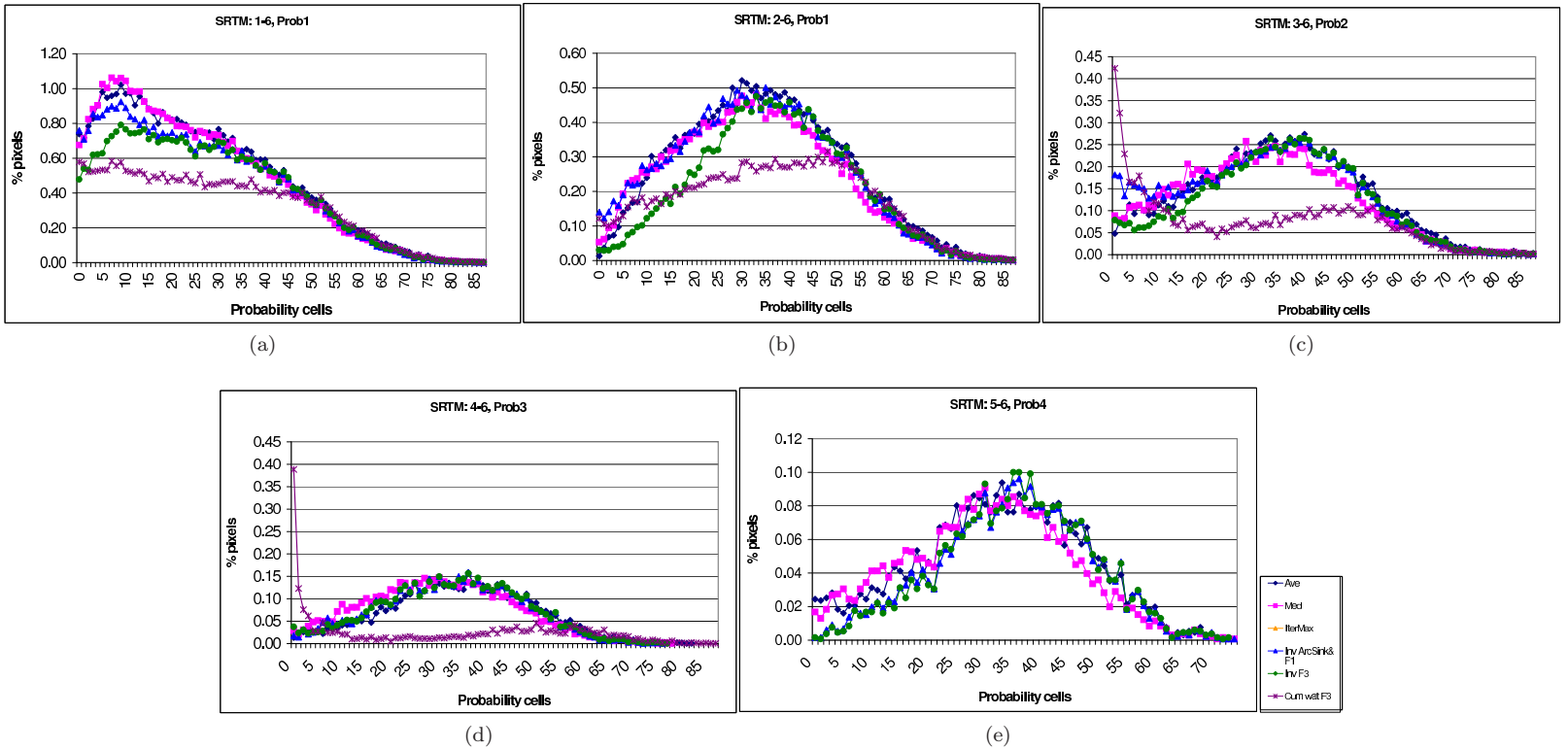

Figure 3.43: SRTM:Distribution probabilities along the networks.

Spatial distribution

The spatial distribution for the most probable watershed divide nets when all Strahler orders are considered are presented in figure 3.44. The nets derived from the average dataset present a higher number of watersheds with reduced size. The net derived from the inverse of the cumulative probability map for stream network, filled with optimal hybrid carving, shows lower number of watersheds. The borders are falling in the areas with higher probability in both cases. The net derived from the cumulative probability map for watershed divides has larger watersheds and in some case, especially for SRTM present straight lines cutting the watersheds.

Figure 3.46 for AST, figure 3.46 for DEM and figure 3.47 for SRTM present the derived watershed divides nets when not all the Strahler orders are considered. In case of `prob1` (case a) the behaviour of most probable extracted nets is similar to what was previously described, but with less numerous watersheds. In case of `prob2` (case b) the nets derived from the inverse of the cumulative probability map for stream network is following more precisely the areas with higher probability. The net derived from the cumulative probability map for watershed is not very consistent with the higher probability pixels areas. The case of `prob3` (case c) is quite similar with average derived net and inverse cumulative probability map for stream network derived nets following the areas with higher probability, while the net derived from cumulative probability map for watershed is quite different. `Prob4` (case d) is similar for what concern the average and the inverse cumulative probability map for stream network derived nets. In this case the most probable net could not be derived from the cumulative probability map for watershed, as the maximum Strahler order obtained was four.

AST shows better delineated nets in all three cases presented. It is possible to identify watershed and most of the borders fall in the higher probability areas. The DEM dataset produced more smooth results with some straight lines, not following the main morphology of the area. The SRTM show the most fuzzy distribution with a lot of straight lines especially in the case of the net derived from the inverse of the cumulative probability map for stream network.

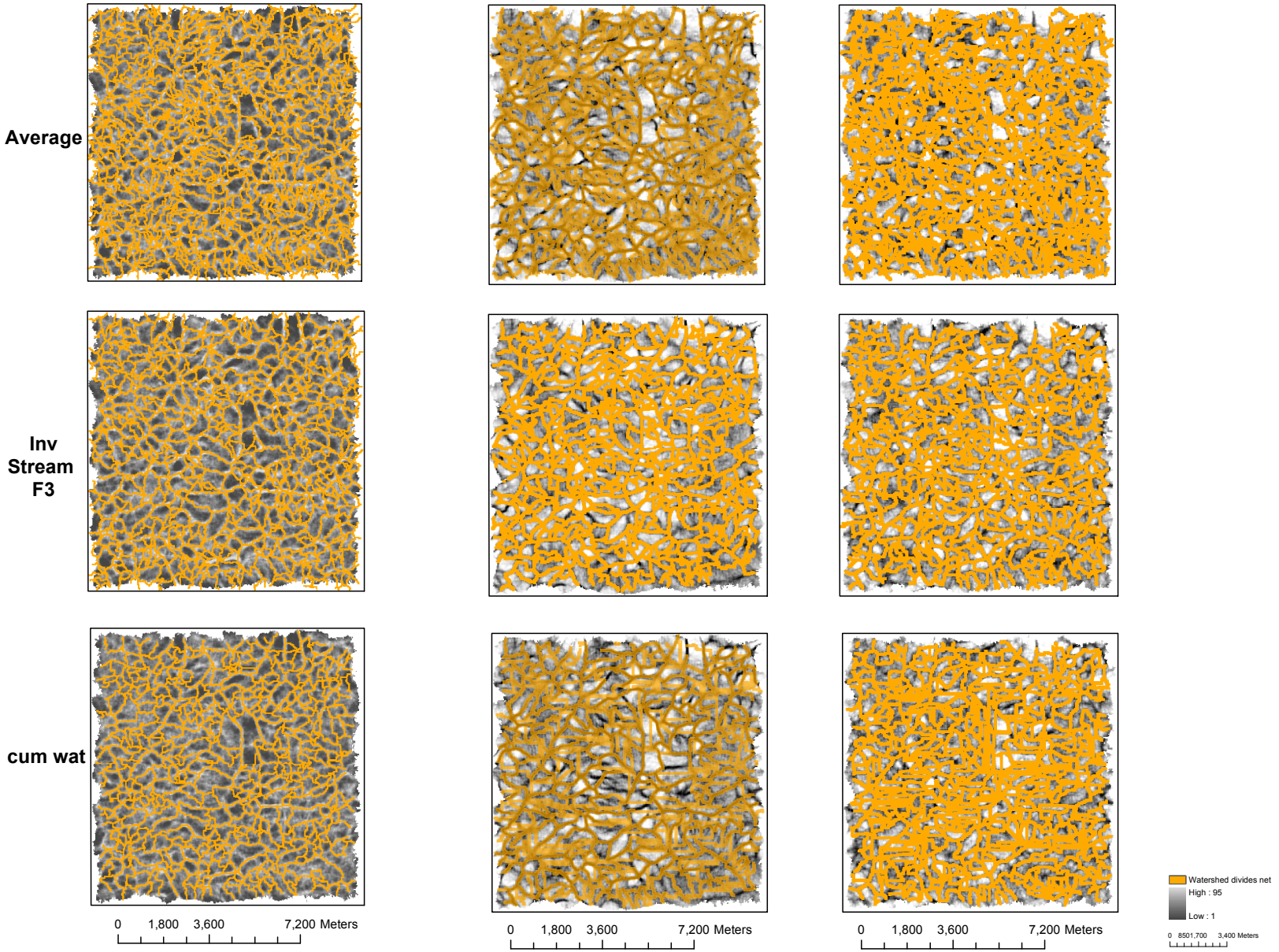

(a) AST (b) DEM (c) SRTM

Figure 3.44: Most probable watershed divide nets considering all Strahler orders (prob0).

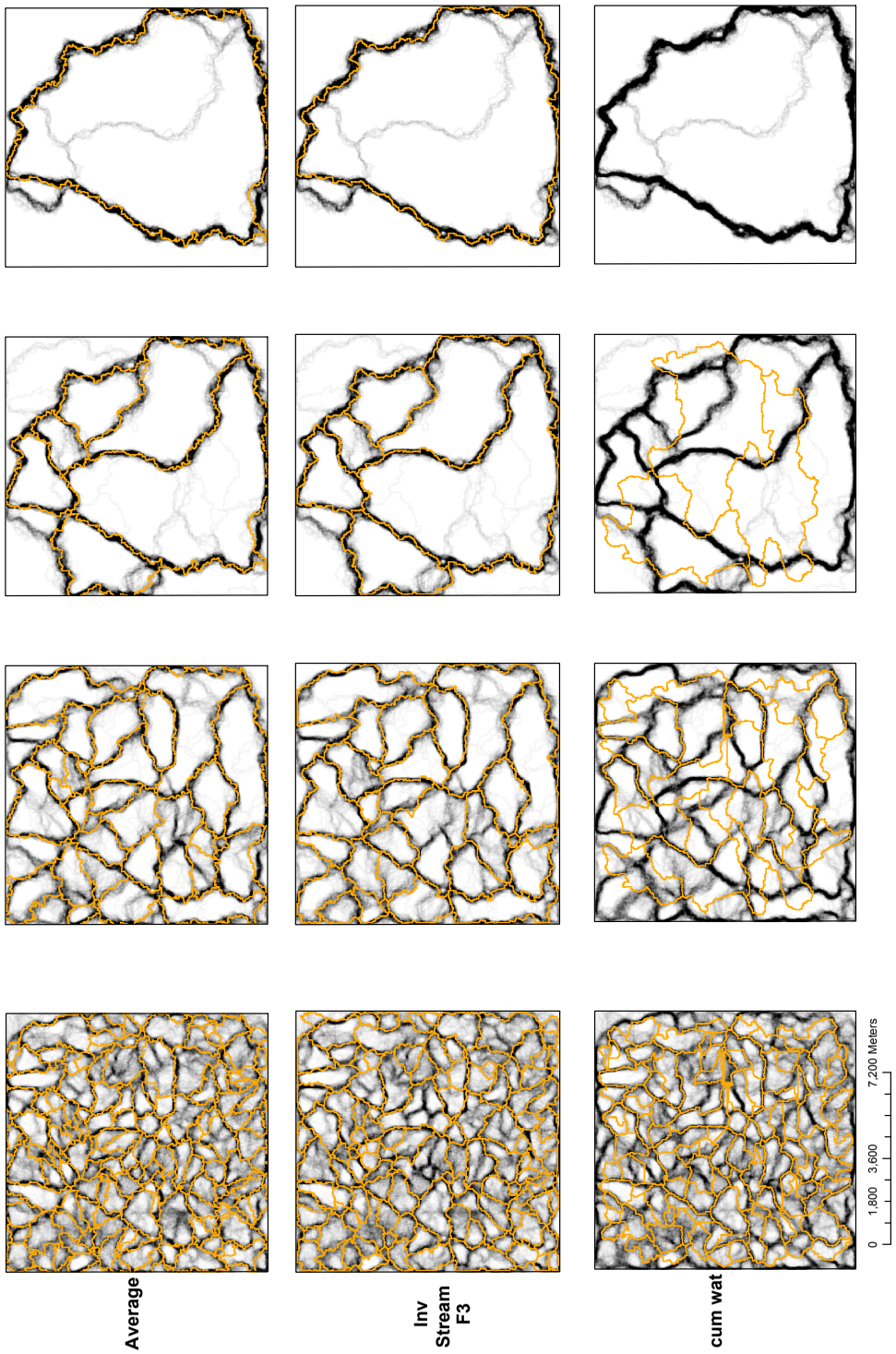

(a) Prob1 (b) Prob2 (c) Prob3 (d) Prob4

Figure 3.45: AST: Most probable watershed divide nets for different Strahler orders considered.

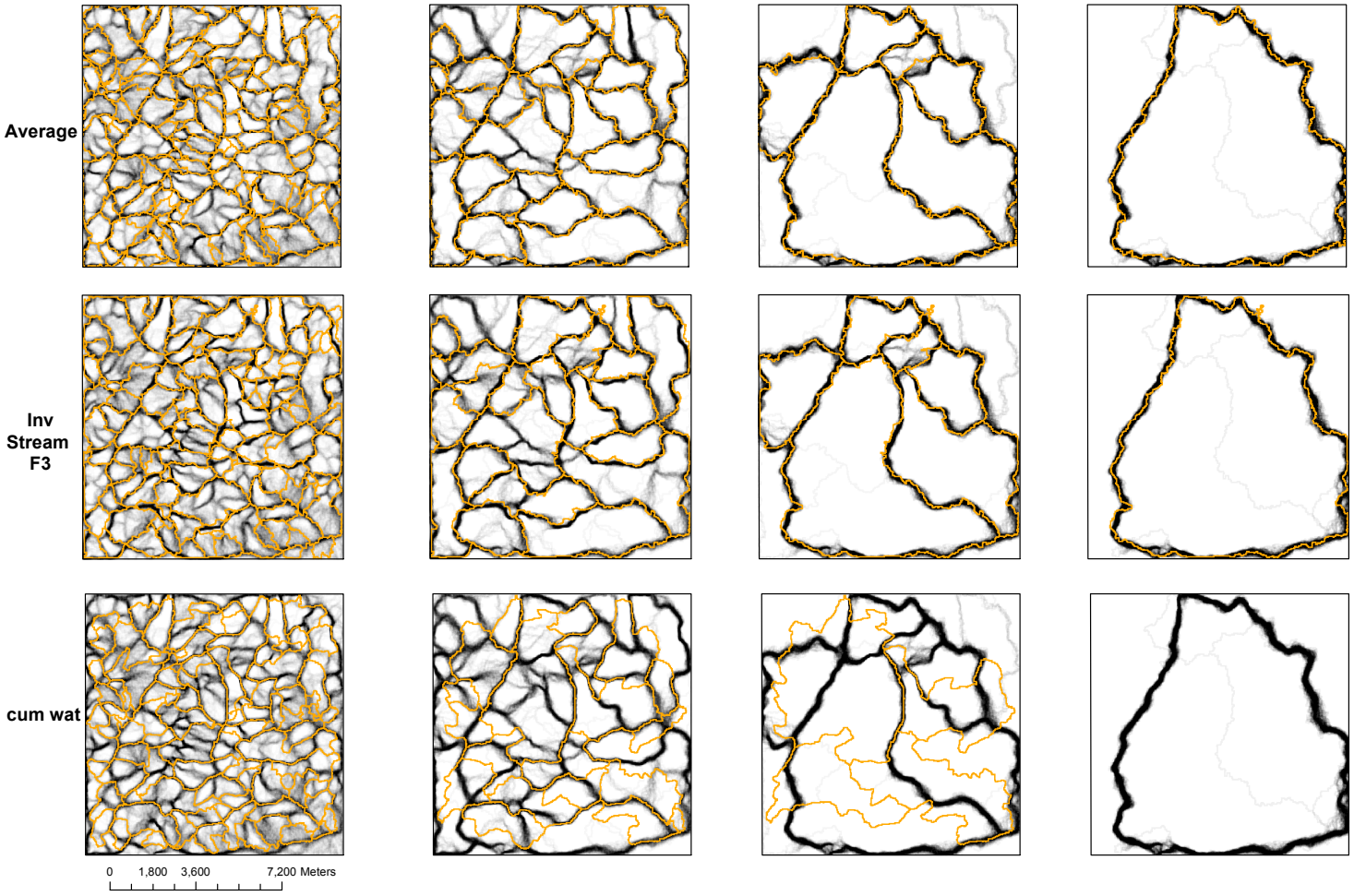

(a) Prob1 (b) Prob2 (c) Prob3 (d) Prob4

Figure 3.46: DEM: Most probable watershed divide nets for different Strahler orders considered.

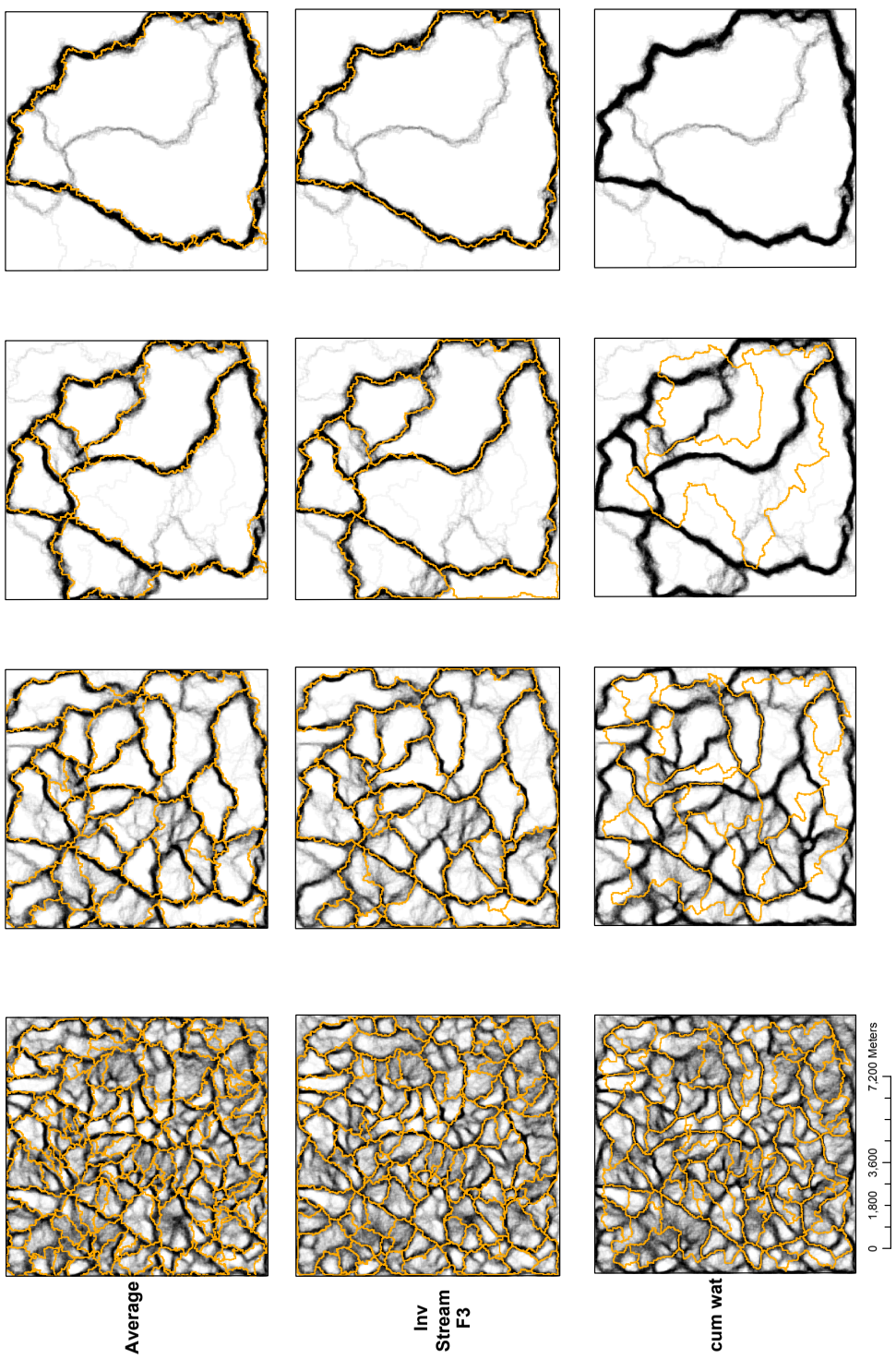

(a) Prob1 (b) Prob2 (c) Prob3 (d) Prob4

Figure 3.47: SRTM: Most probable watershed divide nets for different Strahler orders considered.

4

Concluding remarks

The spatial positioning and the geomorphological properties of hydrographic features are important in many environmental and management studies. Digital elevation data are commonly used to model drainage divides, hydrographic channel networks and stream attributes such as contribute drainage area, channel sinuosity or tributary junctions (Davies et al., 2007).

Many algorithms have been developed to extract hydrological and morphological features from DEMs but less studies have dealt with the determination of the uncertainty in these parameters, or the effect of this uncertainty in further applications. The accuracy of these parameters is dependent both on the algorithm and on the errors associated with the DEM itself. Since it is almost impossible to model all the errors associated with a given algorithm and since a DEM is normally only provided with a RMSE measure, simple error propagation is not adequate to determine the error associated with the derived hydrological parameters. A more rigorous method of determining the affect of DEM errors on derived topographic parameters is with statistical analysis using Monte Carlo simulation and error realisations of the DEMs (Raaflaub and Collins, 2006). However there are some drawback such as computational time and complexity (Reuter et al., 2008a).

DTMs of different original resolution were compared in order to assess the quality of derived hydrological and morphological features. A stochastic approach was used to model the error propagation. The probabilistic distribution of extracted hydrological features was drawn considering the spatial structure of errors in the datasets. The features considered were: (i) stream network, and (ii) watershed divides net. The distribution of the Strahler order of the features was studied. An analysis of the overall probability of features extracted from variously prepared datasets was carried in order to get information on where is the most probable stream network or watershed divides net.

The main points are summarised below:

Preprocessing of DTMs

- The impact of tested sink filling methods do not influence significantly the roughness of the dataset (figure 2.3).
- The main differences in heights among the considered DTMs appear in urban and forested land uses with SRTM > DEM > AST (figure 2.5). The use of filling methods does not impacts in a significant ways on the differences among datasets (figure 2.7)
- The DEM dataset reaches an higher Strahler order followed by AST and SRTM (figure 2.9). The CDA for AST in low Strahler order segments is much higher for AST than for the other two datasets (figure 2.10).
- AST present more evident micromorphology with higher local variability (figure 2.13).

Error modelling

- DEM datasets has a different variogram model with a more linear trend (figure 3.2).
- 100 iterations explain in all cases more than 90% of the variability. The number of iterations needed to reach 95% of the variability is different according to the datset considering. DEM requires about 50% of the iterations needed for AST and SRTM (figure 3.3).

– The flow accumulation threshold calculated is rather similar for all the DTMs considered (figure 3.6).

Probability distribution

– The probability values obtained for stream network are generally low (maximum is 72%) and indicate an high uncertainty in the automatic delineation of hydrological features (Morris and Heerdegen, 1988). The values obtained for watershed are higher, reaching 90% and over, but the distribution is much more smoothed and scattered.

– In the probability distribution for stream network DEM reaches higher probability values (figure 3.8) and has a less scattered and smoothed distribution (figure 3.11 to figure 3.13 on pages 32–34). AST and SRTM have similar trends with slightly more defined results for AST dataset (table 3.4).

– The results for the probability distribution for watershed divides net are very smooth and spread in the space (figure 3.11, figure 3.12, figure 3.13). It is difficult to recognised the watershed and only the main divides are easily identifiable. The probability values follow the normal distribution (figure 3.10).

– The probability distribution maps for ridge cells and basin are more clearly defined in case of DEM (figure 3.11 to figure 3.14 on pages 32–35).

Strahler order

– Most of the pixels have value two of Strahler order variety, i.e. the cell has the same Strahler order when it is part of a river network (figure 3.15a).

– The Strahler order distribution for stream network has similar trends for the different considered DTMs in various orders. The highest probability value is reached in order three for AST, order two for DEM and order four for SRTM (figure 3.17).

– The uncertainty for stream segments of Strahler order one or two is very high. A better delineation can be found in segments with higher orders, from three up (figure 3.21 to figure 3.23 on pages 43–45).

– Considering segment of increasing Strahler order to generate watersheds the probability distribution for watershed divide nets is less smoothed and it is easier to identify the watershed regions (figure 3.26 to figure 3.28 on pages 48–50).

Most probable feature

– The stream networks derived from the inverse probability map have higher overall probability values than network extracted from DTMs-derived data, i.e. mean, median of iteration and network that maximised the overall probability among the iterations (max-prob; figure 3.29).

– The lowest values of overall probability are obtained with the max-prob network. The highest results of overall probability are obtained for the stream network derived from the inverse probability map and filled with the optimal hybrid method.

– AST dataset has the lowest numerical values, but slightly better spatial matching. The DEM dataset has the highest numerical results (figure 3.33 to figure 3.35 on pages 55–57).

– The analysis of overall probability for the most probable watershed divide net did not provide clear results when stream segments of all the Strahler orders were considered (figure 3.38). The highest numerical values were reached considering the probability map for watershed divides net, but the spatial matching was inconsistent (figure 3.44).

– The results of the overall probability have a more clear trend when considering segment of increasing Strahler order to generate watersheds. The net extracted from the inverse probability map for stream networks filled with optimal hybrid method has the higher values (figure 3.39). The spatial overlapping of of features extracted for the probability map for watershed divides nets is still poor (figure 3.45 to figure 3.47 on pages 69–71).

– The results show a rather good spatial matching with representation of terrain surfaces, especially in case of streams of higher Strahler order (figure 3.37 on page 60). A comparison with more accurate hydrographic data derived from traditional cartography or satellite/aerial imagery in different morphological and hydrological conditions would give a further indication on the spatial matching of features extracted with the proposed method .

The AST dataset has the highest original resolution and it was expected to provide the more defined results with lower variability (Nikolakopoulos et al., 2006; Sorensen and Seibert, 2007). The results obtained have less uncertainty than what was obtained from SRTM, but higher than the DEM results. AST datasets presents visually an higher local variability and it was not corrected for flat regions as in case of SRTM case. Furthermore these local variability could be emphasised by the error model and the added noise. However the spatial matching of extracted most probable features is the rather accurate. The DEM dataset presents a lower variability in the various extracted features as it is a mosaic, resampled to a common resolution, of DTMs from different sources of, generally, higher resolution and low uncertainty. The SRTM dataset has the lowest original resolution and presents the highest variability in the results.

The derivation of most probable network gives an indication on the location where there are the highest probabilities to find the features on the terrain. The methodology presented is useful to derive hydrographic features that minimise the uncertainty due to errors in the elevation data source. The use of more iterations of DTMs with modelled error seems to give more reliable results (Raaflaub and Collins, 2006) or at least a measure of the reliability of the obtained results.

Bibliography

Annoni, A., Luzet, C., Gubler, E., Ihde, J. (Eds.), 2003. Map Projections for Europe. Vol. EUR 20120 EN. European Commission, DG Joint Research Centre.
URL http://www.ec-gis.org/sdi/publist/pdfs/annoni-etal2003eur.pdf

Blaszczynski, J. S., 1997. Landform characterization with Geographic Information Systems. Photogrammetric Enginnering and Remote Sensing 63 (2), 183–191.

Burrough, P. A., McDonell, R., 2000. Principles of Geographical Information System. Oxford University Press.

Cambardella, C. A., Moorman, T. B., Novak, J. M., Parkin, T. B., Karlen, D. L., Turco, R. F., Konopka, A. E., 1994. Field-scale variability of soil properties in Central Iowa soils. Soil Scientific Society American Journal 58, 1501–1511.

Chou, T., Lin, W., Lin, C., Chou, W., Huang, P., 2004. Application of the PROMETHEE technique to determine depression outlet location and flow direction in DEM. Journal of Hydrology 287, 4961.

Colombo, R., Vogt, J. V., Soille, P., Paracchini, M. L., de Jager, A., 2007. Deriving river networks and catchments at the European scale from medium resolution digital elevation data. Catena 70, 296–305.

Cressie, N., 1993. Statistics for Spatial Data. Wiley, New York.

Darnell, A., Tate, N., Brunsdon, C., 2008. Improving user assessment of error implications in digital elevation models. Computers, Environment and Urban Systems 32, 268–277.

Davies, J., Lagueux, K., Sanderson, B., Beechie, T., 2007. Modeling stream channel characteristics from drainage-enforced DEMs in Puget Sound, Washington, USA. Journal of the American Water Resources Association 43 (2), 414 – 426.

EuroDEM, 2008. Sample from EuroDEM (c) eurogeographics and bundesamt fuer kartographie und geodaesie. Tech. rep., EuroGeographics.
URL http://www.eurogeographics.org/eng/EuroDEM.asp

EuroGeographics, April 2008. Eurodem user guide. Tech. rep., EuroGeographics.
URL http://www.eurogeographics.org/eng/documents/EuroDEM_UserGuide_v1_0_Final.pdf

Fairfield, J., Leymarie, P., 1991. Drainage networks from grid digital elevations models. Water Resources Research 27 (5), 709–717.

Fisher, P., 1993. Algorithm and implementation uncertainty in viewshed analysis. International Journal of Geographical Information Systems 7 (4), 331–347.

Garbrecht, J., Martz, L., 2000. Digital elevation model issues in water resources modeling. In: Maidment, D., Djokic, D. (Eds.), Hydrologic and Hydraulic Modeling Support with Geographic Information Systems: Redlands. Environmental Systems Research Institute Press.

Goodchild, M., Mark, D., 1987. The fractal nature of geographic phenomena. Annals, Association of American Geographers 77, 265278.

Goovaerts, P., 1997. Geostatistics for Natural Resources Evaluation. Oxford University Press.

Hancock, G. R., 2005. The use of digital elevation models in the identification and characterization of catchments over different grid scales. Hydrological Processes 19, 17271749.

Hengl, T., Reuter, H. (Eds.), Oct 2008. Geomorphometry: Concepts, Software, Applications. Vol. 33 of Developments in Soil Science. Elsevier, Amsterdam.
URL http://www.elsevierdirect.com/product.jsp?isbn=9780123%743459&ref=CWS1#6

Holmes, K., Chadwick, O., Kyriakidis, P., 2000. Error in a USGS 30-meter digital elevation model and its impact on terrain modeling. Journal of Hydrology 233, 154–173.

Hovenbitzer, M., 2008. The European DEM (EuroDEM). In: The International Archives of the Photogrammetry, Remote Sensing and Spatial Information Sciences. Vol. XXXVII. pp. 1853–1856, iSPRS Congress Beijing 2008.
URL http://www.isprs.org/congresses/beijing2008/proceedings/4_pdf/323.pdf

Hunter, G., Goodchild, M., 1997. Modeling the uncertainty of slope and aspect estimates derived from spatial databases. Geographical Analysis 29, 35–49.

Hutchinson, M., 1989. A new procedure for gridding elevation and stream line data with automatic removal of spurious pits. Journal of Hydrology 106 (211-232), 211–232.

Jarvis, A., Reuter, H., Nelson, A., Guevara, E., 2006. Hole-filled seamless SRTM data V3. Tech. rep., International Centre for Tropical Agriculture (CIAT).

Jenson, S. K., Domingue, J. O., 1988. Extracting topographic structure from digital elevation data for Geographic Information System analysis. Photogrammetric Engineering and Remote Sensing 54 (11), 1593–1600.

Journel, A., 1996. Modelling uncertainty and spatial dependence: Stochastic imaging. International Journal of Geographical Information Systems 10 (5), 517–522.

Keys, R., 1981. Cubic convolution interpolation for digital image processing. IEEE Transactions in Acoustics, Speech and Signal Processing 29 (6), 1153 – 1160.

Kyriakidis, P., Ashton M. Shortridge, A., Goodchild, M., 1999. Geostatistics for conflation and accuracy assessment of digital elevation models. International Journal of Geographical Information Science 13 (7), 677–707.

Lindsay, 2006. Sensitivity of channel mapping techniques to uncertainty in digital elevation data. International Journal of Geographical Information Science 20(6), 669–692.

Maune, D. (Ed.), 2001. Digital Elevation Model Technologies and Applications: The DEM Users Manual. American Society for Photogrammetry and Remote Sensing.

Metropolis, N., Ulam, S., 1949. The Monte Carlo method. Journal of the American Statistical Association 44 (247), 335–341.

Miller, C., Laflamme, R., 1958. The digital terrain modelling - theory and application. Photogrammetric Engineering 25, 433–442.

Moore, I. D., Grayson, R. B., Landson, A. R., 1991. Digital terrain modelling: a review of hydrological, geomorphological, and biological applications. Hydrological Processes 5, 3–30.

Morris, D., Heerdegen, R., 1988. Automatically derived catchment boundaries and channel networks and their hydrological applications. Geomorphology 1, 131–141.

Nikolakopoulos, K. G., Kamaratakis, E. K., Chrysoulakis, N., 2006. SRTM vs ASTER elevation products. Comparison for two regions in Crete, Greece. International Journal of Remote Sensing 27 (21), 4819–4838.

Nunes de Lima, M., 2005. IMAGE2000 and CLC2000: Products and methods. Tech. Rep. EUR 21757, European Commission, Joint Reaserch Centre.

Oksanen, J., Sarjakoski, T., 2005. Error propagation of DEM-based surface derivatives. Computers and Geosciences 31 (8), 1015–1027.

Oksanen, J., Sarjakoski, T., 2006. Uncovering the statistical and spatial characteristics of fine toposcale DEM error. International Journal of Geographical Information Science 20 (4), 345–369.

Peucker, T., Douglas, D., 1975. Detection of surface-specific points by local parallel processing of discrete terrain elevation data. Computer Graphics and Image Processing 4, 375–387.

Pike, R., 2002. A bibliography of terrain modeling (geomorphometry), the quantitative representation of topography - supplement 4.0. Tech. Rep. OPEN-FILE REPORT 02-465, U.S. Department of the Interior - U.S. Geological Survey.

Planchon, O., Darboux, F., 2001. A fast, simple and versatile algorithm to fill the depressions of digital elevation models. Catena 46, 159–176.

Polidori, L., Chorowicz, J., Guillande, R., 1991. Description of terrain as a fractal surface, and application to digital elevation model quality assessment. Photogrammetric Engineering and Remote Sensing 57 (10), 1329–1332.

Raaflaub, L., Collins, M., 2006. The effect of error in gridded digital elevation models on the estimation of topographic parameters. Environmental Modelling & Software 21, 710–732.

Reuter, H., Hengl, T., Gessler, P., Soille, P., 2008a. Preparation of DEMs for geomorphometric analysis. In: Hengl, T., Reuter, H. (Eds.), Geomorphometry: Concepts, Software, and Applications. Vol. 33 of Developments in Soil Science. Elsevier, Ch. 4, pp. 87–120.

Reuter, H., Strobl, P., Mehl, W., Jarvis, A., Nelson, A., Seliger, R., 2008b. 1 arc second DEM based on ASTER data v1.0. European Commission - DG Joint Research Centre (JRC) and and International Centre for Tropical Agriculture (CIAT), URL of mirror site: http://srtm.csi.cgiar.org/.

Reuter, H., Strobl, P., Mehl, W., Jarvis, A., Nelson, A., Seliger, R., 2008c. Methods for data fusion for a global 30m digital surface model. In preparation.

Reuter, H. I., Nelson, A., Jarvis, A., 2007. An evaluation of void-filling interpolation methods for SRTM data. International Journal of Geographical Information Science 21 (9), 983–1008.

Reuter, H. I., Wendroth, O., Kersebaum, K., 2006. Optimisation of relief classification for different levels of generalisation. Geomorphology 77, 79–89.

Riley, S. J., DeGloria, S. D., Elliot, R., 1999. A terrain ruggedness index that quantifies topographic heterogeneity. Intermountain Journal of Sciences 5 (1-4), nd.

Soille, P., 2004a. Morphological carving. Pattern Recognition Letters 25, 543–550.

Soille, P., 2004b. Optimal removal of spurious pits in grid digital elevation models. Water Resources Research 40 (12), W12509.

Soille, P., 2007. From mathematical morphology to morphological terrain features. In: Peckham, R., Jordan, G. (Eds.), Digital Terrain Modelling. Springer, Berlin.

Soille, P., Ansoult, M., Jun. 1990. Automated basin delineation from digital elevation models using mathematical morphology. Signal Processing 20, 171–182.

Soille, P., Gratin, C., Jun. 1994. An efficient algorithm for drainage networks extraction on DEMs. Journal of Visual Communication and Image Representation 5 (2), 181–189.

Soille, P., Vogt, J., Colombo, R., 2003. Carving and adaptative drainage enforcement of grid digital elevation models. Water Resources Research 39(12), 1366.

Sorensen, R., Seibert, J., 2007. Effects of DEM resolution on the calculation of topographical indices: TWI and its components. Journal of Hydrology 347, 79–89.

Sorensen, R., Zinko, U., Seibert, J., 2006. On the calculation of the topographic wetness index: evaluation of different methods based on field observations. Hydrology and Earth System Sciences 10 (1), 101–112.

Strahler, A. N., 1952. Hypsometric (area-altitude) analysis of erosional topography. Bulletin Geological Society of America 63, 1117–1142.

Tarboton, D. G., 1997. A new method for the determination of flow directions and upslope areas in grid digital elevation models. Water Resources Research 33, 309–319.

Tarboton, D. G., Bras, R. L., Rodriguez-Iturbe, I., 1991. On the extraction of channel networks from digital elevation data. Hydrological Processes 5, 81–100.

Temme, A., Heuvelink, G., Schoorl, J., Claessens, L., 2008. Geostatistical simulation and error propagation in geomorphometry. In: Hengl, T., Reuter, H. (Eds.), Geomorphometry: Concepts, Software, and Applications. Vol. 33 of Developments in Soil Science. Elsevier, Ch. 5, pp. 121–140.

Vogt, J., Soille, P., de Jager, A., Rimavičiute, E., Mehl, S., Foisneau, S., Bódis, K., Dusart, J., Paracchini, M., Haastrup, P., Bamps., C., 2007. A pan-European River and Catchment Database. No. EUR 22920 EN. European Publications Office.

Vogt, J. V., Colombo, R., Bertolo, F., 2003. Deriving drainage networks and catchment boundaries: a new methodology combining digital elevation data and environmental characteristics. Geomorphology 53, 281–298.

Vrščaj, B., Daroussin, J., Montanarella, L., 2007. SRTM as a possible source of elevation information for soil-landscape modelling. In: Peckham, R., Jordan, G. (Eds.), Digital Terrain Modelling. Springer, Berlin.

Wang, L., Liu, H., 2006. An efficient method for identifying and filling surface depressions in digital elevation models for hydrologic analysis and modelling. International Journal of Geographical Information Science 20 (2), 193–213.

Webster, R., Oliver, M. A., 2000. Geostatistics for Environmental Scientists. John Wiley & Sons.

Wechsler, S. P., 2007. Uncertainties associated with digital elevation models for hydrologic applications: A review. Hydrology and Earth System Sciences 11 (4), 1481–1500.

Wechsler, S. P., Kroll, C. N., 2006. Quantifying DEM uncertainty and its effect on topographic parameters. Photogrammetric Engineering & Remote Sensing 72 (9), 1081–1090.

Wilson, J., Gallant, J., 2000. Terrain Analysis - Principles and Applications. Wiley, New York.

Wise, S., 1998. The effect of GIS interpolation errors on the use of digital elevation models in geomorphology. In: Lane, S., Richards, K., Chandler, J. H. (Eds.), Landform Monitoring, Modelling and Analysis. John Wiley and Sons, pp. 139–164.

European Commission

EUR 23489 EN – Joint Research Centre – Institute for Environment and Sustainability
Title: Quality assessment of hydro-geomorphological features derived from Digital Terrain Models
Author(s): Laura Poggio and Pierre Soille
Luxembourg: Office for Official Publications of the European Communities
2008 – 89 pp. – 21.0 x 29.7 cm
EUR – Scientific and Technical Research series – ISSN 1018-5593

Abstract
Digital terrain models (DTM) provide a model for representing the continuous earth elevation surface that can contain errors introduced by the main phases of generation and modelling. Uncertainty of the model is rarely considered by users. Assessment of uncertainty require information on the nature, amount and spatial structure of the errors. DTMs of different original resolution were compared in order to assess the quality of derived hydrological and morphological features. SRTM dataset with resolution of 100m, DEM dataset mosaic from various sources with a resolution of 60m and ASTER derived dataset with a resolution of 30m were used. The error propagation was modelled with a stochastic approach. The probabilistic distribution of extracted hydrological features was drawn considering the spatial structure of errors in the datasets. The features considered were stream network and watershed divides net. The distribution of the Strahler order of the features was studied. An analysis of the overall probability of features extracted from variously prepared datasets was carried in order to get information on where is the most probable stream network or watershed divides net.

The mission of the JRC is to provide customer-driven scientific and technical support for the conception, development, implementation and monitoring of EU policies. As a service of the European Commission, the JRC functions as a reference centre of science and technology for the Union. Close to the policy-making process, it serves the common interest of the Member States, while being independent of special interests, whether private or national.

JRC
EUROPEAN COMMISSION

Publications Office
Publications.eu.int